

UNIVERSITY OF OKLAHOMA

GRADUATE COLLEGE

STUDY OF STRESS FIELD IN SEISMOGENIC PROCESSES IN OKLAHOMA

A THESIS

SUBMITTED TO THE GRADUATE FACULTY

in partial fulfillment of the requirements for the

Degree of

MASTER OF SCIENCE

By

YAN QIN

Norman, Oklahoma

2017

STUDY OF STRESS FIELD IN SEISMOGENIC PROCESSES IN OKLAHOMA

A THESIS APPROVED FOR THE
CONOCOPHILLIPS SCHOOL OF GEOLOGY AND GEOPHYSICS

BY

Dr. Xiaowei Chen, Chair

Dr. Nori Nakata

Dr. Ze'ev Reches

This thesis is dedicated to my parents.

Acknowledgements

There have been many people who walked alongside me during the past two years.

They have guided me, helped me and showed me the whole new world of geophysics. I would like to thank each and every one of them. First and foremost, I would like to express my deepest gratitude to my supervisor Dr. Xiaowei Chen for her continuous support, motivation and immense knowledge over the past two years. Thanks for being patient with me and inspiring me to pursue a PhD degree in Geophysics.

I would like to thank my committee members Dr. Nori Nakata and Dr. Ze'ev Reches for their time, insight and advice.

I would thank my department and Oklahoma Geological Survey for providing funding, data and many other resources.

I would thank my colleagues in our group for sharing information and providing timely comments.

Last but not least, I would thank my parents and friends who have always been there for me. This accomplishment would not have been possible without any of them.

Table of Contents

Acknowledgements	iv
List of Tables	viii
List of Figures.....	ix
Abstract.....	xvi
Chapter 1 Introduction.....	1
1.1 Fault analysis using seismicity	1
1.2 Stress field in Oklahoma	2
1.3 Woodward cluster.....	2
1.4 Dynamic triggering.....	3
1.5 Structure of the thesis	3
Chapter 2 Seismogenic fault mapping.....	8
2.1 Introduction	8
2.2 Seismicity clustering	8
Data and results	10
2.3 Cluster classification	11
2.4 Fault geometry mapping.....	12
2.5 Discussion.....	14
2.6 Conclusion.....	15
Chapter 3 Regional stress state.....	26
3.1 Introduction	26
3.2 Stress inversion and results	27

Data and results	29
3.3 Optimal orientation of focal mechanisms and fault	30
Optimal focal plane	31
Optimally oriented faults based on $\sigma Hmax$ orientation	31
3.4 Fault stress state based on Mohr circle analysis	33
3.5 Discussion.....	34
3.6 Conclusion.....	38
Chapter 4 A case study: Woodward cluster	51
4.1 Introduction	51
4.2 Regional stress state in Woodward cluster	51
4.3 Seismicity migration.....	52
4.4 Coulomb Stress interaction.....	53
4.6 Discussion.....	55
4.7 Conclusion.....	55
Chapter 5 Dynamic triggering in Oklahoma	62
5.1 Introduction	62
5.2 Catalog study	62
5.3 Waveform study and analysis.....	64
5.4 Dynamic stress calculation	66
5.5 Magnitude calibration of detected events	67
5.6 Discussion.....	69
5.7 Conclusion.....	70

Conclusion	79
References	80
Appendix A: Seismogenic fault mapping results	88
Appendix B: Regional stress inversion results	90

List of Tables

Table 3-1: Fault stress state modeling parameters. [<i>Goertz-Allmann and Wiemer, 2012</i>]	50
Table 4-1 Cumulative rupture information for each stage.	61
Table 5-1 Mainshock information showing positive β statistic in Woodward area and calculated β using detected catalog.....	78
Table 5-2 Dynamic stress of each mainshock showing positive β statistic in Woodward area.	78

List of Figures

Figure 1-1. Mapped Oklahoma fault [<i>Holland, 2015</i>].	4
Figure 1-2. Overview of seismicity and fault distribution in Oklahoma. Red dots are seismicity relocations with $M > 2.8$ [<i>Chen, 2016</i>]. Green lines are mapped faults [<i>Holland, 2015</i>].	5
Figure 1-3. Maximum horizontal stress orientation map for Oklahoma by <i>Alt and Zoback</i> [2015]. Yellow dots are seismicity; blue lines are σ_{Hmax} orientation from image logs; green lines are σ_{Hmax} orientation from sonic dipole logs; white lines are σ_{Hmax} orientation from world stress map data.	6
Figure 1-4. Maximum horizontal stress orientation map by <i>Walsh and Zoback</i> [2016]. Red dots are earthquakes with $M > 3.0$; green lines are mapped faults [<i>Donald and Holland, 2015</i>].	7
Figure 2-1. Gutenberg-Richter relation of seismicity relocations of Oklahoma [<i>Chen, 2016</i>]. b value is 1.31 ± 0.12 ; magnitude completeness is 3.30 ± 0.39	16
Figure 2-2. (a) 2D histogram of T and R , white lines are threshold of η and R as 0.01 and 0.01 used in clustering; (b)(c)(d) histogram of η , R and T , respectively; red lines are the same threshold for η and R as in (a); no T threshold is applied in clustering.	17
Figure 2-3. Clustering results of seismicity relocations. Each cluster is represented by a different color. Thin red lines are mapped fault [<i>Holland, 2015</i>].	18
Figure 2-4. Cluster classification results with threshold $t_{max} = 0.5$ and $\mu = 5$	18

Figure 2-5. Seismicity distribution for Prague cluster; it is classified as an aftershock sequence; reds dots are events ascribed to the cluster (blue dots) because their closeness in time and location. The top panel shows magnitude-time distribution; the bottom panel shows the map view of the cluster.	19
Figure 2-6. Seismicity distribution of Pawnee cluster; it is classified as an aftershock sequence. The top panel shows magnitude-time distribution; the bottom panel shows the map view of the cluster.....	20
Figure 2-7. Seismicity distribution of Fairview cluster; it is classified as a swarm; red dots are events ascribed to the cluster (blue dots) because their closeness in time and location. The top panel shows magnitude-time distribution; the bottom panel shows the map view of the cluster.	21
Figure 2-8. Seismicity distribution of Woodward cluster; it is composed of 6 discrete sub-clusters; each is represented by a different color. The top panel shows magnitude-time distribution; the bottom panel shows the map view of the cluster.	22
Figure 2-9. Seismogenic fault map generated in this study (thick red line); thin red lines are mapped fault from <i>Holland</i> , [2015].....	23
Figure 2-10. (a) Fault length in logarithmic scale versus maximum magnitude in the corresponding cluster; (b) histogram of the fault length in logarithmic scale....	24
Figure 2-11. (a) Rose diagram of strike angle of seismogenic faults. (b) Histogram of dip angle of seismogenic faults. (c) Histogram of planarity of seismogenic faults.	25

Figure 3-1. 2D Mohr diagram showing 5 hypothetical faults in a 2D Mohr circle (left) numbered to correspond to their orientations on the map (right). Fault number 3 is closest to slip (black Mohr circle) in this stress field because the ratio of shear to effective normal stress is highest. Fault 2 and 4 could be triggered by modest changes in pore pressure (blue Mohr circle), and fault 1 and 5 would require the most pore pressure to slip (orange Mohr circle). [Walsh and Zoback, 2016] 39

Figure 3-2. Illustration of possible dimensions of the formal stress inversions performed with MSATSI stress inversion package from *Martínez - Garzón et al.* [2014]. 39

Figure 3-3. Maximum horizontal stress orientation map (left) (red: normal faulting; green: strike-slip; black: oblique faulting) and histogram σ_{Hmax} orientation(right)..... 40

Figure 3-4. Top: rose diagram of strike(a), histogram of dip(b) and rake angle (c) of original focal plane from OGS catalog. Bottom: rose diagram of strike(d), histogram of dip(e) and rake angle (f) of selected optimal focal plane based on stress orientation. NF: normal faulting; SS: strike slip faulting, RF: reverse faulting in (c) and (f). 41

Figure 3-5. Fault plane orientation relative to a given $\sigma_1 - \sigma_3$ stress field (left); θ is the angle between the normal of fault plane and σ_1 orientation; Mohr diagram of shear stress versus effective normal stress (right). 41

Figure 3-6. Left: rose diagram of δ between fault strike and uniform σ_{Hmax} orientation 85° . Right: rose diagram of δ between fault strike and nearest σ_{Hmax} orientation

from our inversion results. Dashed red lines denote the optimal range $[25^\circ, 39^\circ]$.

..... 42

Figure 3-7. Seismogenic fault map color-coded by δ , the angle between fault strike and

σ_{Hmax} orientation. Top: δ is calculated using uniform σ_{Hmax} orientation 85° .

Bottom: δ is calculated using nearest σ_{Hmax} orientation from our inversion

result. 43

Figure 3-8. Fault stress state calculated from Model 2. Scenario 1,2 and 3 are three

different ways to determine fault orientation to stress field (see the text). Blue

and red lines are the fault strength envelopes with $\mu = 0.6$, $\Delta P = 0$ and $\mu = 0.6$,

$\Delta P = 10MPa$, respectively. Each circle represents a seismogenic fault stress

state; red: fault stress state from scenario1; blue: fault stress state from scenario

2; green: fault stress state from scenario 3. Two dashed lines denote the optimal

orientation angle range with $2\theta \in [102^\circ, 130^\circ]$ 44

Figure 3-9. Focal mechanism distribution for Pawnee cluster. Color scheme for the

beach ball: green, strike-slip faulting; red, normal faulting; blue, reverse

faulting. A rose diagram of the strike of selected focal planes is shown in the

right corner. Red line is the inverted σ_{Hmax} orientation; green line is the strike of

M5.8 mainshock in Pawnee cluster; blue line is the seismogenic fault strike

orientation; the blue are green lines are consistent. 45

Figure 3-10. Focal mechanism distribution for Prague cluster. Color scheme for the

beach ball: green, strike-slip faulting; red, normal faulting; blue, reverse

faulting. A rose diagram of the strike of selected focal planes is shown in the

right corner. Red line is the inverted σ_{Hmax} orientation; green line is the strike of M5.7 mainshock in Prague cluster; blue line is the seismogenic fault strike orientation; the blue are green lines are consistent.....	46
Figure 3-11. Focal mechanism distribution for Fairview cluster. Color scheme for the beach ball: green, strike-slip faulting; red, normal faulting; blue, reverse faulting. A rose diagram of the strike of selected focal planes is shown in the right corner. Red line is the inverted σ_{Hmax} orientation; green line is the strike of M5.1 mainshock in Fairview cluster; blue line is the seismogenic fault strike orientation; the blue are green lines are overlaid.....	47
Figure 3-12. Histogram of standard deviation of σ_{Hmax} orientation.	48
Figure 3-13. Maximum horizontal compressive stress orientation map with uncertainties from bootstrap resampling (red: normal faulting; green: strike-slip faulting; black: oblique faulting). Gray lines are mapped fault [Holland, 2015]. Black dots show grids with standard deviation of σ_{Hmax} larger than 5° . The numbers under the black dots are the number of focal mechanism solutions available in that grid.....	49
Figure 4-1. Focal mechanism distribution in depth view (green: strike-slip faulting; red: normal faulting).	56
Figure 4-2. Flower structures in nature. Seismic profiles are of positive flower structures from the Aruba Gap Abyssal Plain, Colombia (left) and negative flower structure from the Andaman Sea (right). Vertical scale is in seconds of two-way travel time. [Guerroué and Cobbold, 2006].....	58

Figure 4-3. 3D view of seismogenic fault planes picked from seismicity distribution in Woodward cluster.....	58
Figure 4-4. Seismicity overview for Woodward cluster. Top: daily seismicity rate (blue lines) and cumulative moment curve (red lines); stages are denoted by blue dashed lines; each stage corresponds to a jump in cumulative moment curve. Bottom: magnitude distribution. Black dashed line denotes $M3.0$	59
Figure 4-5. Map view (top panel) and depth view (bottom panel) of seismicity of each stage shown in Figure 4-4. Red dots are events occurring in current stage, gray dots are events in previous stages.....	60
Figure 4-6. Coulomb Stress change resolved on seismogenic fault planes at each stage shown in Figure 4-5. (No focal mechanism information available in stage 3) ..	60
Figure 5-1. Mainshock distribution from 2010 to 2015 with $M_s > 6.5$, $depth < 100km$, and $PGV > 0.01cm/s$. There are 49 mainshocks used in continental U.S beta search.	71
Figure 5-2. Stacked beta (>2.0) map from 49 mainshocks shown in Figure 5-1. Gray dots are seismicity from ANSS catalog with $M>3.0$; yellow triangles are volcanoes; orange circles are geothermal fields in California.....	71
Figure 5-3. Mainshock distribution from 2010 to 2015 with $M_s > 6.5$, $depth < 100km$, and $PGV > 0.002cm/s$. There are 29 mainshocks used in Oklahoma beta search.	72
Figure 5-4. Stacked beta (>2.0) map from 29 mainshocks in Figure 5-3. Gray dots are earthquake locations from OGS catalog.....	72

Figure 5-5. Matched filter detection results of May 12 th , 2015 M7.3 earthquake shown on waveforms of station U32A, BHT component. Red dashed lines are detected events; (c) shows the waveform 5h before till 5h after the mainshock; (b) zooms into 2.5h after mainshock; (a) zooms into four detected events in surface wave in (b); (d) shows the spectrogram of (c).	73
Figure 5-6. Magnitude difference versus $\log_{10}(\alpha)$ for templates used in matched-filter detection. Top: before magnitude calibration; bottom: after magnitude calibration. The slope is the constant c in equation 5-6.	74
Figure 5-7. Magnitude distribution for detected events around May 12 th , 2015 M7.3 mainshock. Top: before calibration; bottom: after calibration.	75
Figure 5-8. Magnitude-time distribution of cataloged events in stage2 in figure 4-4. Dashed lines are large earthquakes that shows positive beta anomaly in stage2; blue means no triggering; red denotes the triggering event of May 12 th , 2015 M7.3 Nepal earthquake.	75
Figure 5-9. Seismicity rate within 24 hours of May 12 th , 2015 M7.3 mainshock (top) and March 29 th , 2015 M7.5 mainshock (bottom). Red line is the observation; black line is constant rate based on the seismicity rate before mainshock.....	76
Figure 5-10. Magnitude distribution of detected catalog for May 12 th , 2015 M7.3 mainshock (top) and March 29 th , 2015 M7.5 mainshock (bottom).....	77

Abstract

The recently increased seismicity in Oklahoma provides a rich catalog that delineates unmapped fault system. In this project, I identify 88 clusters with 20 or more earthquakes using automatic nearest-neighbor approach. It is assumed that each cluster nucleates on a preexisting fault segment; I manually pick the fault geometry and use a spectral decomposition method to get fault strike, dip and planarity. These seismogenic faults are steeply dipping ($>80^\circ$) and the dominant strikes are $50^\circ\sim60^\circ$ and $100^\circ\sim110^\circ$. To study the fault orientation to regional stress field, I invert the stress state from focal mechanism solutions using a linear stress inversion method. Most areas in Oklahoma show strike-slip faulting regime, while the north and northwest areas show a transtensional regime. By comparing the seismogenic fault orientation to regional stress orientation, I find that most newly reactivated seismogenic faults are optimally or moderately optimally oriented, thus posing a potential earthquake hazard. I show a case study of seismogenic fault in Woodward, Oklahoma. Three fault segments are picked from seismicity and both the main strike-slip fault and shallower normal fault are optimally oriented to regional stress field. I analyze the reactivation process of the fault system using seismicity migration and Coulomb Stress interaction. Finally, I search for dynamic triggering evidence in Oklahoma by both catalog search and waveform search. I find triggered events in Woodward cluster, Oklahoma by May 12th, 2015 M7.3 Nepal earthquake. The triggering stress threshold is as low as $1kPa$, suggesting the faults were critically loaded at the mainshock time.

Chapter 1 Introduction

1.1 Fault analysis using seismicity

Thousands of fault segments are compiled by Oklahoma Geological Survey (OGS) [Holland, 2015] (Figure1-1) from oil and gas industry data and published literature. However, a large portion of seismicity in Oklahoma does not occur on mapped faults (Figure1-2). So, in this study, I use the rich earthquake information to delineate the currently active faults in Oklahoma. Many earthquakes form clusters and several large clusters have been studied to map fault system. The November 6th, 2011 M_w 5.7 Prague earthquake sequence has been studied and linked to disposal wells which are only a few hundred meters away from the closest earthquakes [Keranen *et al.*, 2013]; the aftershock sequence is used to delineate the rupture zone as narrow, steeply dipping surface in both the sedimentary section and basement; two of the three rupture segments correlate well with the previously mapped Wilzetta fault zone, the other defines a secondary orientation. The slip on the three mainshocks is consistent with an east-northeast direction of maximum horizontal stress. The February 13th, 2016 M_w 5.1 Fairview earthquake is another large earthquake potentially induced by waste water injection in Oklahoma [Yeck *et al.*, 2016]. Affected by the 12km northeast high-rate injection zone, the cluster started in late 2015 and migrates to southwest. The seismicity in Fairview cluster is used to map a preexisting fault with strikes and dips between approximately 40°~48° and 70°~80°, respectively. The September 3rd, 2016 M_w 5.8 Pawnee earthquake occurred on a previously unknown left-lateral strike-slip basement fault that intersects the mapped conjugate Labette fault zone [Yeck *et al.*, 2016].

1.2 Stress field in Oklahoma

The regional stress information can help identify some optimally oriented faults and hence identify some potential earthquake hazards [Holland, 2013]. An in-situ stress map of Oklahoma is developed by *Alt and Zoback* [2015] by utilizing wellbore image logs and shear-velocity anisotropy measurements from sonic dipole data provided by the oil and gas industry. The map reveals a uniform ENE direction (Figure1-3) of maximum horizontal compressive stress (σ_{Hmax}). *Walsh and Zoback* [2016] generate a fairly uniform map of σ_{Hmax} orientation from focal mechanism inversion (Figure1-4). The orientation of σ_{Hmax} is 83° with standard deviation less than 4° , but one grid in the north shows a larger difference at 73° . Despite the ‘uniform’ stress field, the trends of seismicity distribution which are assumed to represent currently active fault segments show a large variability of orientations (Figure1-2). So, the idea of ‘uniform’ stress orientation might be an oversimplified result by lack of data. I use a large number of focal mechanisms to generate a detailed map of stress field by using a linear stress inversion method by *Martínez-Garzón et al.* [2014]. The regional stress field can be used to identify preexisting faults that are optimally oriented and potentially active.

1.3 Woodward cluster

Several large clusters in Oklahoma have been studied after a large earthquake ($M > 5.0$) occurred [Keranen et al., 2013; Yeck et al., 2016]; Woodward cluster is one of the largest, isolated clusters in northwest Oklahoma but without any earthquakes larger than $M4.0$ so far, and the seismicity migration pattern shows complexity in the cluster. I will use Woodward cluster as a case study to demonstrate how the regional stress field

affects fault activities. I also study the characteristics of seismicity distribution, stress interaction and potential earthquake hazard in Woodward cluster.

1.4 Dynamic triggering

Dynamic triggering is one of earthquake triggering mechanisms that describes earthquakes triggered by the transient stress perturbation from surface wave of large ($M > 6.5$), remote earthquakes. Dynamic triggering has been observed in a variety of environments; many of these observations are from active volcanic and hydrothermal areas [Brodsky *et al.*, 2000; Power *et al.*, 2001; Prejean *et al.*, 2004]. Recent research extends triggering to fluid-injection areas [van der Elst *et al.*, 2013] where February 2010 M_w 8.8 Maule earthquake has been found triggering a strong earthquake sequence which could continue up to the time of the first M4.7 earthquake in Prague cluster. Areas with suspected anthropogenic earthquakes are also more susceptible to earthquake triggering from natural transient stresses [van der Elst *et al.*, 2013]. In this study, I perform a systematic search for dynamic triggering evidence in fluid-injection areas in Oklahoma. This study is kind of independent from the study of seismogenic faults. On the other hand, dynamic triggering susceptibility suggests the presence of critically loaded faults and potentially high fluid pressures [van der Elst *et al.*, 2013]. So, the dynamic triggering can be used as a probe to the fault stress state. The triggering stress threshold is usually low which can help identify some critically loaded faults.

1.5 Structure of the thesis

In Chapter 2, I characterize unmapped fault geometry and orientation parameters using earthquake location information. In Chapter 3, I invert regional stress state from focal

mechanism solutions and study the nature of the seismogenic faults. In Chapter 4, I show a case study of Woodward fault system; the reactivation process of the fault is analyzed using seismicity migration and Coulomb Stress interaction. In Chapter 5, I perform a systematic search for dynamic triggering evidence in Oklahoma; this part is relatively independent from seismogenic fault study; however, the triggering evidence suggests the existence of critically loaded faults.

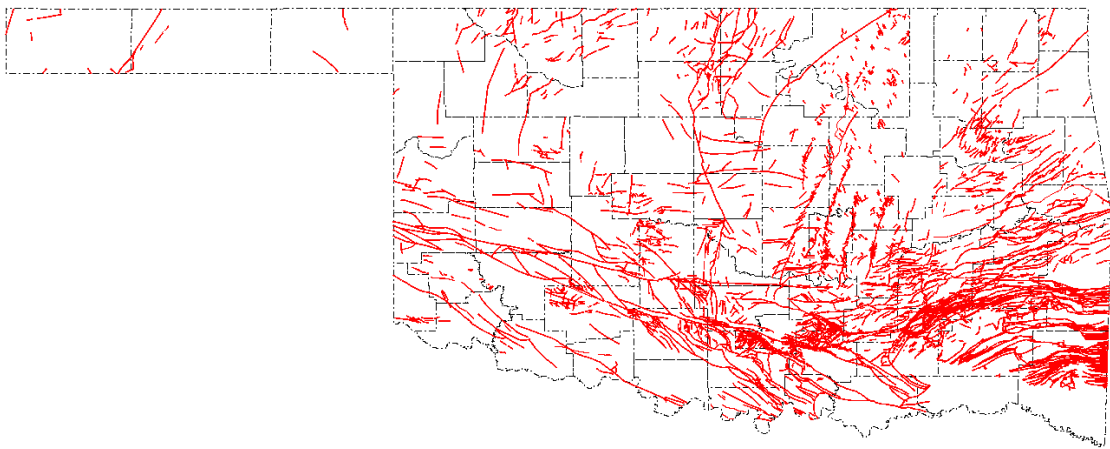


Figure 1-1. Mapped Oklahoma fault [*Holland, 2015*].

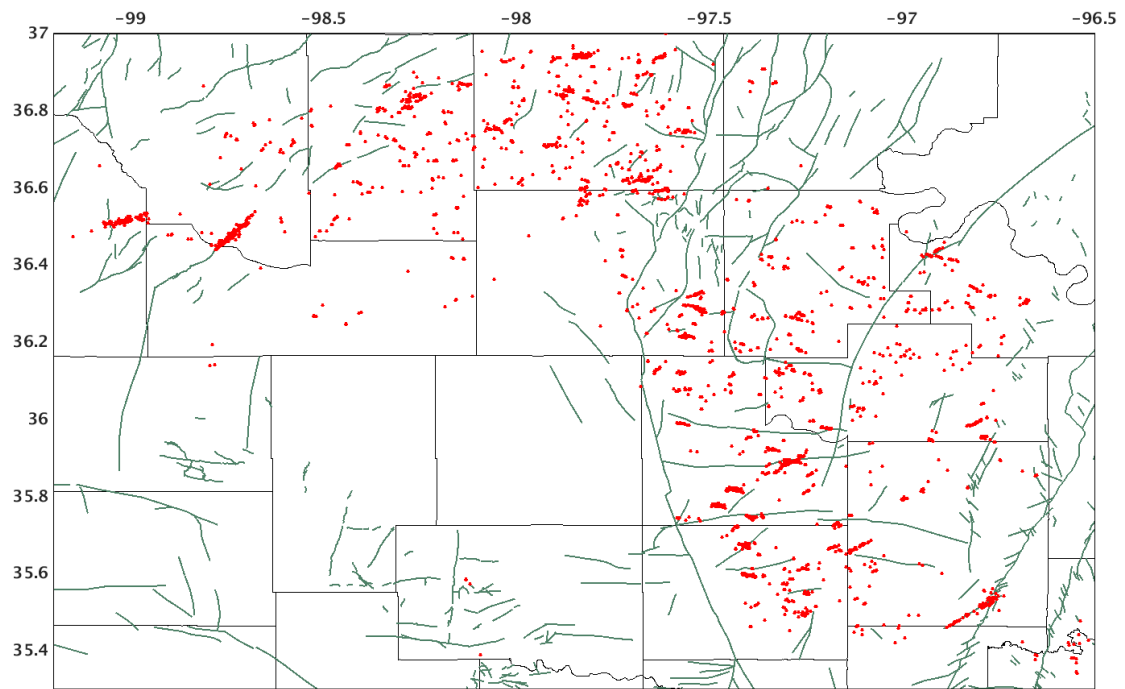


Figure 1-2. Overview of seismicity and fault distribution in Oklahoma. Red dots are seismicity relocations with $M > 2.8$ [Chen, 2016]. Green lines are mapped faults [Holland, 2015].

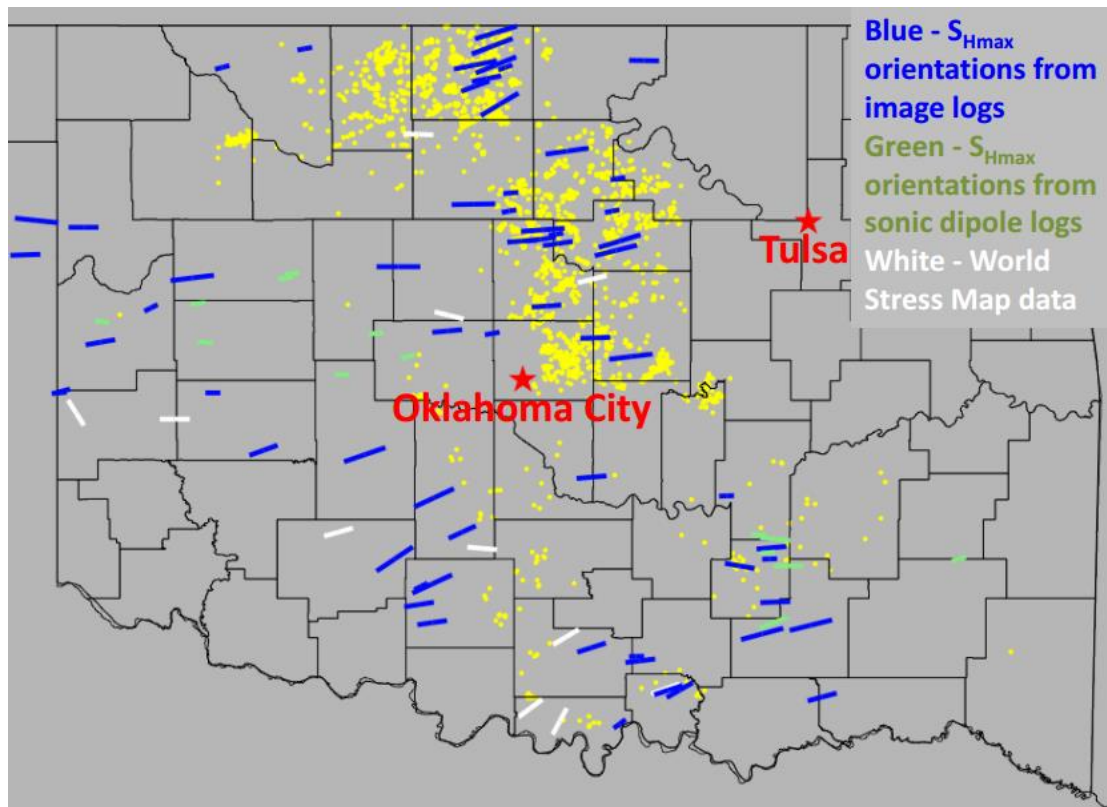


Figure 1-3. Maximum horizontal stress orientation map for Oklahoma by *Alt and Zoback* [2015]. Yellow dots are seismicity; blue lines are σ_{Hmax} orientation from image logs; green lines are σ_{Hmax} orientation from sonic dipole logs; white lines are σ_{Hmax} orientation from world stress map data.

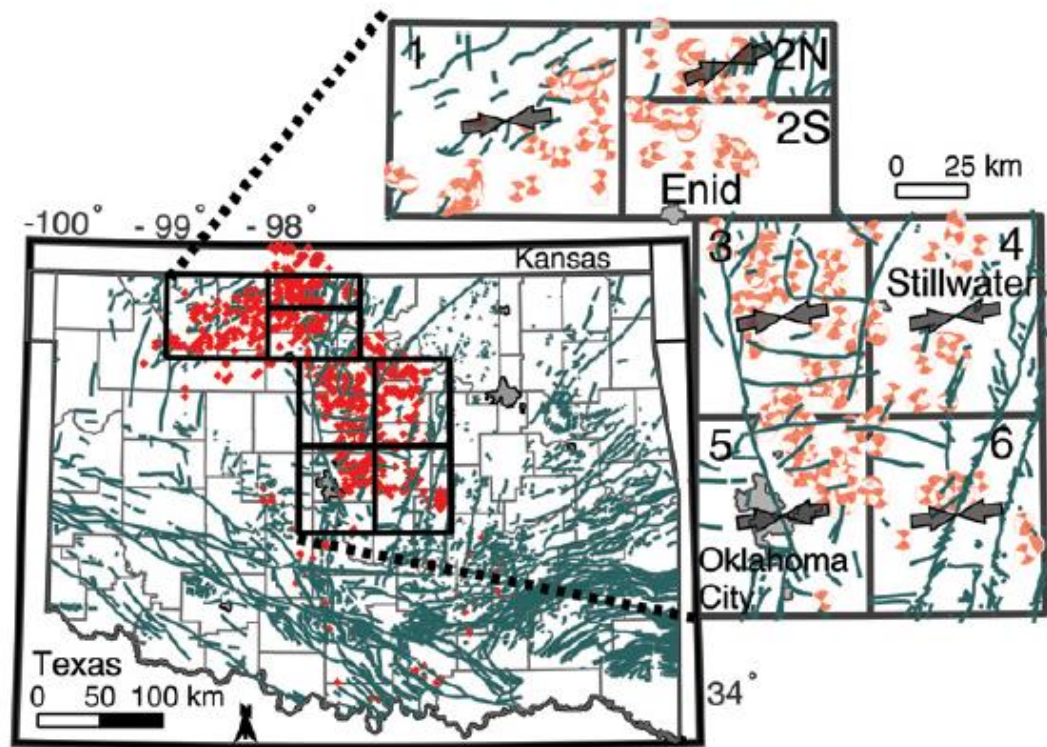


Figure 1-4. Maximum horizontal stress orientation map by *Walsh and Zoback* [2016]. Red dots are earthquakes with $M > 3.0$; green lines are mapped faults [*Donald and Holland*, 2015].

Chapter 2 Seismogenic fault mapping

2.1 Introduction

The preliminary fault map of Oklahoma [*Holland*, 2015] is the current reference fault map for many researches. The mapped faults are compiled from oil and gas industry data and published literature, which do not include any depth information. Seismicity rate in Oklahoma has been increased dramatically, but a large portion of seismicity does not nucleate on mapped faults. Since most of the earthquakes distribute into linear trends, I assume those earthquakes occur on some reactivated, preexisting but unmapped faults. The seismic activities provide rich information to delineate the unmapped fault system. In this chapter, I first use a nearest-neighbor approach [*Zaliapin and Ben-Zion*, 2013a] to automatically identify earthquake clusters and classify the clusters into different types based on the magnitude-time distribution that may represent different failure processes. I manually pick the seismogenic fault from each cluster to get the fault strike, dip and planarity using a spectral decomposition method; these faults could be mapped or unmapped.

2.2 Seismicity clustering

Earthquake clustering is an essential characteristic of seismicity with signature of space, time and size. Clustering in space is exemplified by the concentration of earthquakes along boundaries of major tectonic plates and regional fault networks [e.g., *Scholz*, 2002; *Utsu*, 2002]. Clustering in time is best seen as a significant increase of seismicity immediately after large earthquakes leading to aftershock sequences [*Omori*, 1894; *Utsu*, 1961; *Utsu et al.*, 1995; *Kisslinger*, 1996]. Earthquake swarms, foreshocks, bursts,

gaps and switching of seismicity activity among spatio-temporal domains are also used to denote different types of seismic clustering [Richter, 1958; Jones and Molnar, 1979; Romanowicz, 1993; Utsu, 2002; Felzer and Brodsky, 2006; Vidale *et al.*, 2006; Vidale and Shearer, 2006; Ben-Zion, 2008; Shearer, 2012]. To automatically separate earthquake clusters from randomly occurring background seismicity, I use nearest-neighbor approach [Zaliapin and Ben-Zion, 2013a]. The distance η between two events is defined as:

$$\eta_{ij} = dt_{ij} \cdot dr_{ij}^{df} \cdot 10^{-bm_i} \quad (2-1)$$

where dt_{ij} is the time separation between the two events i, j , $dt_{ij} = t_i - t_j$; dr_{ij} is the 3-D space separation $dr_{ij} = |\vec{r}_i - \vec{r}_j|$ and df is the fractal dimension of the earthquake hypocenter distribution; m_i is the magnitude of parent event i . In this project, I compute the distance η with parameter $df = 1.6$ following Zaliapin & Ben-Zion [2013a].

It will be convenient to represent the scalar distance η in terms of its space and time components normalized by the magnitude of the parent event i [Zaliapin *et al.*, 2008]:

$$\begin{cases} T_{ij} = dt_{ij} \cdot 10^{-q \cdot b \cdot m_i} \\ R_{ij} = dr_{ij}^{df} \cdot 10^{-(1-q) \cdot b \cdot m_i} \end{cases} \quad (2-2)$$

It is readily seen that $\eta_{ij} = T_{ij}R_{ij}$. In this work, I use the scale of magnitude $q=0.5$ [Zaliapin & Ben-Zion 2013a]. b value is from Gutenberg-Richter law, $b=1.3$ for Oklahoma seismicity as shown in Figure 2-1.

Earthquake origin time and locations are used as input in this method; then the distance η between each pair of events is calculated. We set up distance threshold to separate the earthquakes into clusters. Figure 2-2(a) shows the 2D distribution of T and R ; the area

with small R and small T means those events are close to each other both in time and space; it represents the clusters. The areas with large R or large T value represent background seismicity. Figure 2-2(a) shows that not much seismicity occurs in the background as shown in seismicity map in Figure 1-2, so I lower the threshold of η and R to separate small clusters. Distance R is a bimodal distribution and T distribution is unimodal in the histogram of R and T shown in Figure 2-2(c) and (d), which suggests R is more sensitive than T to separate clusters. Because the seismicity in some clusters can last long time or show some bursts in time, I didn't apply T threshold in the clustering.

Data and results

I use the relocated 16,899 earthquakes [Chen, 2016] in Oklahoma from 2010 to 2016 as input to generate clusters. Because the approach is insensitive to the catalog incompleteness [Zaliapin and Ben-Zion, 2013a], I first use magnitude cutoff 2.5, which is a little lower than magnitude completeness 3.3 shown in Figure 2-1, to cluster the seismicity and find that 3195 of 7239 earthquakes with magnitude larger than 2.5 can be separated into 140 clusters. To get more complete clusters, I run the clustering program without magnitude cutoff and find that 8371 out of 16899 earthquakes are separated into 255 clusters and the others are viewed as background seismicity. The clustering results without magnitude cutoff can separate both large and small clusters seen in the results with magnitude cutoff, so I use the latter results with more complete clusters in the following analysis. Figure 2-3 shows the clustering results from a threshold combination of η as 0.01 and R as 0.01 shown in Figure 2-2 (b) and (c). I get 54 clusters with 25 or more events in each cluster and 88 clusters with 20 or more events in each

cluster. The large clusters in Fairview and Pawnee are well separated; Prague is separated into two clusters because the southwestern part ruptured much earlier than the northeastern part; Woodward clusters is divided into six discrete small clusters, which suggests the complexity of Woodward fault systems. More than 70 relatively small clusters are identified in central and northern Oklahoma and the clusters are separated well and do not intersect with each other. I will use these clustering results to continue the analysis.

2.3 Cluster classification

Clusters can be classified into subtypes based on their magnitude-time distribution and the subtypes can be related to tectonic processes. Aftershock sequences and swarms are commonly occurred clusters. I use two parameters to classify the clusters: the timing of the largest event t_{max} normalized by the median value and skewness of moment release μ :

$$t_{max} = \frac{t_{main} - t_{first}}{t_{median} - t_{first}} \quad (2-3)$$

$$\mu = \frac{\sum_1^N (t_i - t^*)^3 m_i}{\sigma^3} \quad (2-4)$$

where t_{main} is the occurrence time of the largest event in each cluster; t_{first} is the occurrence time of the first event in each cluster; t_{median} is the median value of occurrence time in each cluster; t^* is the centroid occurrence time, the mean value of t_i weighted by moment release (M_i), $t^* = \frac{\sum_1^N t_i M_i}{\sum_1^N M_i}$; m_i is the normalized moment, $m_i =$

$\frac{M_0(i)}{\sum_1^N M_0(i)}$; M_0 is the seismic moment estimated from magnitude, $M_0 = 10^{1.5mag+16.1}$; σ is

the standard deviation of central moment, $\sigma^2 = \sum_1^N (t_i - t^*)^2 m_i$.

Aftershock sequences usually start with the largest event, so they will be characterized by a small t_{max} and large positive skewness because of the long tail of aftershock

distribution on the positive side. While for swarm sequences, the largest event usually occurs later than that of aftershock sequences and the cluster will be characterized by

relatively large t_{max} and small skewness which means no significantly skewed

distribution. For our classification, I select thresholds for t_{max} and skewness μ as 0.5

[Zhang and Shearer, 2016; Cheng, 2016] and 5 [Roland and McGuire, 2009]

respectively. Using the thresholds on the 54 clusters with 25 or more events, I find 5

aftershock sequences, 33 swarms, 12 mixtures, and 4 foreshocks sequences as shown in

Figure 2-4. The classification of some large clusters are consistent with previous studies

[Keranen et al., 2016; Yeck et al., 2016]; Prague and Pawnee cluster are classified as

aftershock sequences as shown in Figure 2-5 and Figure 2-6; Fairview is classified as

swarm cluster (Figure 2-7) in which the largest event occurred three months after the

seismicity had started in the cluster; and Woodward is composed of six discrete clusters

(Figure 2-8), which suggests the complexity of seismicity distribution in this cluster.

2.4 Fault geometry mapping

Earthquakes tend to occur on fault plane and the distribution of earthquakes will spread

out along the fault strike and dip direction, in which event locations will show the

largest variance. I use the spectral decomposition method [Vidale and Shearer, 2006] to

find the direction of largest and smallest variance. First, for each cluster with 20 or more events, I create a 3×3 covariance matrix D of event locations;

$$D = \begin{pmatrix} E(x^2) & E(xy) & E(xz) \\ E(yx) & E(y^2) & E(yz) \\ E(zx) & E(zy) & E(z^2) \end{pmatrix} \quad (2-5)$$

where x and y are converted from longitude and latitude to kilometers relative to the cluster mean location, z is depth in kilometers relative to the cluster mean depth; then I calculate the eigenvalues ($\lambda_1, \lambda_2, \lambda_3$) and corresponding eigenvectors (U_1, U_2, U_3) of the covariance matrix. The shape of the seismicity cluster can be characterized by the relative size of eigenvalues. A nearly spherical distribution of events has $\lambda_1 \approx \lambda_2 \approx \lambda_3$; a plane distribution is characterized by $\lambda_3 \ll \lambda_1, \lambda_2$ with U_3 orthogonal to the plane; a linear distribution has $\lambda_1 \gg \lambda_2, \lambda_3$ with U_1 defining the direction of the line [Vidale and Shearer, 2006]. We define the planarity of seismicity hypocenters to be $1 - \lambda_3/\lambda_2$ [Vidale, 1986]. At its extremes, planarity of 1 indicates perfect planar alignment and planarity of 0 indicates a similar width and depth of seismicity cloud, whatever the length [Vidale and Shearer, 2006]. The fault strike and dip angle can be calculated using the eigenvector of the smallest eigenvalue.

$$\text{strike} \sim \text{atan}\left(\frac{U_3(2)}{U_3(1)}\right) \quad (2-6)$$

$$\text{dip} \sim \text{atan}\left(\frac{\sqrt{U_3(1)^2 + U_3(2)^2}}{U_3(3)}\right) \quad (2-7)$$

where $U3$ is the eigenvector of the smallest eigenvalue. I assume the first two eigenvectors $U1$, $U2$ can represent the fault plane, and $U3$ is perpendicular to the fault plane.

For each potential fault segment, I manually pick the start and end point of fault based on seismicity distribution. The top and bottom depth of the fault are 10th and 90th percentile of the depth distribution in each cluster. I picked 88 seismogenic faults (Figure 2-9) and the fault geometries are listed in Appendix A. To better know about the faults, I plot several parameters of the faults. Figure 2-10(a) shows a log-linear relation between fault length and maximum magnitude in each cluster; the histogram of fault length in Figure 2-10(b) shows that most of the faults are in the range $[10^0, 10^{0.6}]$ km; referring to the log-linear relation in Figure 2-10(a) the expected potential maximum magnitude will be 3.2 to 4.4 for the seismogenic faults. The strike angle of seismogenic faults mainly distributes in two bins of $[50^\circ \sim 60^\circ]$ and $[110^\circ \sim 120^\circ]$, which form a conjugate fault pattern as shown in Figure 2-11(a); most of the dip angle of seismogenic faults are larger than 80° , suggesting the seismogenic faults are steeply dipping faults (Figure 2-11b); Figure 2-11(c) shows that most of the faults have plane geometry with planarity larger than 0.6, which confirms my assumption in calculation that the eigenvectors $U1$ and $U2$ can be used to represent fault plane and $U3$ is perpendicular to the fault plane.

2.5 Discussion

We pick the ‘fault plane’ under the assumption that the seismicity plane can represent fault plane, which is not always the case. The seismicity plane could be a structural

feature, like a weak zone or a fluid conduit that facilitates the occurrence of seismicity. However, we observed that some clusters (e.g., Pawnee cluster) show a conjugate fault pattern; some (e.g., Fairview cluster) show an extension of mapped fault; some clusters (e.g., Prague cluster) nucleate on or near mapped fault. These evidences give us more confidence to pick the fault plane from seismicity distribution. We can further verify the existence of smaller faults with seismic data or well log observation data.

The decomposition method is sensitive to outlier of data when the cluster is small. I manually ‘cleaned’ small clusters to exclude some outliers if a potential fault segment is distinguishable. Then the cleaned cluster is used to calculate a more accurate fault strike, dip and planarity. I compare the fault strike to the nearby focal mechanism solutions to verify that the strike is in the right trend, but the focal mechanism information is not used in fault mapping.

2.6 Conclusion

Seismicity distribution in Oklahoma shows characteristics of clustering and I identify the clusters using nearest-neighbor approach. Those clusters can be classified into different types based on their magnitude-time distribution. Of 54 identified clusters with more than 25 events, there are 33 swarms and 5 aftershocks. Swarm-like clusters are dominant in Oklahoma, which are largely defined by smaller earthquakes. Most of the clusters have linear distribution and can be assumed to represent a potential fault segment. I pick 88 fault segments from clusters with more than 20 events and calculate the fault strike, dip and planarity using spectral decomposition method. There is a log-linear relation between fault length and maximum magnitude of earthquakes on that

potential fault plane; most of the fault length is $10^0 \sim 10^{0.6}$ km and the expected largest magnitude is 3.2~4.4. Large clusters like Prague and Fairview are expected to have larger earthquakes ($M > 5.0$), which are consistent with the real case. The planarity (>0.6) shows that the seismicity distribution in clusters is planar; most of these seismogenic faults are steeply dipping ($>80^\circ$), and the dominant strike is around $[50^\circ \sim 60^\circ]$ and $[110^\circ \sim 120^\circ]$, which form a conjugate pattern relative to an 85° stress orientation.

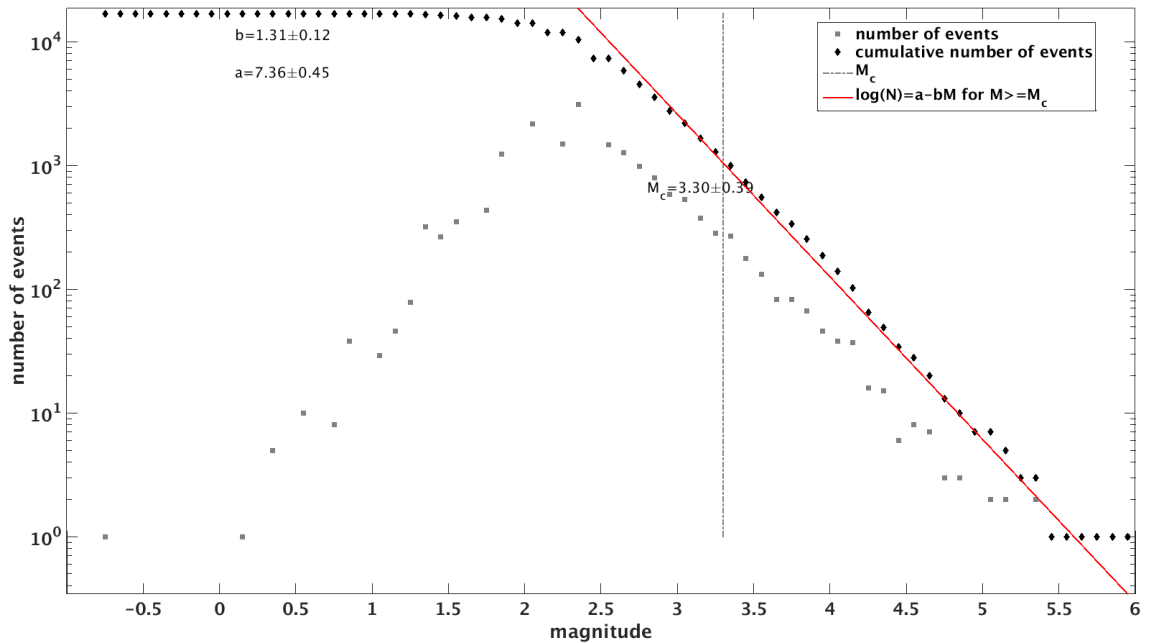


Figure 2-1. Gutenberg-Richter relation of seismicity relocations of Oklahoma [Chen, 2016]. b value is 1.31 ± 0.12 ; magnitude completeness is 3.30 ± 0.39 .

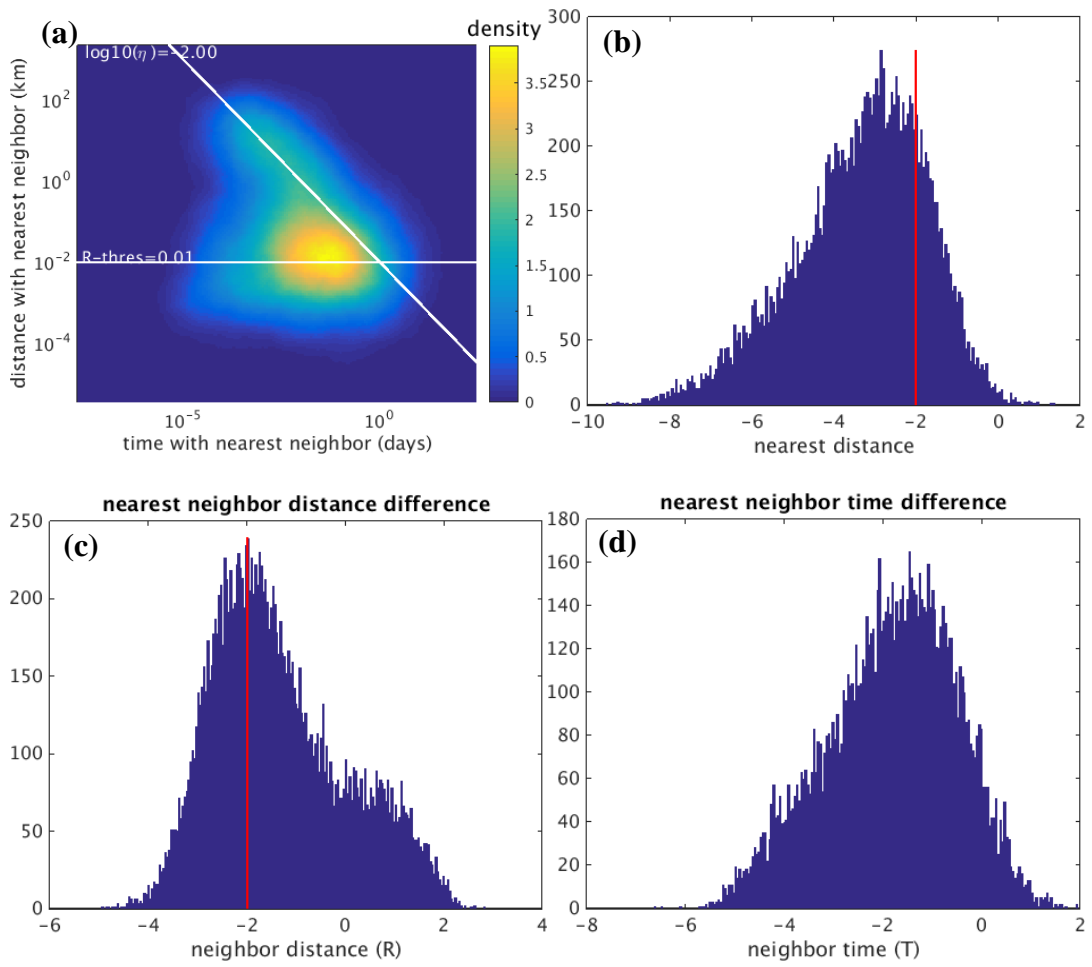


Figure 2-2. (a) 2D histogram of T and R , white lines are threshold of η and R as 0.01 and 0.01 used in clustering; (b)(c)(d) histogram of η , R and T , respectively; red lines are the same threshold for η and R as in (a); no T threshold is applied in clustering.

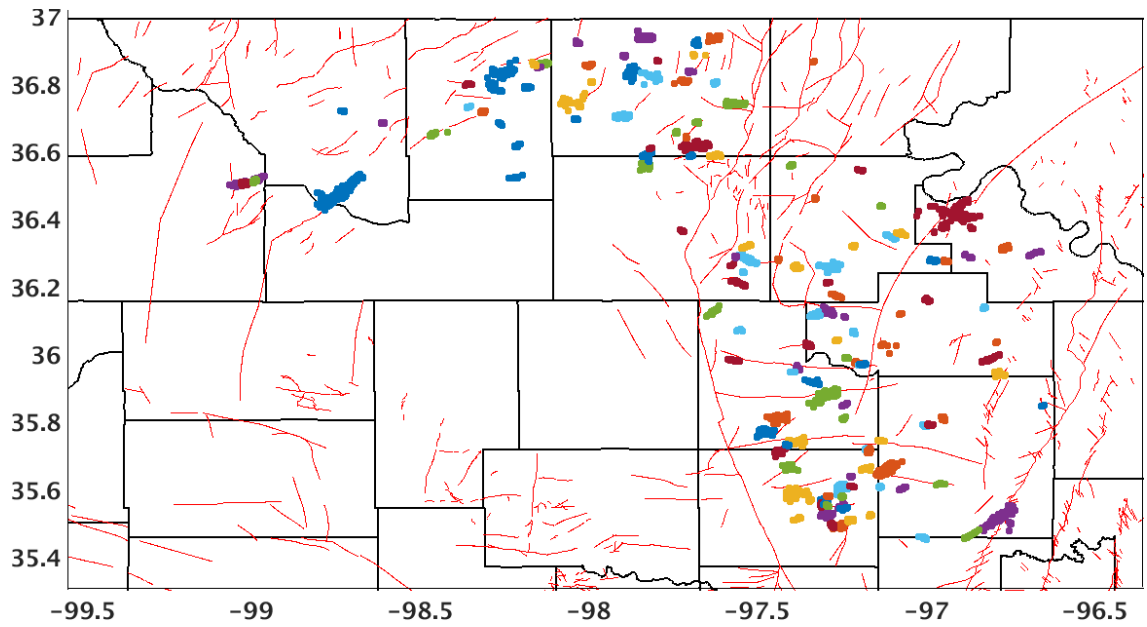


Figure 2-3. Clustering results of seismicity relocations. Each cluster is represented by a different color. Thin red lines are mapped fault [Holland, 2015].

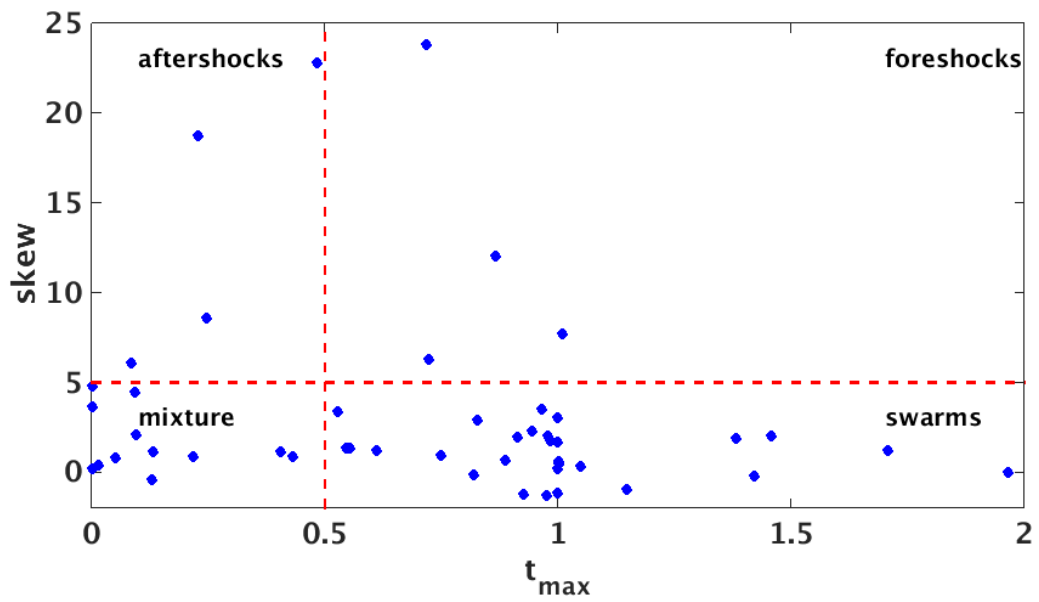


Figure 2-4. Cluster classification results with threshold $t_{max} = 0.5$ and $\mu = 5$.

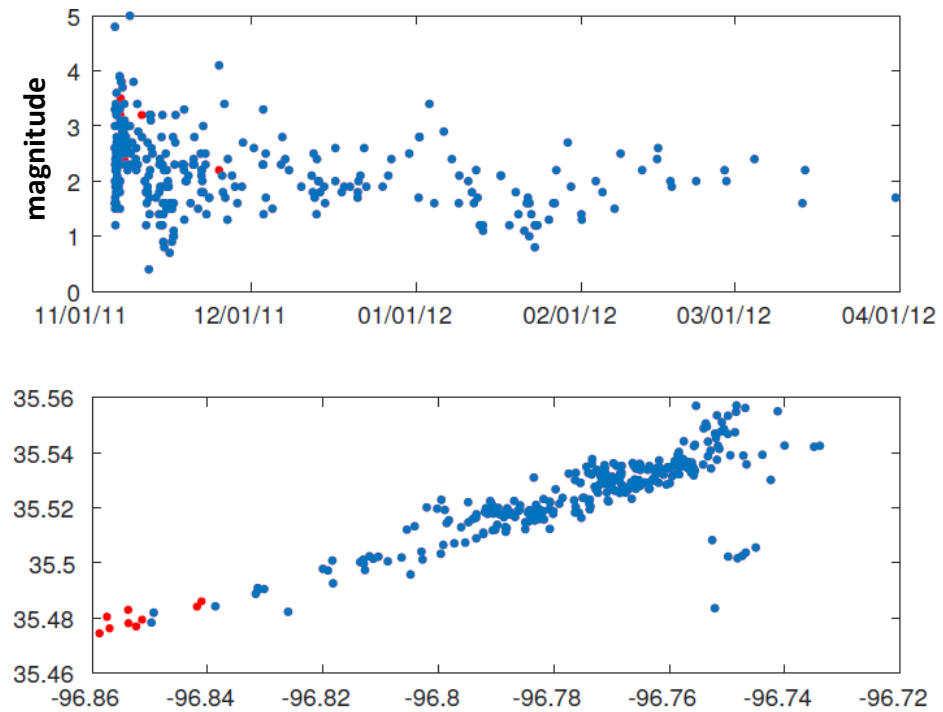


Figure 2-5. Seismicity distribution for Prague cluster; it is classified as an aftershock sequence; reds dots are events ascribed to the cluster (blue dots) because their closeness in time and location. The top panel shows magnitude-time distribution; the bottom panel shows the map view of the cluster.

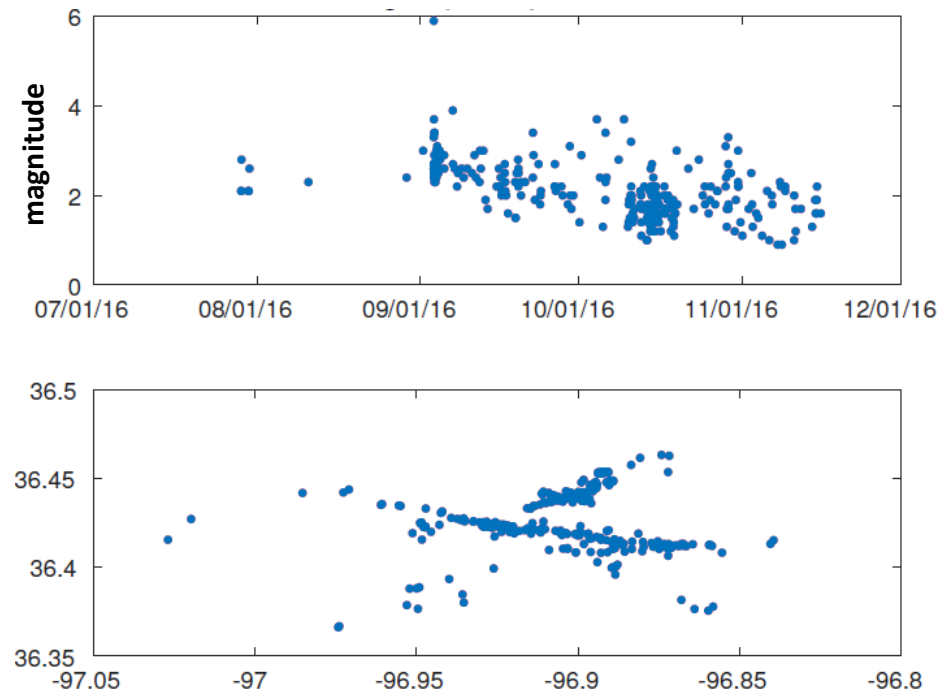


Figure 2-6. Seismicity distribution of Pawnee cluster; it is classified as an aftershock sequence. The top panel shows magnitude-time distribution; the bottom panel shows the map view of the cluster.

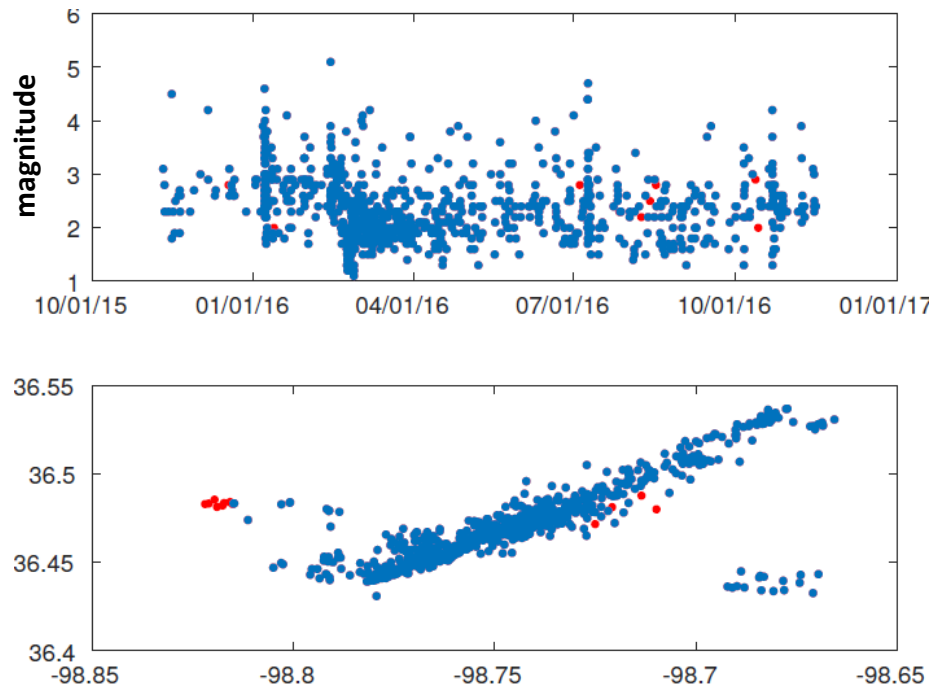


Figure 2-7. Seismicity distribution of Fairview cluster; it is classified as a swarm; red dotes are events ascribed to the cluster (blue dots) because their closeness in time and location. The top panel shows magnitude-time distribution; the bottom panel shows the map view of the cluster.

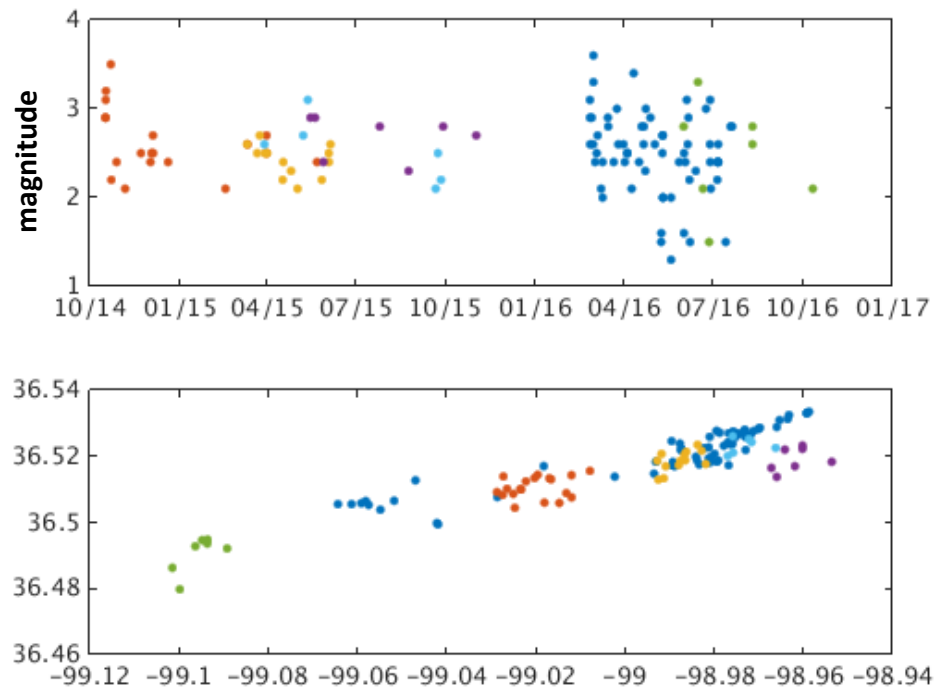


Figure 2-8. Seismicity distribution of Woodward cluster; it is composed of 6 discrete sub-clusters; each is represented by a different color. The top panel shows magnitude-time distribution; the bottom panel shows the map view of the cluster.

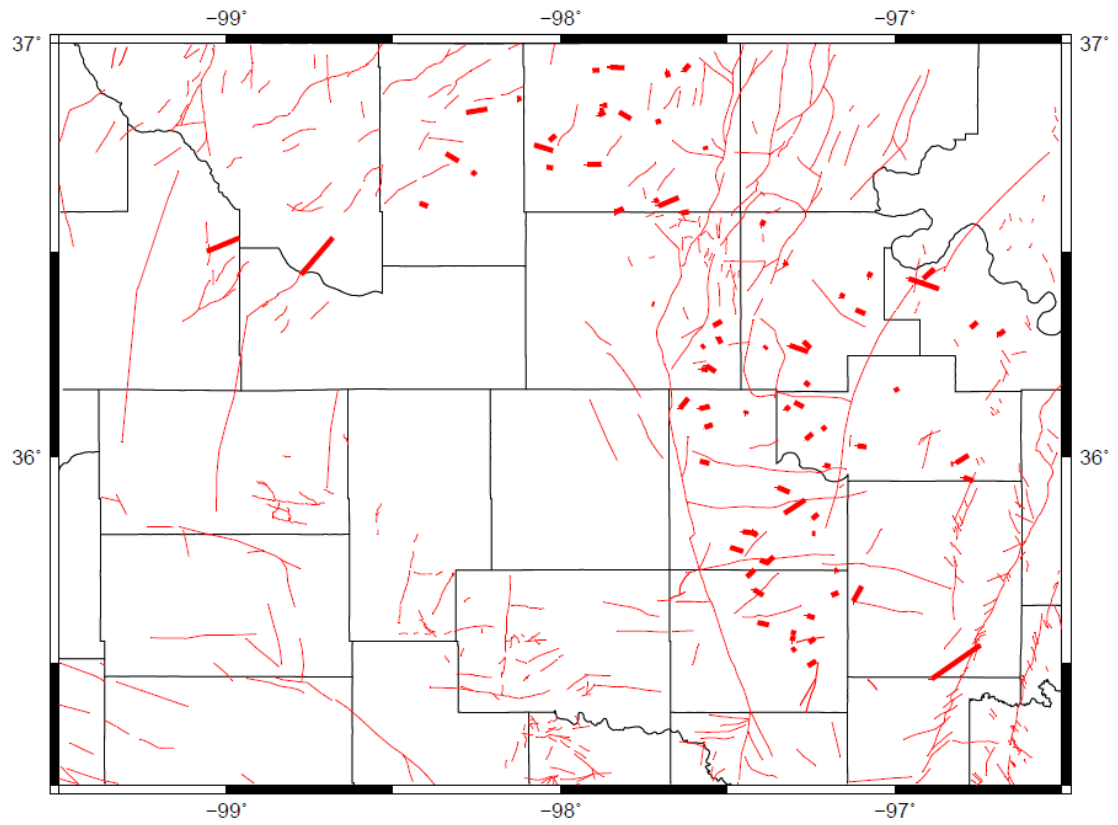


Figure 2-9. Seismogenic fault map generated in this study (thick red line); thin red lines are mapped fault from *Holland* [2015].

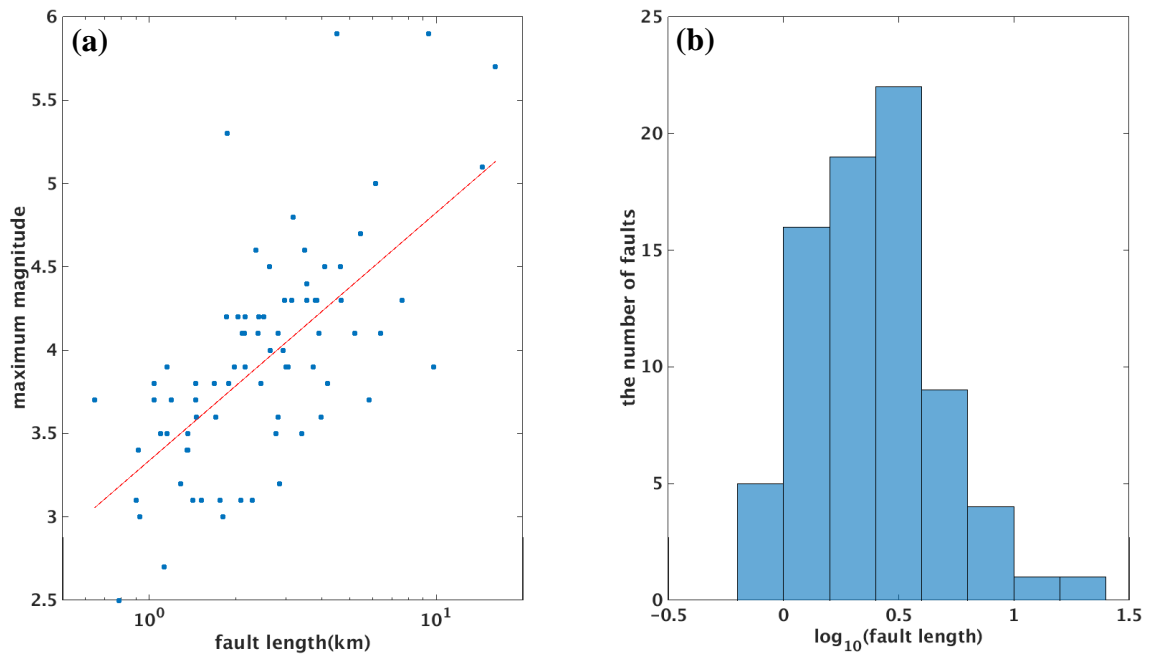


Figure 2-10. (a) Fault length in logarithmic scale versus maximum magnitude in the corresponding cluster; (b) histogram of the fault length in logarithmic scale.

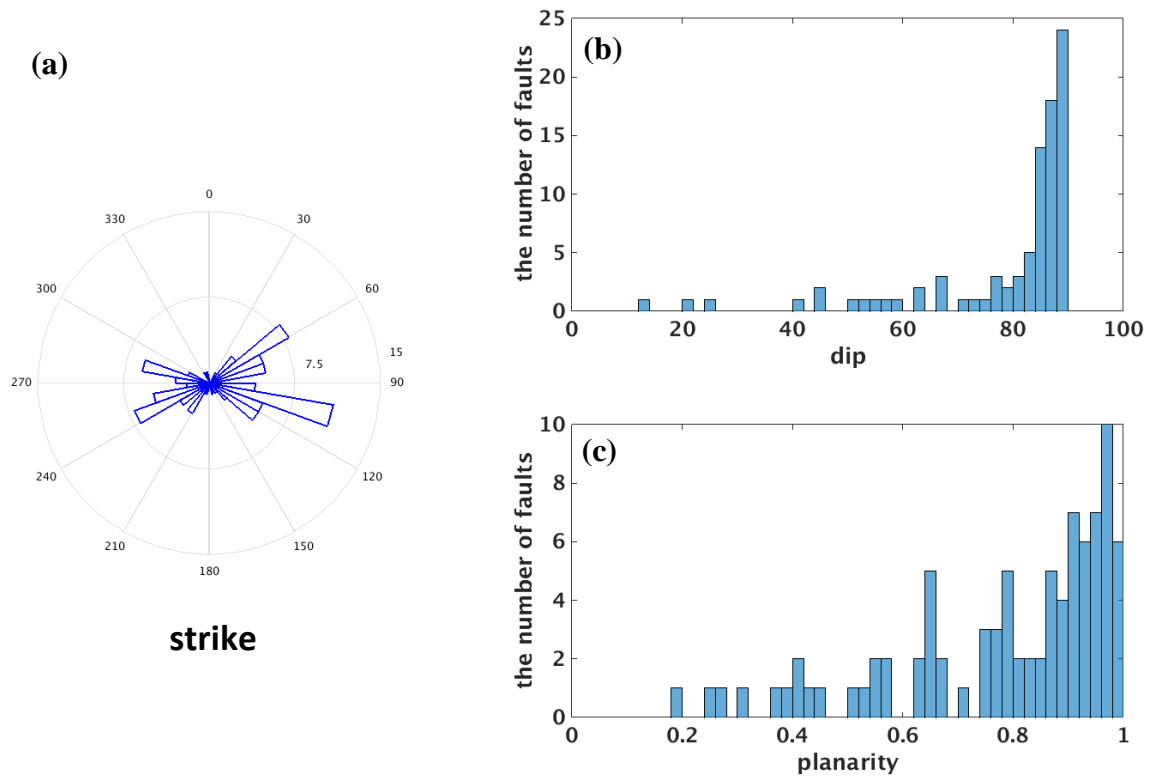


Figure 2-11. (a) Rose diagram of strike angle of seismogenic faults. (b) Histogram of dip angle of seismogenic faults. (c) Histogram of planarity of seismogenic faults.

Chapter 3 Regional stress state

3.1 Introduction

A lot of seismic activities in Oklahoma have been linked to fluid-injection [*Keranen et al.*, 2013; *Keranen et al.*, 2014; *Yeck et al.*, 2016]. The mechanism can be well explained by Coulomb failure criterion and Mohr circle: fluid injection will increase pore pressure, reduce effective normal stress and shift the Mohr circle to the left; when the Mohr circle is tangential to Coulomb failure envelope, the fault will fail. In theory (Figure 3-1), under a given stress field, the optimally orientated faults will firstly rupture when pore pressure increases. And moderately optimally oriented faults and sub-optimally oriented faults will only rupture when pore pressure increases more. Previous studies [*Holland* 2015; *Walsh and Zoback*, 2016; *Qi*, 2016] have shown that Oklahoma is under a relatively uniform stress regime that the maximum horizontal compressive stress σ_{Hmax} orientation is 85° , while the orientation of seismogenic faults shows a larger range of variability from the analysis in chapter2. The reason can be that under a uniform σ_{Hmax} orientation, some moderately optimally oriented faults or sub-optimally oriented faults might have ruptured in Oklahoma, or the ruptured faults are optimally oriented if the heterogeneity of σ_{Hmax} orientation is taken into consideration. It requires more detailed information on the stress field to reconcile the paradox of uniform σ_{Hmax} and variable seismogenic fault orientations. Using a new set of focal mechanism data from the Oklahoma Geological Survey (OGS), I generate the stress map with higher spatial resolution. Then I analyze the seismogenic fault orientation

relative to newly inverted σ_{Hmax} orientation map and find out how these reactivated faults are oriented.

3.2 Stress inversion and results

The estimation of the stress-field orientation from focal mechanism of earthquakes is a relevant tool to understand crustal mechanics and the physics of earthquakes. In global seismology, Formal Stress Inversion (FSI) is a well-established technique to study tectonic processes [e.g., *Hardebeck and Michael*, 2014; *Yoshida et al.*, 2012]. Most of the developed FSI method share two-assumptions:

1. The stress field is homogeneous within the considered rock volume.
2. The slip of the fault is parallel to the direction of the tangential traction [*Wallace*, 1951; *Bott*, 1955].

I choose the MSATSI software package [*Martínez-Garzón et al.*, 2014] which allows the FSI to be used in MATLAB. In nature, the transition between two different states of stress must be continuous. However, during the investigation of a distribution of stress-field orientations the obtained stress tensor might depend on the way that the input data are bound [e.g., *Hardebeck and Michael*, 2004; *Townend and Zoback*, 2004]. Different from single event inversion, the input focal mechanisms are grouped into subareas ('grid point') distributed over different dimensions (Figure3-2) and a stress tensor is inverted for each grid point simultaneously using least-square inversion scheme to best fit the set of focal mechanisms. The forward problem is given by

$$Gm = d \quad (3-1)$$

The vector m is the model vector of stress tensor components:

$$m = \begin{pmatrix} \sigma_{11} \\ \sigma_{12} \\ \sigma_{13} \\ \sigma_{22} \\ \sigma_{23} \end{pmatrix} \quad (3-2)$$

there are five model parameters, and $\sigma_{33} = -(\sigma_{11} + \sigma_{22})$ is assumed, because fault slip direction cannot constrain the isotropic part of the stress tensor. The vector d is the data vector made up of $3 * K$ unit slip vector components for K focal mechanisms,

$$d = \begin{pmatrix} s_{11} \\ s_{12} \\ s_{13} \\ \dots \\ s_{K1} \\ s_{K2} \\ s_{K3} \end{pmatrix} \quad (3-3)$$

where s_{kl} is the l th component of the unit slip vector for the k th earthquake. The data kernel matrix G is derived from fault normal vector of each focal mechanism.

$$G = \begin{pmatrix} n_{11} - n_{11}^3 + n_{11}n_{13}^2 & n_{12} - 2n_{12}n_{11}^2 & n_{13} - 2n_{13}n_{11}^2 & n_{11}n_{13}^2 - n_{11}n_{12}^2 & -2n_{11}n_{12}n_{13} \\ n_{12}n_{13}^2 - n_{12}n_{11}^2 & n_{11} - 2n_{12}^2n_{11} & -2n_{11}n_{12}n_{13} & n_{12} - n_{12}^3 + n_{12}n_{13}^2 & n_{13} - 2n_{13}n_{12}^2 \\ n_{13}^3 - n_{13}n_{11}^2 - n_{13} & -2n_{11}n_{12}n_{13} & n_{11} - 2n_{13}^2n_{11} & n_{13}^3 - n_{13}n_{12}^2 - n_{13} & n_{12} - 2n_{12}n_{13}^2 \\ \dots & \dots & \dots & \dots & \dots \\ n_{K1} - n_{K1}^3 + n_{K1}n_{K3}^2 & n_{K2} - 2n_{K2}n_{K1}^2 & n_{K3} - 2n_{K3}n_{K1}^2 & n_{K1}n_{K3}^2 - n_{K1}n_{K2}^2 & -2n_{K1}n_{K2}n_{K3} \\ n_{K2}n_{K3}^2 - n_{K2}n_{K1}^2 & n_{K1} - 2n_{K2}^2n_{K1} & -2n_{K1}n_{K2}n_{K3} & n_{K2} - n_{K2}^3 + n_{K2}n_{K3}^2 & n_{K3} - 2n_{K3}n_{K2}^2 \\ n_{K3}^3 - n_{K3}n_{K1}^2 - n_{K3} & -2n_{K1}n_{K2}n_{K3} & n_{K1} - 2n_{K3}^2n_{K1} & n_{K3}^3 - n_{K3}n_{K2}^2 - n_{K3} & n_{K2} - 2n_{K2}n_{K3}^2 \end{pmatrix} \quad (3-4)$$

Where n_{ki} is i th component of the normal vector for the k th earthquake. The least squares inverse solution [e.g., *Menke*, 1989] is given by

$$G^T G m = G^T d \quad (3-5)$$

and is solved by *Michael* [1984] using Gaussian elimination. Uncertainty is estimated by bootstrap resampling of the data, which may include randomly selecting one of the

two focal mechanism nodal planes if the actual fault plane is not known or is uncertain [Michael, 1987a].

The software contains a damping factor between data misfit and model length; in my study, I did not employ the damping factor, instead I used a moving window inversion to reduce spatial variability. The two methods can achieve the similar goal to remove unnecessary variability while retaining the true variability required by data [Hardebeck and Michael, 2006].

A common way of displaying tectonic stress results is to map the azimuth of maximum horizontal compressive stress σ_{Hmax} ; to get the true orientation of the maximum horizontal stress, the software package projects the principal stresses onto a true geographic coordinate system, and calculates the normal stress acting on the vertical plane of the new coordinate system, then finds the direction of maximum/minimum normal stress [Lund and Townend, 2007].

Data and results

I have 4,169 focal mechanism solutions in Oklahoma and southern Kansas without preference of the two nodal planes. Using a 0.2° by 0.2° grid and moving step 0.1° , I generate 192 grid points with 20 or more events. Each grid point is inverted for a stress solution. The inversion results are shown by the orientation of σ_{Hmax} in Figure 3-3. The dominant orientation of σ_{Hmax} is $80^\circ \sim 85^\circ$, and the dominant faulting type is strike-slip faulting which are consistent with previous studies [Holland, 2015; Walsh and Zoback, 2016; Qi, 2016]. However, the orientation of stress field is not uniform; some spatial variations can be observed. A $\sim 10^\circ$ clockwise rotation is observed near the Nemaha

fault which might be caused by Nemaha Uplift; the azimuth rotation has been observed but not confirmed in previous study [Walsh and Zoback, 2016]. It could be an artifact because the Nemaha fault is currently not active, so we don't have enough data along this area (Figure 3-13). Or the regional stress field is changed because of geology; with the estimation of spatial extension of Nemaha Uplift and topography result in Oklahoma [Chen, 2016], we will model the regional stress state change to explain the observation. The map also shows a spatial variation of faulting type. Central Oklahoma is mostly in strike-slip faulting regime; north and northwest Oklahoma shows a transition from normal faulting to strike-slip faulting regime. The σ_{Hmax} orientation map is used to analyze the fault nature in the next section.

3.3 Optimal orientation of focal mechanisms and fault

After obtaining the regional principal stress orientations, I use Mohr circle to select the optimal focal plane, determine the optimal fault orientation and model the fault stress state.

Mohr circle: The shear and normal stress acting on the fault plane can be calculated from the two-dimensional principal stress as

$$\tau = \frac{\sigma_1 - \sigma_3}{2} \sin 2\theta \quad (3-6)$$

$$\sigma_n = \frac{\sigma_1 + \sigma_3}{2} - \frac{\sigma_1 - \sigma_3}{2} \cos 2\theta \quad (3-7)$$

Where σ_1 is maximum principal stress, σ_3 is minimum principal stress and θ is the angle between the normal vector of fault plane and σ_1 direction. The shear and normal

stress state can be represented by Mohr diagram in $\tau - \sigma_n$ plane. For the fault strength, I use fault strength envelope to represent Mohr-Coulomb friction law:

$$\tau = S + \mu\sigma_n \quad (3-8)$$

When Mohr circle is tangential to fault strength envelope, the fault starts to fail.

Optimal focal plane

Before the knowledge of regional stress field, I have no preference of the two nodal planes for focal mechanism solutions. With the known orientation of σ_{Hmax} , I can choose the real fault plane from the two nodal planes using the criteria that the angle between the strike of focal mechanism and σ_{Hmax} should be closer to 30° . Figure 3-4 shows the rose diagrams of strike, histograms of dip and rake angles of randomly listed nodal planes from OGS catalog and the same for selected primary focal plane by comparing to regional stress field. The rose diagram of selected focal planes in Figure 3-5 shows a conjugate fault pattern relative to the average σ_{Hmax} orientation of 85° ; the dip angle of most faults is larger than 50° ; the rake angle shows a dominant strike-slip faulting and a significant fraction of normal faulting which are consistent with the stress inversion results shown in Figure 3-3.

Optimally oriented faults based on σ_{Hmax} orientation

To determine whether the seismogenic faults are optimally oriented, a simple way is to compare fault strike orientation to σ_1 orientation. Because most areas in Oklahoma are in strike-slip faulting regime; the maximum horizontal compressive stress σ_{Hmax} is the largest principal stress σ_1 , so I will compare fault strike to σ_{Hmax} orientation in the following analysis; the angle difference is denoted as angle δ . For most rocks, the

friction coefficient μ ranges from 0.6 to 0.85 based on laboratory tests [Byerlee, 1978]; the range is expended to [0.2 0.85] based other observations [Reches, 1992; Qi, 2016]. As shown in Figure 3-5, the slope of fault strength envelope is [0.2 0.85], and θ range where the Mohr circle is tangential to the fault strength envelope will be [51°, 65°]; then the angle δ between fault plane and σ_{Hmax} is in [25°, 39°]. When the angle difference between the fault strike and σ_{Hmax} orientation falls in the δ range [25°, 39°], the seismogenic fault is regarded as optimally oriented. I choose 77 seismogenic faults in strike-slip faulting area and study their orientation below.

I use a uniform σ_{Hmax} orientation of 85° as comparison to our inversion results. For a uniform σ_{Hmax} orientation map, the angle δ is the difference between fault strike and 85°; for our results, the angle δ is the difference between fault strike and the orientation of nearest σ_{Hmax} from inversion map. The distribution of δ is shown in Figure 3-6; with uniform stress field, the δ of 25% seismogenic faults falls in the range 25°~39°; after considering the heterogeneity of σ_{Hmax} , one third of the seismogenic faults are optimally oriented and the δ angle falls in the expected range. Figure 3-7 shows the fault orientation state color coded by δ for a uniform σ_{Hmax} orientation and our inversion results. The faults with δ angle in the theoretical range [25°, 39°] are regarded as optimally oriented; the faults with δ angle 15° offset the theoretical range are regarded as moderately oriented; out of the above ranges, the faults are sub-optimally oriented. Several faults in central, northern and northwestern Oklahoma have been changed from sub-optimally oriented or moderately optimally oriented to optimally oriented.

3.4 Fault stress state based on Mohr circle analysis

Using the criteria above helps identify seismogenic faults that are optimally oriented to current stress field; however, when pore pressure increases (Figure 3-1), some moderately optimally oriented faults can be brought to failure. We model the fault stress state to study the failure potential using parameters (Table 3-1) from *Goertz-Allmann and Wiemer* [2012], which are based on Basel geothermal system study [*Häring et al.*, 2008]. I use following equations to calculate normal and shear stress on fault plane:

$$t(\vec{n}) = T \cdot \vec{n} \quad (3-9)$$

$$\sigma_n = t(\vec{n}) \cdot \vec{n} \quad (3-10)$$

$$\tau_s = t(\vec{n}) \cdot \vec{f} \quad (3-11)$$

where T is the stress tensor; we use 2D stress tensor of principal stress σ_1, σ_3 ; $t(\vec{n})$ is the traction of a given fault plane with normal vector \vec{n} ; σ_n and τ_s are normal and shear stress based on fault normal vector (\vec{n}) and parallel vector (\vec{f}); for each fault, I have three scenarios to characterize fault orientation relative to stress field. In scenario 1, I calculate the stress state based on the orientation of normal vector of fault plane (the eigenvector of the smallest eigenvalue in Chapter2) to the orientation of σ_3 ; in scenario 2, the fault stress state is calculated based on the orientation of fault strike to a uniform σ_{Hmax} orientation of 85° ; in scenario 3, the stress state is based on the orientation of fault strike to the inversion result of σ_{Hmax} orientation. Fault stress state for four different principal stress models (Table 3-1) [*Goertz-Allmann and Wiemer*, 2012] are calculated and the results are similar; I show the result in Figure 3-8 from a model with

$\sigma_1 = 105MPa$, $\sigma_3 = 42MPa$ and pore pressure (P_h) 25MPa (Table 3-1, Model 2). Each circle in the figure represents the stress state of a seismogenic fault. The friction coefficient is assumed as 0.6. The faults in optimal angle range (between two dashed lines) are closest to fault strength envelope and will fail first. With pore pressure increase of 10MPa, moderately optimally oriented faults and sub-optimally oriented faults start to fail. Before pore pressure increase, only one third of the seismogenic faults are optimally oriented and close to fail; after pore pressure increase, over 70% of the seismogenic faults are distributed above the fault strength line and possible to fail. The results show slight difference between the scenarios. Scenario 1 that stress state is determined by fault normal and σ_3 orientation has the largest percentile (80%) of faults that are above the fault strength line and ready to fail; with a uniform σ_{Hmax} and local inverted σ_{Hmax} orientation, scenario 2 and 3 have 69% and 72% of the faults that are likely to fail, respectively. A better knowledge of the regional stress orientation has improved our understanding of the fault activities.

3.5 Discussion

I map seismogenic faults from seismicity spatial distribution and invert stress field from focal mechanism solutions. The input data for fault mapping and stress field inversion are two different datasets, which are independent of each other. However, in reality, the focal mechanism solution is correlated with the fault orientation. And one concern is that large clusters tend to dominate the focal mechanism catalog, and thus the focal mechanism solutions in these clusters might become dominant in stress inversion and bias the result. The length of the M5 clusters is close to the grid size of 0.2° by 0.2° in

stress inversion. But this is not the case for small clusters, as the grid size is much larger than the small cluster size (mapped fault length based on seismicity distribution is $10^0 \sim 10^{0.6}$ km in Figure 2-10). Therefore, the input data from most grids would include focal mechanism solutions from one or more small clusters and some background seismicity. For the seismogenic faults that are shifted from moderately optimally oriented or sub-optimally oriented to optimally oriented in central and northern Oklahoma, the input file for those grids contains focal mechanisms from both clusters and background seismicity. For large clusters in Pawnee, Prague, Fairview and Woodward, most of the input data are from clusters and those large clusters are relatively isolated from background seismicity, so the inversion result should favor the focal solutions within clusters. I still find the inversion results comparable to previous studies and they can reveal more detailed information about the cluster.

For Pawnee cluster, previous study [Alt and Zoback, 2016] shows a fault segment with strike 110° and σ_{Hmax} orientation is 82° ; we pick the fault segment with strike 105° and the stress orientation is 80° shown in Figure 3-9 with all input focal mechanism solutions. The fault strike is consistent with strike of M5.8 mainshock focal mechanism solution. The stress orientation will be slightly changed to 77° when we only use the focal mechanisms from aftershocks. This could be an artifact because of smaller dataset before mainshocks; alternatively, this could suggest temporal changes caused by the mainshock, which has been observed elsewhere from large earthquakes [Hardebeck and Hauksson, 2001], and this would require more detailed analysis.

For Prague cluster shown in Figure 3-10, we mapped the fault strike 55° and stress orientation 79° from 62 focal mechanism solutions from the cluster. The dominant strike angle of these focal mechanisms is $50\sim 60^\circ$ and the strike of the M5.7 mainshock focal mechanism solution is 56° , which verify the fault strike. The δ angle between fault strike and σ_{Hmax} orientation is 24° , which might reflect a higher friction coefficient in this area. Some grid shows a slight σ_{Hmax} rotation when the input only includes focal mechanisms from northeastern part of the fault, which is consistent with the observation that the northeastern and southwestern parts of the fault are not at the exact same trend and there is strong heterogeneity in the focal mechanism solutions [Keranen *et al.*, 2013; Sumy *et al.*, 2014].

For Fairview cluster shown in Figure 3-11, the fault strike and dip inferred from seismicity are 45° and 86° , respectively; the fault strike is consistent with focal solution of the Mw5.1 mainshock (strike 47°) and five other $M>4.0$ events (strike $42^\circ\sim 48^\circ$) in this cluster and also consistent with $40^\circ\sim 48^\circ$ strike range from Yeck *et al.* [2016], but our result shows a slightly more steeply dipping plane compared to $70^\circ\sim 80^\circ$ (Yeck *et al.*, 2016). The local orientation of σ_{Hmax} is 88.6° in strike-slip faulting regime, which is comparable to N83°E from Alt and Zoback [2015]. In our study, the main Fairview fault is not optimally oriented base on the strict theoretical δ range [25° , 39°]; the fault is not optimally oriented either based on a 30° criteria between fault strike and σ_{Hmax} in Alt and Zoback [2016]. However, a group of smaller events shows strike distribution around 30° of the stress orientation; those smaller fractures in this cluster are optimally oriented to the stress field. The reactivation of this moderately optimal fault might

suggest regional stress changes from some ambient stress state; and the fault rupture might be initiated by a high pore pressure increase due the high-injection rate zone to the northeast [Yeck *et al.*, 2016]. Fairview cluster delineates an extension of a north-east-trending fault. If the currently active segment is connected to the southwestern part of the mapped fault, larger earthquakes might occur in this area.

Woodward cluster is an isolated cluster in northwest, which demonstrates a transition zone from normal faulting to oblique faulting (normal and strike-slip) to strike-slip faulting. The faulting type transition from normal to strike-slip faulting has been observed by Alt and Zoback [2015] in northern Oklahoma. In strike-slip faulting regime, we have $\sigma_{Hmax} > \sigma_V > \sigma_{Hmin}$; northern and northwest Oklahoma shows a transition from normal faulting ($\sigma_V > \sigma_{Hmax} > \sigma_{Hmin}$) to a combination of strike-slip and normal faulting ($\sigma_{Hmax} \cong \sigma_V > \sigma_{Hmin}$). Thus, the stress magnitudes are less compressive in northern Oklahoma than in the central Oklahoma.

The uncertainties of stress field can be calculated from the inversion results using bootstrap resampling. Figure 3-12 shows the histogram of standard deviation of σ_{Hmax} orientation from 2000 resamplings for all the grids. More than 85% of the grids have a standard deviation less than 5° . Figure 3-13 shows the inversion results with uncertainties; the grids with standard deviation larger than 5° are mainly distributed in normal or strike-slip/normal faulting area or some strike-slip faulting area with a small number of focal mechanism solutions available (black dots in Figure 3-13). Since we only analyze the optimal fault orientation in strike-slip faulting area, the uncertainty of the stress orientation in our analysis should be less than 10° with most grids less than 5° .

3.6 Conclusion

I generate a detailed stress map (0.2° by 0.2°) of Oklahoma and south Kansas using over 4,000 focal mechanisms. The basic observations that the dominant orientation of σ_{Hmax} is $80^\circ \sim 85^\circ$ and dominant faulting type is strike-slip faulting are consistent with previous studies. The map also shows spatial variations of stress orientation and faulting type in north and northwest Oklahoma. The uncertainty of stress orientation of these areas is larger than 5° but less than 10° . I use δ range $[25^\circ, 39^\circ]$ (angle between fault plane and σ_{Hmax}) to search for optimally oriented seismogenic faults in Oklahoma. Using a uniform stress orientation 85° , some currently active faults are not optimally oriented; if I compare the fault strike to our heterogeneous stress map, those faults are optimally oriented. The stress field in Oklahoma is not uniform and some detailed spatial variations ($\geq 0.2^\circ$) are revealed by my inversion results. A detailed stress map can be used to better estimate the fault stress state and explain the fault activities.

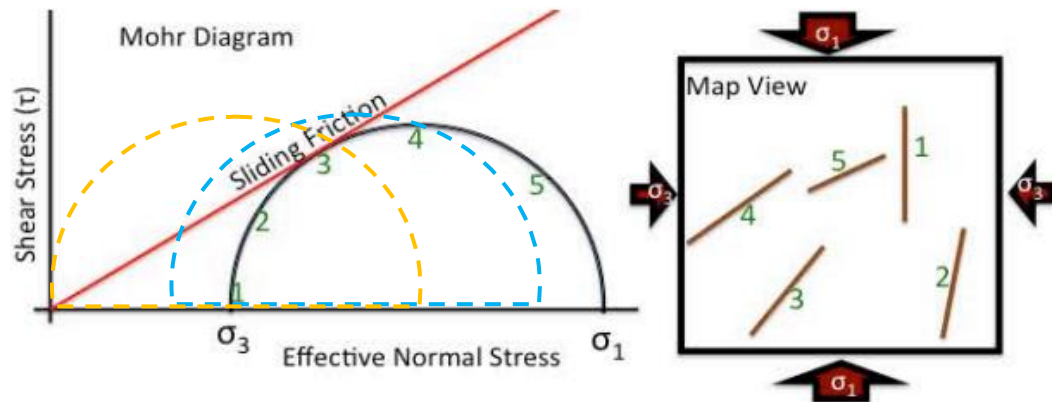


Figure 3-1. 2D Mohr diagram showing 5 hypothetical faults in a 2D Mohr circle (left) numbered to correspond to their orientations on the map (right). Fault number 3 is closest to slip (black Mohr circle) in this stress field because the ratio of shear to effective normal stress is highest. Fault 2 and 4 could be triggered by modest changes in pore pressure (blue Mohr circle), and fault 1 and 5 would require the most pore pressure to slip (orange Mohr circle). [Walsh and Zoback, 2016]

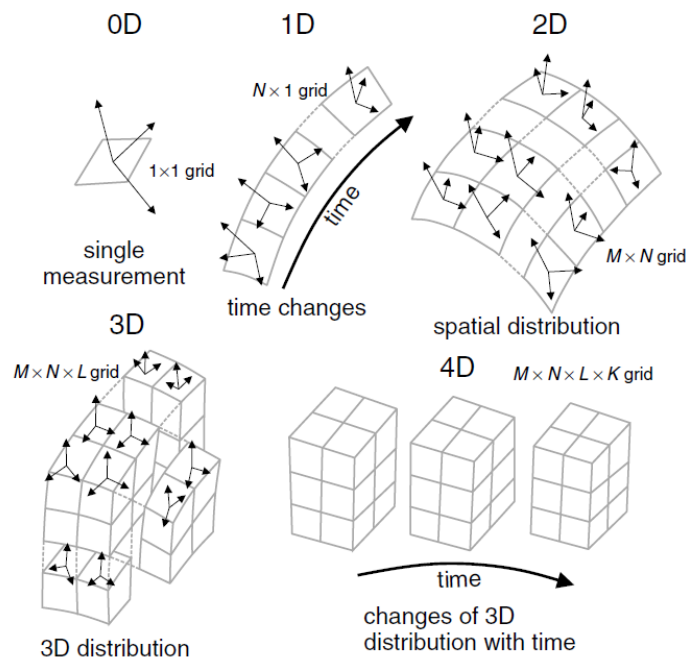


Figure 3-2. Illustration of possible dimensions of the formal stress inversions performed with MSATSI stress inversion package from *Martínez-Garzón et al.* [2014].

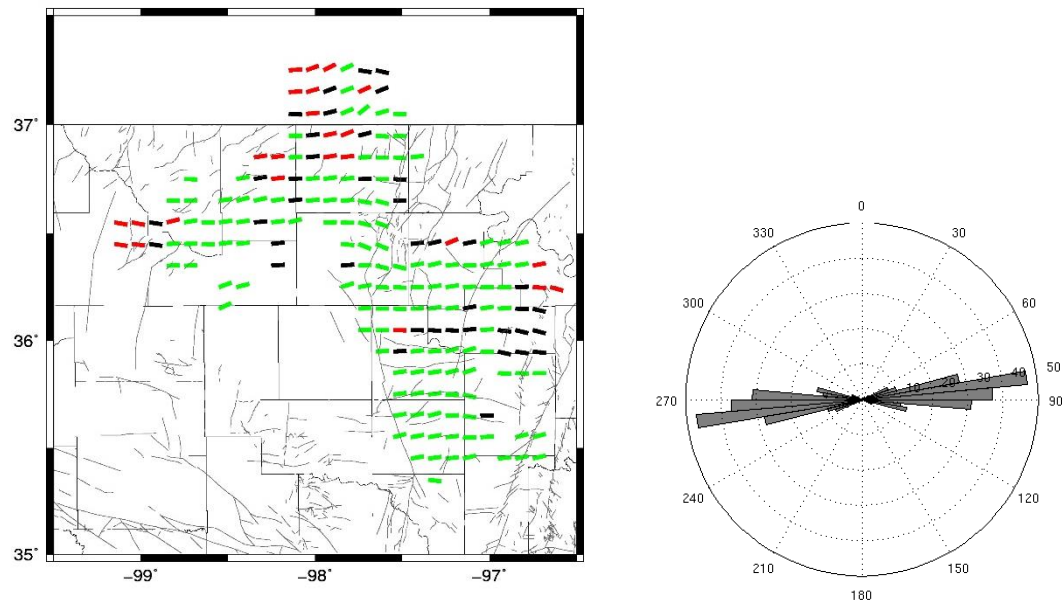
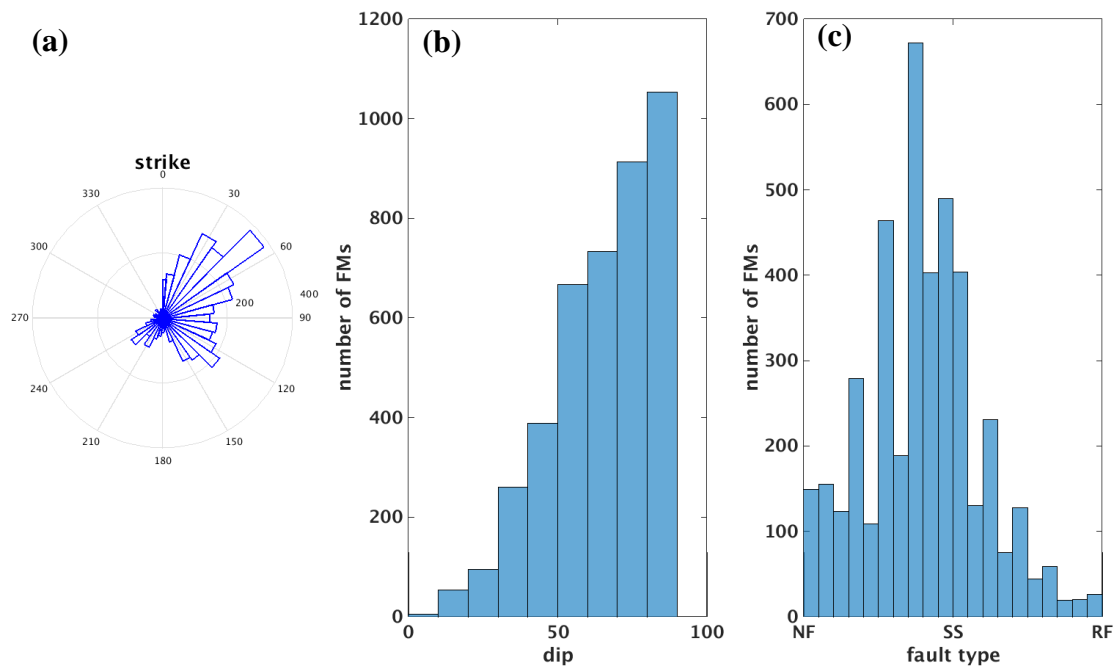


Figure 3-3. Maximum horizontal stress orientation map (left) (red: normal faulting; green: strike-slip; black: oblique faulting) and histogram σ_{Hmax} orientation(right).



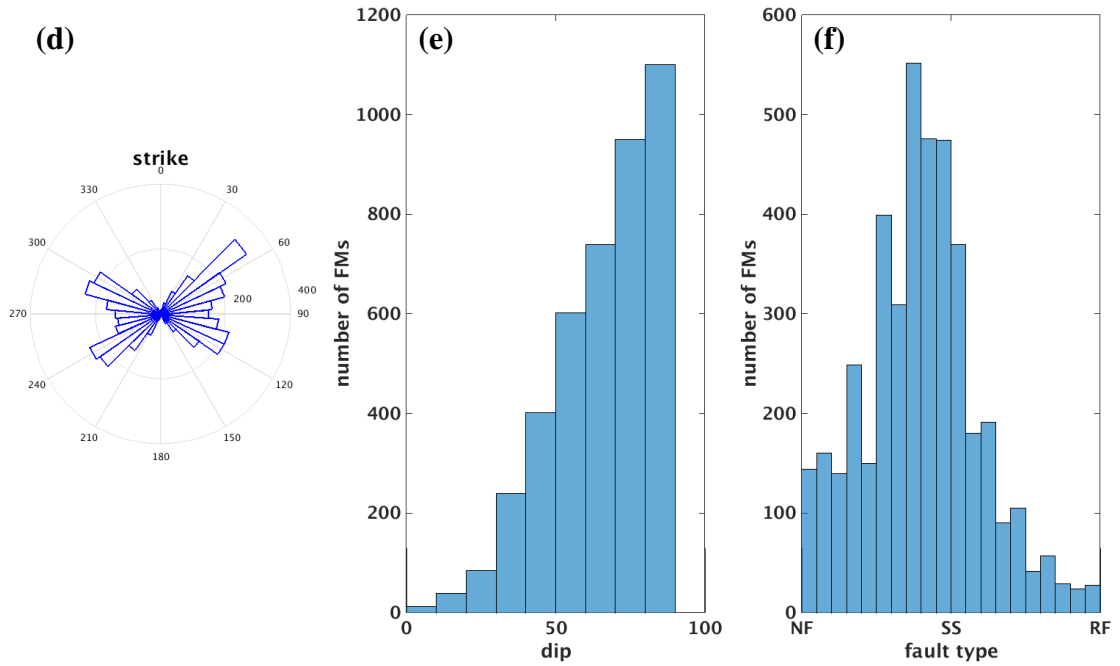


Figure 3-4. Top: rose diagram of strike(a), histogram of dip(b) and rake angle (c) of original focal plane from OGS catalog. Bottom: rose diagram of strike(d), histogram of dip(e) and rake angle (f) of selected optimal focal plane based on stress orientation. NF: normal faulting; SS: strike slip faulting, RF: reverse faulting in (c) and (f).

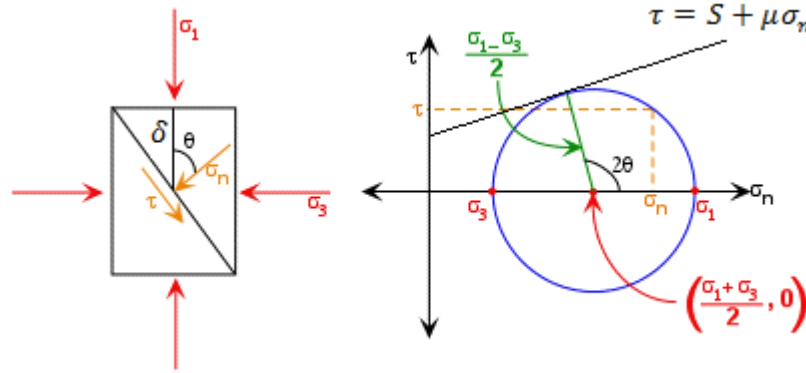


Figure 3-5. Fault plane orientation relative to a given $\sigma_1 - \sigma_3$ stress field (left); θ is the angle between the normal of fault plane and σ_1 orientation; Mohr diagram of shear stress versus effective normal stress (right).

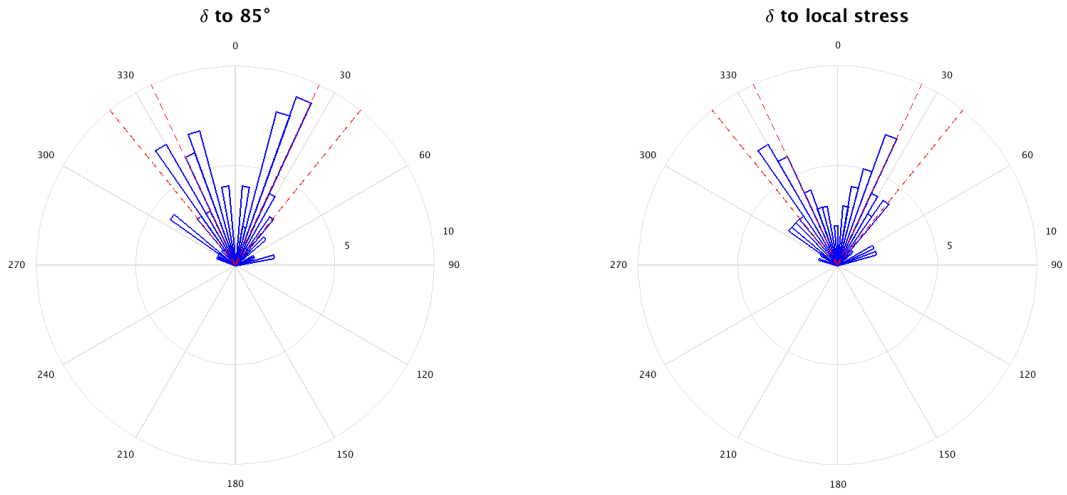
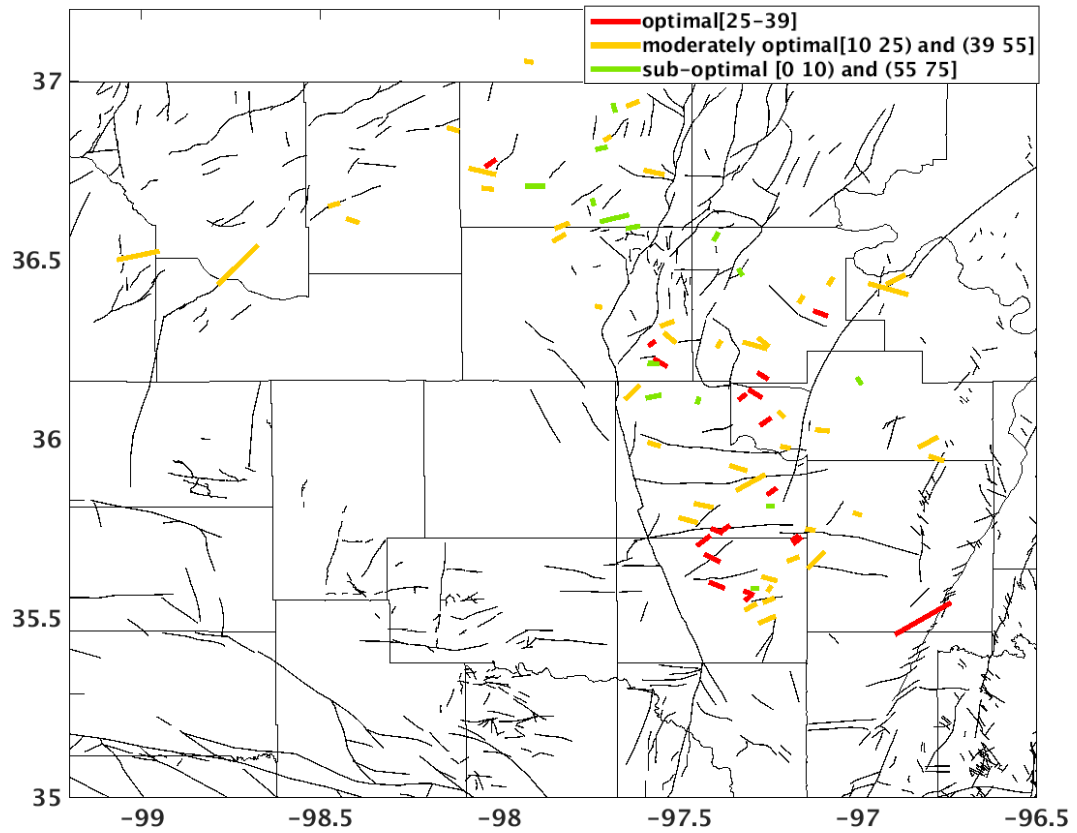


Figure 3-6. Left: rose diagram of δ between fault strike and uniform σ_{Hmax} orientation 85° . Right: rose diagram of δ between fault strike and nearest σ_{Hmax} orientation from our inversion results. Dashed red lines denote the optimal range $[25^\circ, 39^\circ]$.



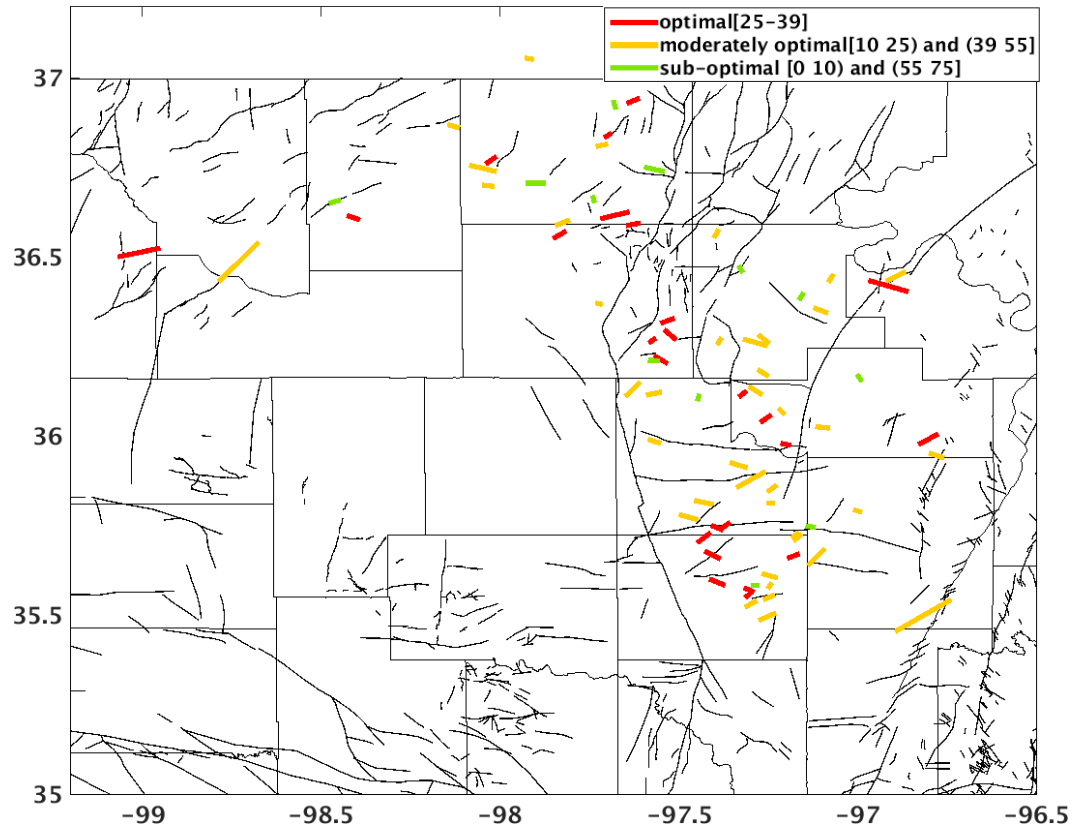


Figure 3-7. Seismogenic fault map color-coded by δ , the angle between fault strike and σ_{Hmax} orientation. Top: δ is calculated using uniform σ_{Hmax} orientation 85° . Bottom: δ is calculated using nearest σ_{Hmax} orientation from our inversion result.

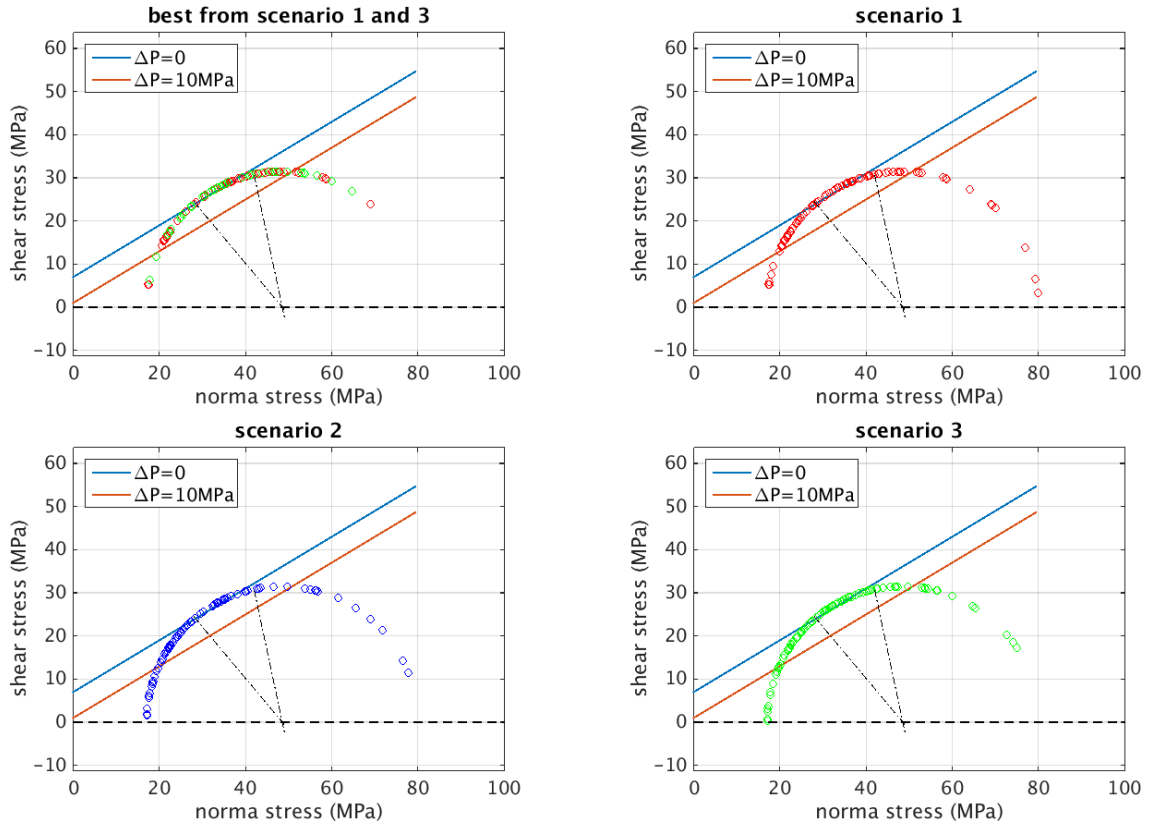


Figure 3-8. Fault stress state calculated from Model 2. Scenario 1,2 and 3 are three different ways to determine fault orientation to stress field (see the text). Blue and red lines are the fault strength envelopes with $\mu = 0.6$, $\Delta P = 0$ and $\mu = 0.6$, $\Delta P = 10 \text{ MPa}$, respectively. Each circle represents a seismogenic fault stress state; red: fault stress state from scenario1; blue: fault stress state from scenario 2; green: fault stress state from scenario 3. Two dashed lines denote the optimal orientation angle range with $2\theta \in [102^\circ, 130^\circ]$.

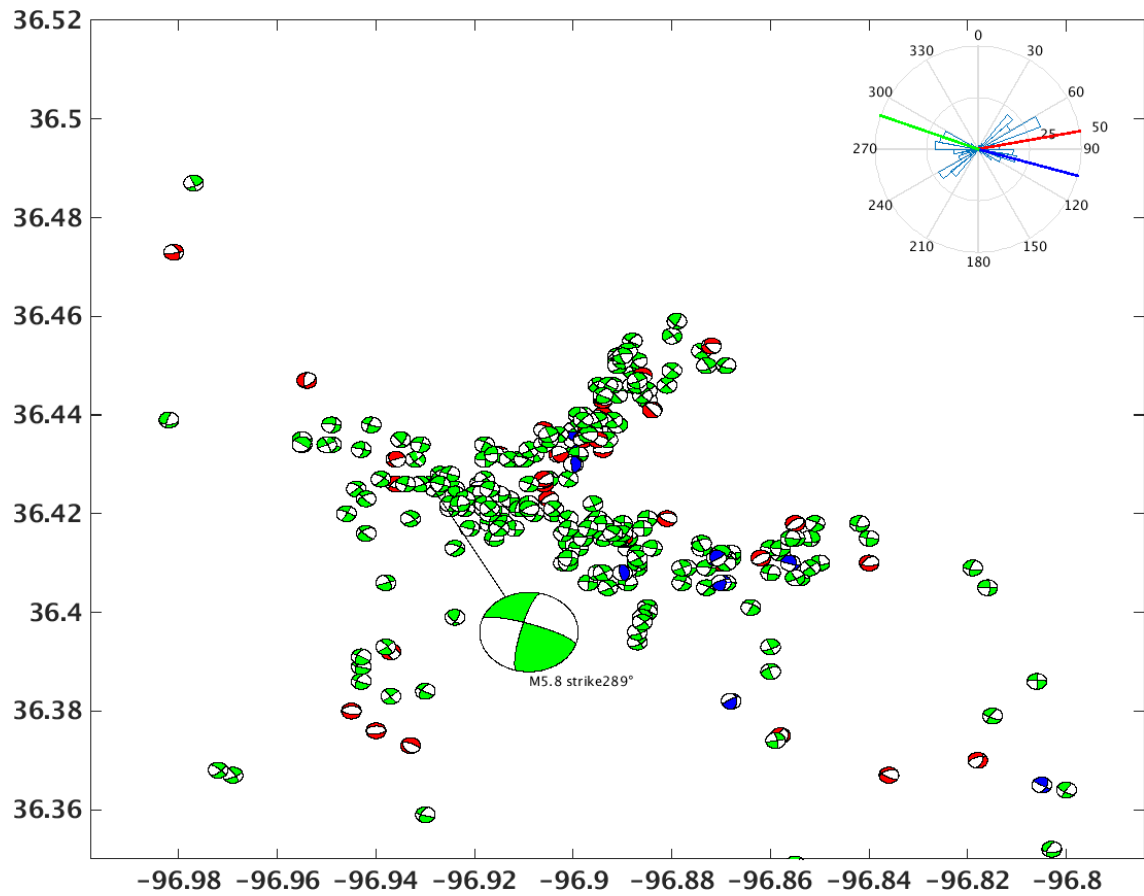


Figure 3-9. Focal mechanism distribution for Pawnee cluster. Color scheme for the beach ball: green, strike-slip faulting; red, normal faulting; blue, reverse faulting. A rose diagram of the strike of selected focal planes is shown in the right corner. Red line is the inverted σ_{Hmax} orientation; green line is the strike of M5.8 mainshock in Pawnee cluster; blue line is the seismogenic fault strike orientation; the blue are green lines are consistent.

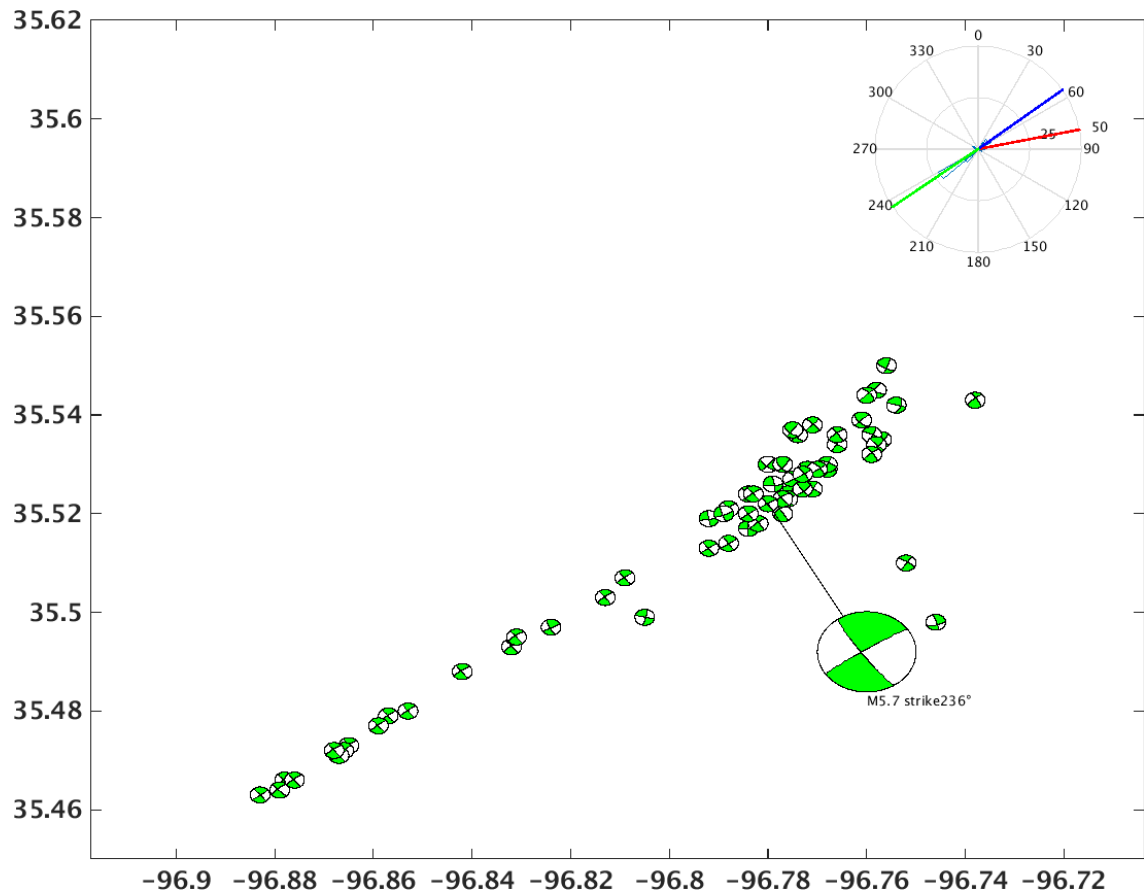


Figure 3-10. Focal mechanism distribution for Prague cluster. Color scheme for the beach ball: green, strike-slip faulting; red, normal faulting; blue, reverse faulting. A rose diagram of the strike of selected focal planes is shown in the right corner. Red line is the inverted σ_{Hmax} orientation; green line is the strike of M5.7 mainshock in Prague cluster; blue line is the seismogenic fault strike orientation; the blue are green lines are consistent.

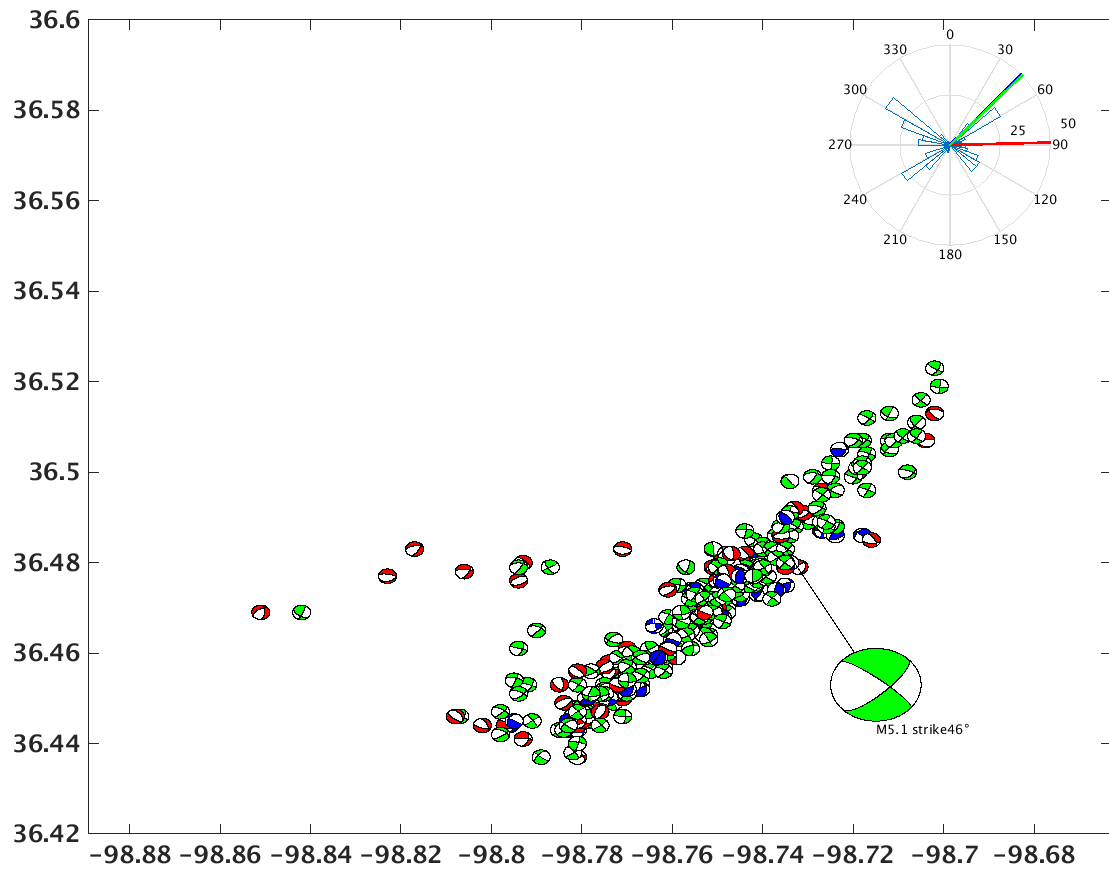


Figure 3-11. Focal mechanism distribution for Fairview cluster. Color scheme for the beach ball: green, strike-slip faulting; red, normal faulting; blue, reverse faulting. A rose diagram of the strike of selected focal planes is shown in the right corner. Red line is the inverted σ_{Hmax} orientation; green line is the strike of M5.1 mainshock in Fairview cluster; blue line is the seismogenic fault strike orientation; the blue are green lines are overlaid.

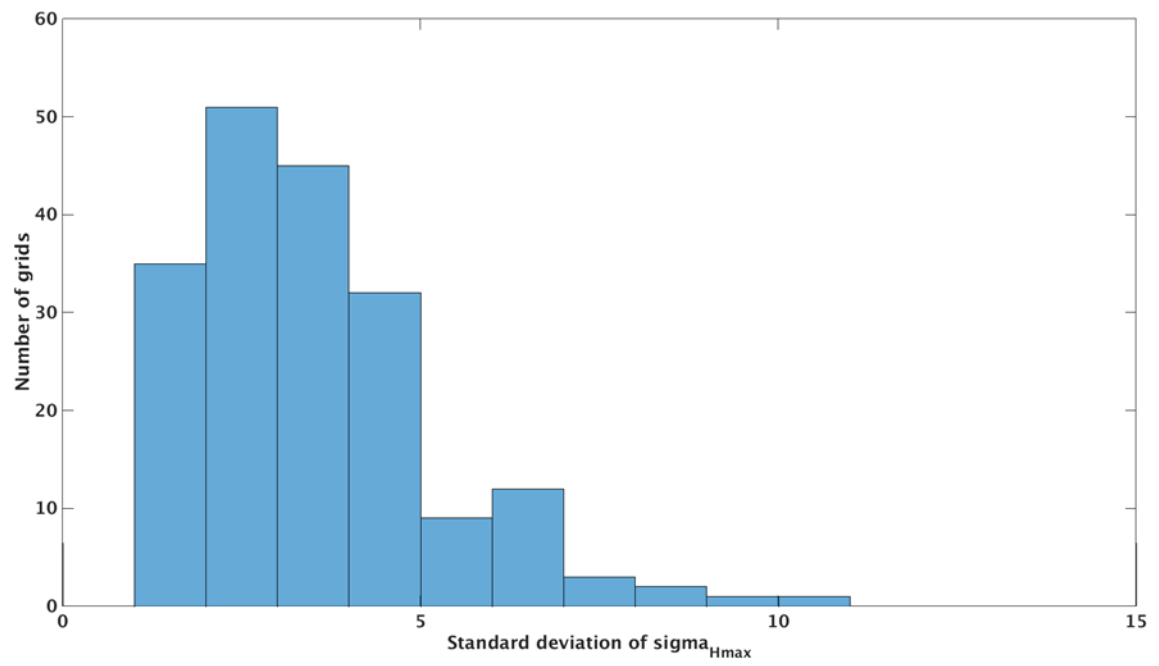


Figure 3-12. Histogram of standard deviation of σ_{Hmax} orientation.

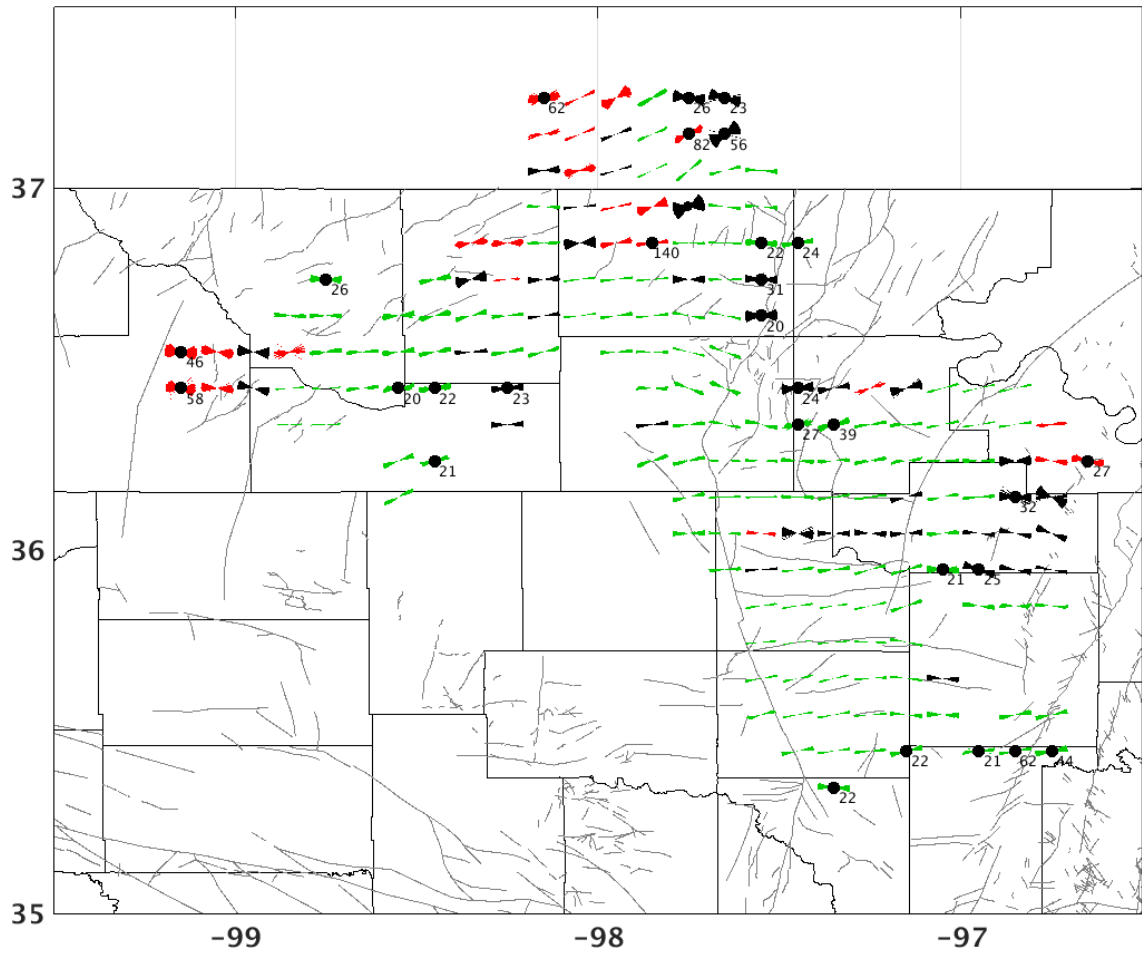


Figure 3-13. Maximum horizontal compressive stress orientation map with uncertainties from bootstrap resampling (red: normal faulting; green: strike-slip faulting; black: oblique faulting). Gray lines are mapped fault [Holland, 2015]. Black dots show grids with standard deviation of σ_{Hmax} larger than 5° . The numbers under the black dots are the number of focal mechanism solutions available in that grid.

Table 3-1: Fault stress state modeling parameters. [*Goertz-Allmann and Wiemer, 2012*]

Model #	1	2	3	4
Model	Avg. crust	Avg. crust	Weak crust	Strong crust
depth	4.5km	2.5km	4.5km	4.5km
$\bar{\sigma}_3(MPa)$	75	42	75	75
$\bar{\sigma}_1(MPa)$	185	105	147	232
$P_h(MPa)$	45	25	45	45

Chapter 4 A case study: Woodward cluster

4.1 Introduction

Several large clusters including the M_w 5.7 Prague, M_w 5.1 Fairview and M_w 5.8 Pawnee earthquakes have been studied in Oklahoma [Keranen *et al.*, 2013; Keranen *et al.*, 2014; Yeck *et al.*, 2016]. Woodward cluster differs from other large clusters in Oklahoma. First, the clustering results show that it is composed of several small subclusters, rather than one large cluster like Fairview; second, there are no events with magnitude larger than 4.0 but the moment release is not smooth; third, it is in a transtensional regime characterized by both normal and strike-slip faults. This chapter will focus on Woodward cluster and analyze stress state, seismicity migration, Coulomb Stress interaction in this cluster.

4.2 Regional stress state in Woodward cluster

The focal mechanism solutions show that Woodward cluster is in a transtensional regime. From the depth view of focal mechanism solutions in Figure 4-1, I can see a dipping strike-slip fault at deeper depth and some normal slip components at shallower depth. As shown in Figure 4-2, I pick three segments of faults based on the seismicity distribution and focal mechanism distribution in this cluster. The stress inversion result shows that the local σ_{Hmax} orientation is 100° ; the main strike-slip fault strike is 68° , which is optimally oriented; the normal faulting segment in the middle is at strike of 98° , parallel to the σ_{Hmax} orientation; and the dipping angle is 68° , which is optimally oriented compared to the vertical direction of σ_1 . The optimal orientation of the faults in this cluster would facilitate the earthquake occurrence.

Woodward cluster can be used to define a strike slip fault system; in brittle upper crust, strike-slip faults tend to have complex structures in which minor faults undergo oblique slip [*Tchalenko*, 1970; *Naylor et al.*, 1986]. In cross-section view, faults tend to be steep at depth and to splay upwards, forming flower structures [Figure 4-3; *Harding*, 1985; *Sylvester*, 1988]. The conventional understanding is that flower structures form in strike-slip faulting and their fault splays have reverse or normal components of slip; positive flower structures form in transpressional regime and their fault splays show reverse components of slip and negative flower structures form in transtensional regime and their fault splays show normal components of slip [*Guerroué and Cobbold*, 2006]. The observation in Woodward is consistent with the above theory, a steeply dipping strike-slip fault at depth with normal component of slip forming in the transtensional regime.

4.3 Seismicity migration

A three-dimensional seismogenic fault system in the Woodward cluster is shown in Figure 4-4. I use seismicity to analyze the reactivation process of the fault system. In the Woodward cluster, there are no events with magnitude larger than 4.0, but there are several spikes in seismicity rate and jumps in cumulative moment release, which appear to correspond to each newly reactivated segment along the fault (Figure 4-5 and Figure 4-6). I separate the sequence into six stages in time based on seismicity rate changes:

1. Seismicity starts on the northwest normal fault segment (on fault plane 2)
2. Seismicity migrates to the northeast strike slip fault (on fault plane 3);
3. Seismicity extends to the northeast (fault plane 3);

4. Seismicity extends to farther northeast (fault plane 3);
5. Reactivation of southwest end of fault plane 3 at shallower depth;
6. Reactivation of fault plane 2 at relative shallow depth.

4.4 Coulomb Stress interaction

Coulomb Stress changes can be used to explain the rupture pattern in Woodward cluster; Coulomb failure stress (CFS) [Jaeger and Cook, 1969] is defined as

$$CFS = |\tau| + \mu(\sigma + P) - S \quad (4-1)$$

Where $|\tau|$ is the shear traction on a plane, σ is the normal traction on the plane and P is the fluid pressure, S is the cohesion, μ is the coefficient of friction. If we assume that μ and S are constant over time, a change in CFS resolved in the slip direction is:

$$\Delta CFS = \Delta\tau + \mu(\Delta\sigma_n + \Delta P) \quad (4-2)$$

$$\Delta CFS = \Delta\tau + \mu'\Delta\sigma'_n \quad (4-3)$$

where $\Delta\tau$ is shear stress change, $\Delta\sigma_n$ is normal stress change due to the earthquake; μ is the coefficient of friction, and ΔP is the change in pore pressure. ΔCFS is Coulomb Stress change resolved onto the fault plane and in the slip direction of the subsequent earthquakes; ΔCFS is used to evaluate if one earthquake brings another earthquake closer to, or farther away from failure, that is if $\Delta CFS > 0$, fault plane is loaded and brought closer to failure; if $\Delta CFS < 0$, the fault plane is relaxed, which is called ‘stress shallow’; Some studies have simplified the first equation by using an apparent coefficient of friction μ' without explicitly calculating ΔP ;

From previous studies [Reasenber and Simpson, 1992; King *et al.*, 1994; Hardebeck *et al.*, 1998], static stress changes as low as 0.01MPa (0.1bar) can trigger earthquakes.

To study the interaction between the events of the six stages, I cluster each stage with daily seismicity rate larger than 2 events and calculate a cumulative moment from all the earthquakes during each stage. As the events in each stage are close to each other in time and space, the cumulative magnitude is used to represent the cumulative effect of the cluster on subsequent stages. I use the average of the representative focal mechanisms in the cluster and the cumulative magnitude (Table. 4-1) as input to calculate the Coulomb Stress changes resolved on the seismogenic fault planes in this area in the Coulomb3.3 software [Toda *et al.*, 2005, 2011; Lin *et al.*, 2004]. The Coulomb Stress change can affect the following rupture area (Figure 4-7). When the current stage ruptures, it exerts Coulomb Stress on the fault system, and fault plane with positive Coulomb Stress is consistent with the subsequent rupture area. As shown in Figure 4-7, fault slip in stage 1 generates positive ΔCFS on the northeast strike-slip fault at depth, where the strike-slip fault ruptures in stage 2. The slip in stage 2 generates positive ΔCFS both to the northeast and on top, where the fault rupture extends to northeast in stage4 and some shallow faults are reactivated in stage5. The slip in stage 5 generates positive ΔCFS at shallow depth to the west and leads to the reactivation of shallow structures on the normal fault in stage6. Because there are more events with $M > 3.0$ in stage 1 and stage 2 as shown in Figure 4-4, the cumulative magnitude for these two stages is larger than $M4.0$; the Coulomb Stress changes in stage 1 and stage 2 have a significant influence on the rupture pattern.

4.6 Discussion

Woodward is located in a transition area from normal faulting to strike-slip faulting; the stress magnitudes are less compressive in this area. The depth distribution of seismicity and focal mechanism reveals a main deeper strike-slip fault and a shallower normal component of slip. These normal slips might be secondary structures caused by the shear slip of strike-slip fault and their penetration depth depends both on the sedimentation above and shear stress below.

We use a cumulative magnitude to study the Coulomb Stress interaction because those events occurred close to each other in time and space. We pick the average values of the focal mechanisms in each stage as cumulative rupture. However, some focal mechanisms show a large difference from the dominant one; if the difference is the true case and not due to uncertainties, this cumulative effect of stress change might be exaggerated because the stress change of individual events with different focal mechanisms might counteract each other.

4.7 Conclusion

I use Woodward cluster as a case study and show that the two currently active fault segments in this cluster are optimally oriented to regional stress field; the normal fault segment is optimally oriented to σ_v and the strike-slip segment is optimally oriented to σ_{Hmax} . The strike-slip fault at depth with normal component of slip above characterizes a transtensional regime in this area. The seismicity distribution can depict the fault rupture process; the rupture started on the normal fault segment, migrated to the main strike-slip fault and at the same time reactivated some shallower secondary fault

structures. Coulomb Stress interaction can be used to explain the sequential reactivation of different fault segments, where previous stages promoted failure of the next stage.

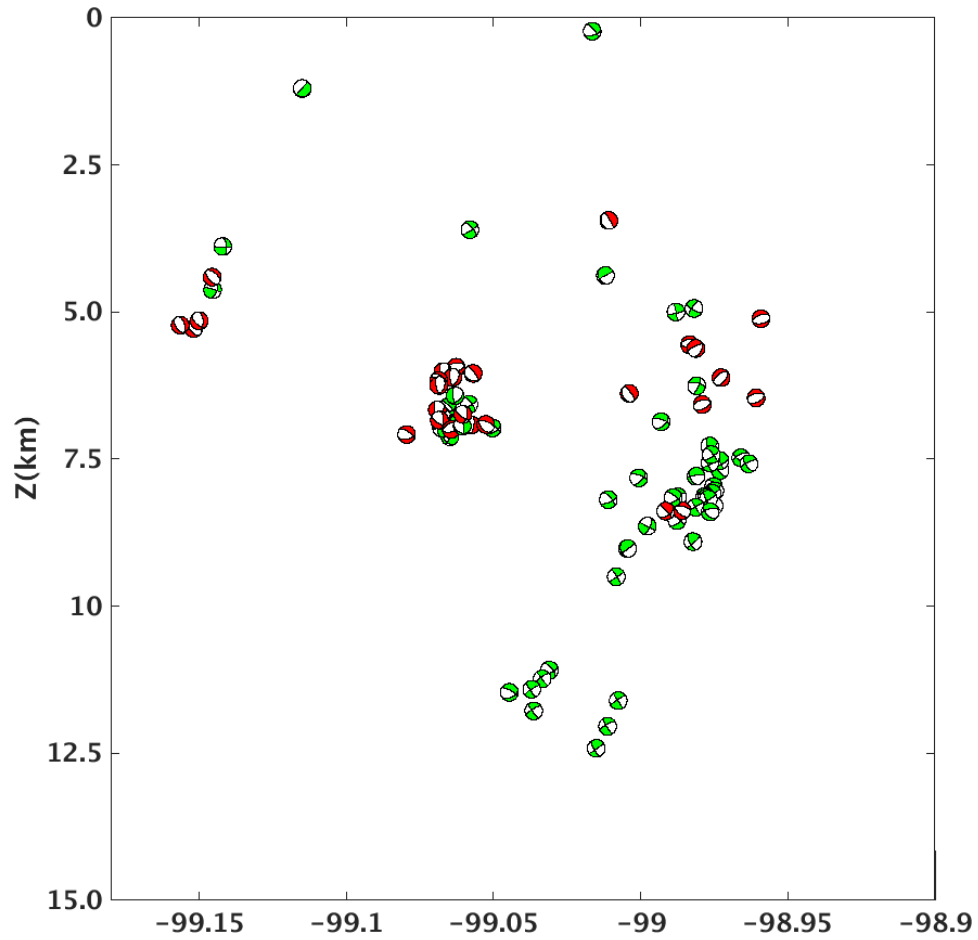


Figure 4-1. Focal mechanism distribution in depth view (green: strike-slip faulting; red: normal faulting).

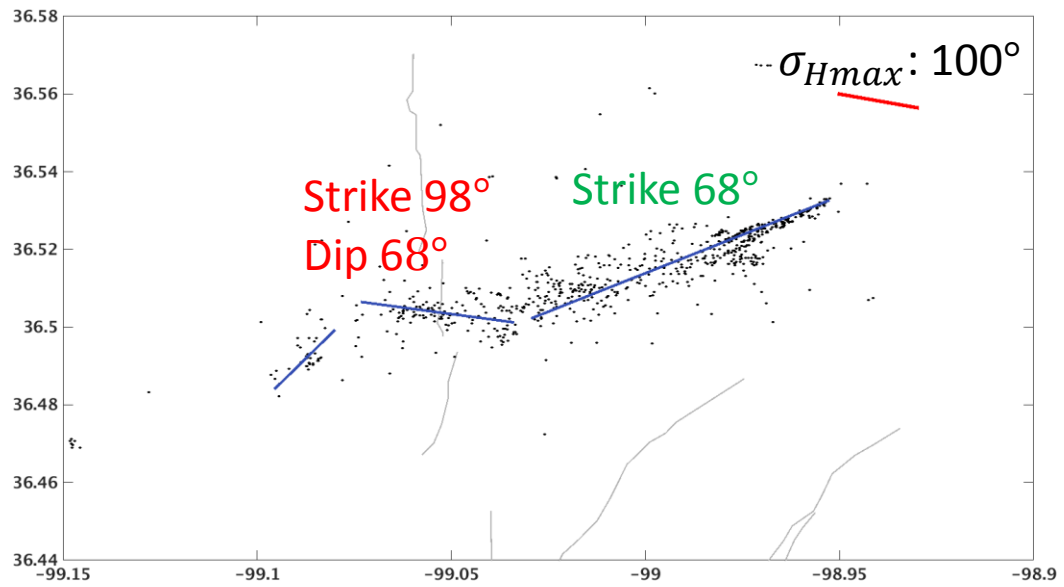


Figure 4-2. Seismogenic fault segment map in Woodward cluster (blue lines); the regional σ_{Hmax} orientation is shown at top right corner; red color means normal faulting. Black dots are seismicity in this cluster. The fault strike and dip angle are listed above the fault segments.

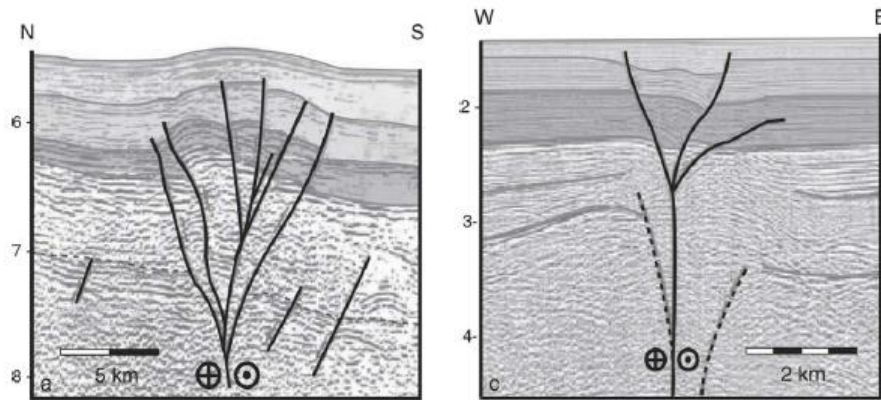


Figure 4-2. Flower structures in nature. Seismic profiles are of positive flower structures from the Aruba Gap Abyssal Plain, Colombia (left) and negative flower structure from the Andaman Sea (right). Vertical scale is in seconds of two-way travel time. [Guerroué and Cobbold, 2006]

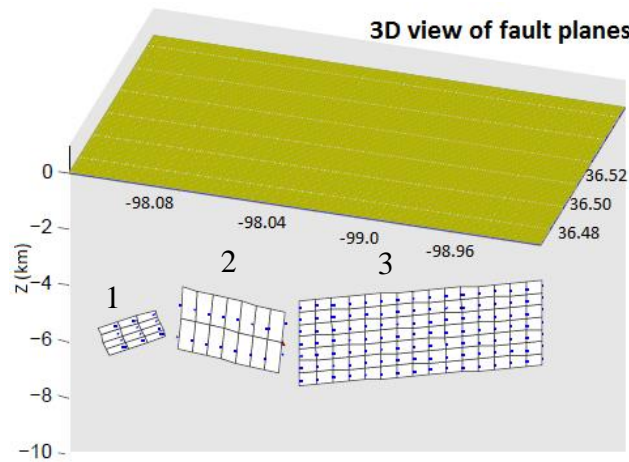


Figure 4-3. 3D view of seismogenic fault planes picked from seismicity distribution in Woodward cluster.

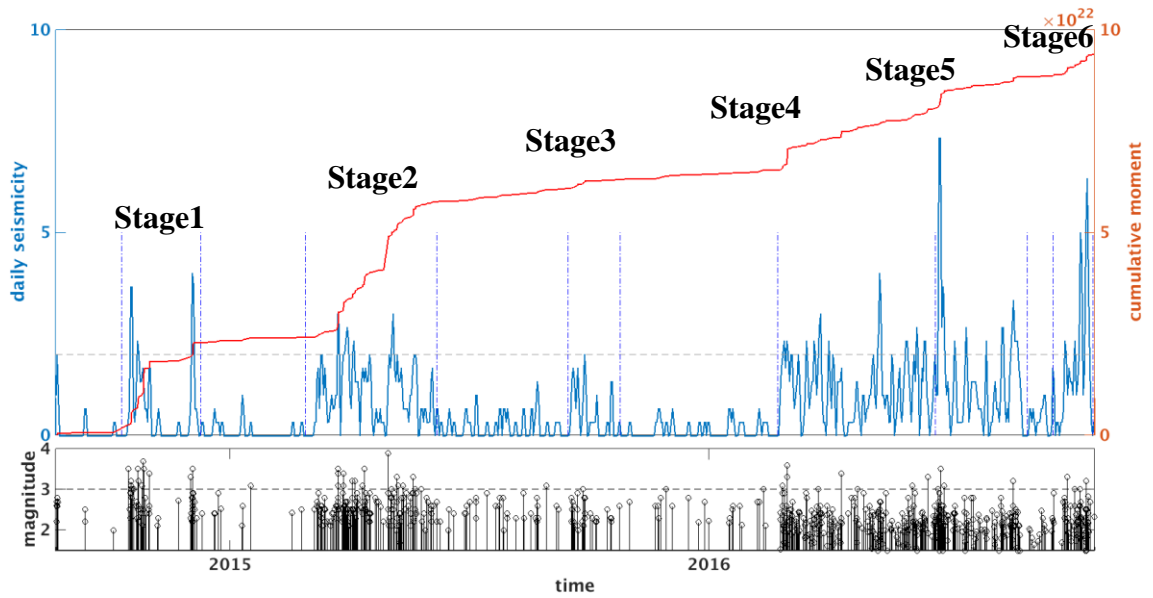


Figure 4-4. Seismicity overview for Woodward cluster. Top: daily seismicity rate (blue lines) and cumulative moment curve (red lines); stages are denoted by blue dashed lines; each stage corresponds to a jump in cumulative moment curve. Bottom: magnitude distribution. Black dashed line denotes ***M*3.0**.

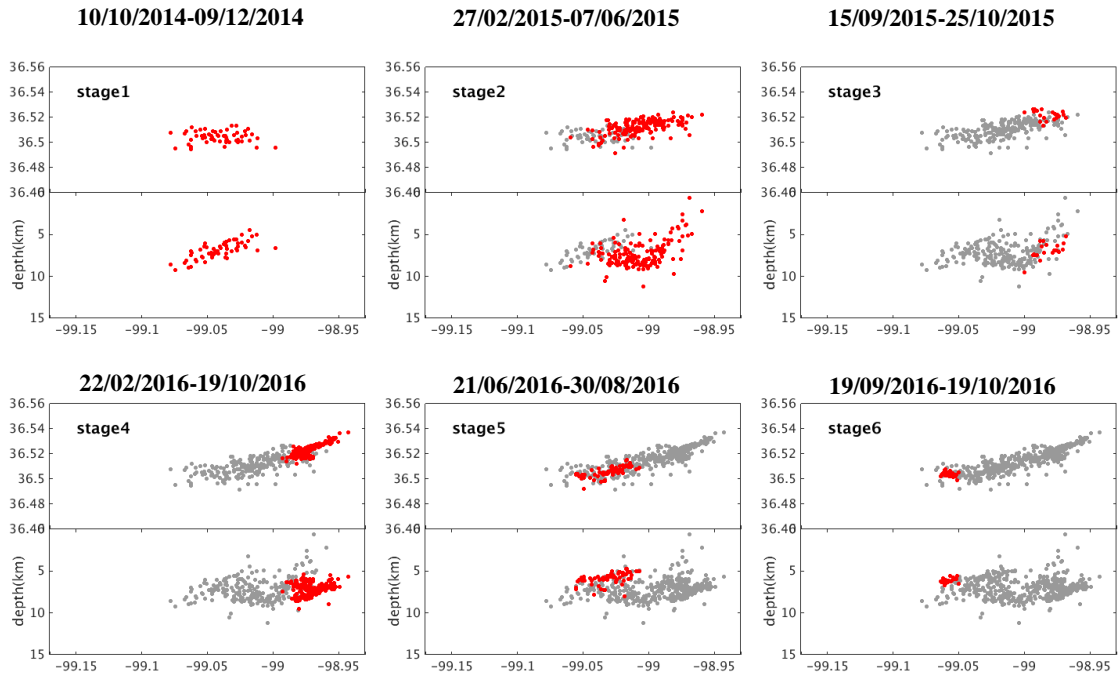


Figure 4-5. Map view (top panel) and depth view (bottom panel) of seismicity of each stage shown in Figure 4-4. Red dots are events occurring in current stage, grey dots are events in previous stages.

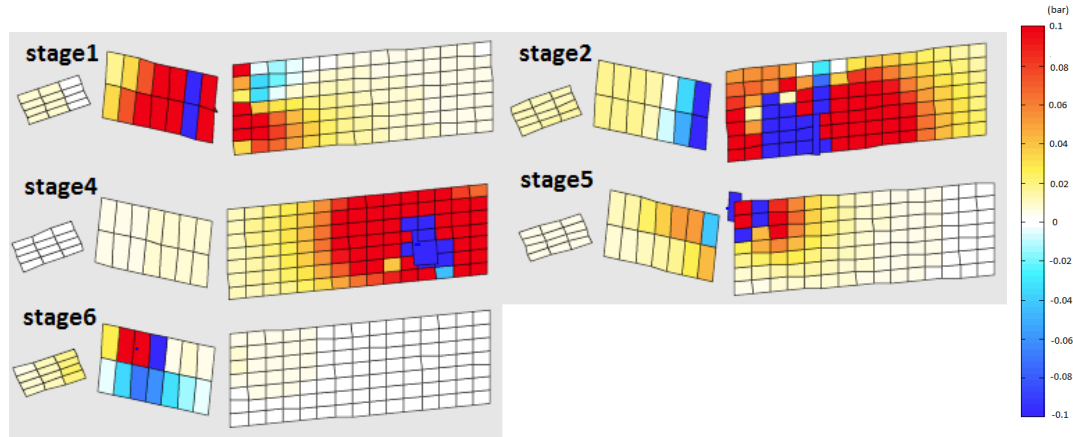


Figure 4-6. Coulomb Stress change resolved on seismogenic fault planes at each stage shown in Figure 4-5. (No focal mechanism information available in stage 3)

Table 4-1 Cumulative rupture information for each stage.

stage	# of events	center lat	center lon	center dep	cumulative mag	strike	dip	slip
1	56	36.5044	-99.0412	6.85	4.2	289.1	57.4	-61.3
2	152	36.5122	-99.007	7.65	4.3	84.4	83.2	-168.6
3	20	36.5217	-98.9826	6.89	3.5	--	--	--
4	231	36.524	-98.9709	7.12	4.1	66.2	67.9	-177.2
5	65	36.5058	-99.0305	5.79	3.7	84.4	83.2	-168.6
6	35	36.5038	-99.058	6.24	3.6	107.3	52.2	-90.5

Chapter 5 Dynamic triggering in Oklahoma

5.1 Introduction

Earthquake triggering by transient stresses from seismic waves of distant main shocks has been observed in many studies [*Hill et al.*, 1993; *Gomberg et al.*, 2001; *Prejean et al.*, 2004; *Brodsky and van der Elst*, 2014]. Areas associated with volcanic or geothermal activity and extensional tectonics are often more prone to dynamic triggering [e.g., *Brodsky and Prejean*, 2005; *Moran et al.*, 2004; *Harrington and Brodsky*, 2006]. Most cases of observed dynamic triggering are where natural earthquakes tend to occur, but recent studies show triggering in regions with low levels of historical seismicity, such as fluid-injection areas, where the triggering occurred prior to large earthquakes, revealing critically stressed faults [*van der Elst et al.*, 2013]. In this chapter, I follow a typical procedure [*Wang et al.*, 2015] to search for dynamic triggering evidence. Fluid injection can increase pore pressure and bring the faults closer to failure. The triggering susceptibility will help identify some critically loaded faults.

5.2 Catalog study

I select large earthquakes between 2010 and 2015 from International Seismological Center (ISC) catalog as potentially triggering earthquakes (refer to as ‘mainshock’ below) using the criteria that surface magnitude (M_s) is larger than 6.5, depth less than 100km and peak ground velocity (PGV) larger than 0.01cm/s. PGV is estimated using the following empirical ground motion regression [*van der Elst and Brodsky*, 2010]:

$$\log A_{20} = Ms - 1.66 \log_{10} \delta - 6 \quad (5-1)$$

$$PGV \approx \frac{2\pi A_{20}}{T} \quad (5-2)$$

where Ms is the surface wave magnitude and δ is the epicenter-station distance in degrees, and T is the period of dominant surface wave ($T = 20s$). Figure 5-1 shows the 49 mainshocks satisfying the above criteria.

I then calculate beta map for each mainshock in the United States using ANSS catalog (magnitude completeness 3.0) with 1° by 1° grid and time window 30 days before and 10 days after each main shock. Then I stack beta value larger than 2.0 for all mainshocks.

The β statistic is a widely accepted quantitative measure of the level of dynamic triggering representing the standard deviation in the background seismicity rate following a remote dynamic triggering event [Matthews and Reasenberg, 1988; Reasenberg and Simpson, 1992; Hill and Prejean, 2007; Wang et al, 2015]. The β statistic is calculated using the following equation [Aron and Hardebeck, 2009]:

$$\beta(N_1, N_2, t_1, t_2) = \frac{N_2 - (N_1 + N_2) \cdot \frac{t_2}{t_1 + t_2}}{\sqrt{(N_1 + N_2) \cdot \frac{t_2}{t_1 + t_2} \cdot (1 - \frac{t_2}{t_1 + t_2})}} \quad (5-3)$$

where t, N are time window and the number of events occurring in the window; subscript 1, 2 denote before and after the mainshock, respectively. If less than 3 earthquakes are observed during time t in a grid, the beta is set to NAN. In general, a β

statistic larger than 2.0 indicates a significant increase in seismic activity at 95% confidence level [Hill and Prejean, 2007].

Figure 5-2 shows the stacked β statistic in continental U.S.. Geothermal and volcanic areas in California show strong positive beta anomaly, which are consistent with previous dynamic triggering studies in those areas [e.g., Aiken and Peng, 2014]. In mid-continent, northern and central Oklahoma and Texas show striking beta anomaly. To further explore the dynamic triggering in Oklahoma, I calculate a finer grid (0.1° by 0.1°) beta map (Figure 5-4) using Oklahoma Geological Survey (OGS) earthquake catalog with magnitude completeness (M_c) 2.8 and same time window 30 days before and 10 days after each main shock (Figure 5-3) with PGV larger than 0.002cm/s. Table 5-1 lists 10 mainshocks showing beta anomaly in an isolated earthquake cluster in Woodward, northwest Oklahoma. Large positive beta indicates potentially significant dynamic triggering in this area. I thus focus on the dynamic triggering search in Woodward cluster in the following section.

5.3 Waveform study and analysis

The monitoring network in early 2015 in Woodward, Oklahoma only included one broadband station U32A. Earthquake waveforms recorded on U32A show that the signal to noise ratio (SNR) is high for most events; therefore, I use U32A in a matched-filter technique to detect uncataloged events based on the similarity to known events. Similar methods have been used to identify tectonic tremor in Japan and microearthquakes in the U.S. [Shelly *et al.*, 2007; van der Elst *et al.*, 2013].

For the mainshocks showing positive beta anomaly in Woodward, first I visually examine the waveform on nearby station U32A. Small events were occurring during the passage of surface wave and these events might be triggered by transient stresses generated by surface wave from remote, large earthquake. Then, I run matched-filter detection on continuous waveform on U32A in the time window 1day before and 1day after the large earthquakes using selected templates. The templates are created from waveform data of local events filtered between 4 and 15Hz in 3s time window that includes distinct P and S arrivals. The local events are selected using criteria that magnitude larger than 2.0, distinct P and S time arrival and occurring within 10 days of the mainshock; if the number of templates is smaller than 10, I extend the time window to select more events. The average number of templates is 17 for each mainshock. Then the templates are used to cross correlate with continuous waveform data and a high cross correlation coefficient larger than nine times of median absolute deviation (MAD) signifies the detection of an event. The P and S wave arrival time differences of the templates are around 2 seconds, so the detected events should be within 20km of the station U32A. The detection result for May 12th, 2015 Nepal earthquake is shown in Figure 5-5. There was a quiescence before the Nepal earthquake and significant seismicity increase after the mainshock, of which four local events were triggered during the surface wave.

After detection, I obtain a detected catalog with small events. I compute β statistic with the detected catalog using equation 5-3, where t_1 is the time window 5hours before the P wave. I define two triggering windows, instantaneous window t_2 with time between

the 5km/s and 2km/s wave arrival, when most of the surface wave energy is captured, and a delayed window t'_2 with time between 2km/s wave arrival and up to 5h after P wave arrival [e.g., *Peng et al.*, 2010]. The β statistic is listed in Table 5-1. Of ten remote mainshocks, the May 12th, 2015 M7.3 Nepal earthquake shows significant triggering phenomenon ($\beta > 2.0$) in both instantaneous and delayed time window.

5.4 Dynamic stress calculation

Triggered events tend to occur on critically loaded faults which fail under the transient stress perturbation generated by surface wave [*van der Elst*, 2014]. So, the dynamic stress threshold can help illuminate the fault stress state. To get the dynamic stress, I process the data in Seismic Analysis Code (SAC) package by removing mean value and the trend, tapering, transferring the original record to velocity domain and rotating the east/north/Z components to radial/transverse/Z components in great circle path. Then, I read the maximum value of the surface wave as peak ground velocity (PGV); using empirical equation [*van der Elst and Brodsky*, 2010], dynamic stress is converted from PGV by:

$$\sigma = PGV * \frac{\mu}{v} \quad (5-4)$$

Where μ is shear rigidity, and v is the phase velocity. Assuming μ of 35GPa and phase velocity of 3.5km/s, I have

$$\sigma(kPa) = PGV(cm/s) * 100 \quad (5-5)$$

The calculated dynamic stress is listed in Table 5-2. The maximum dynamic stress is a fraction of 1kPa, which is lower than many dynamic triggering cases, but still possible

[Aiken and Peng, 2014; Wang *et al.*, 2015] to trigger local earthquakes if the faults are critically loaded.

5.5 Magnitude calibration of detected events

Since I have only one station (U32A) to run matched-filter detection, the detected events can not be located accurately, but magnitude for newly detected events can be estimated. I use a template-matching approach [Cleveland and Ammon, 2015; Shelly *et al.*, 2016] to estimate the magnitude of the new event (M_{new}) based on the magnitude of the template event ($M_{template}$) using the following equation:

$$M_{new} = M_{template} + c \log_{10} \alpha \quad (5-6)$$

where α is the ratio of the newly detected event and the template amplitudes [e.g., Schaff and Richards, 2014] and c is a scaling constant. We estimate α using a principal component fit of data:

$$\alpha = \frac{v(2)}{v(1)} \quad (5-7)$$

where $v(1)$ and $v(2)$ are elements of the eigenvector v corresponding to the largest eigenvalue of the covariance matrix of x and y , $\text{Cov}(x,y)$, and x is the template waveform vector and y is the corresponding newly detected waveform. The cross correlation coefficient threshold of x and y is 0.65 to perform the calibration.

Since I am dealing with relatively small events with corner frequencies dominantly above our band-pass range of 4~15 Hz, the measured amplitude ratio for this band-passed data should accurately reflect the ratio of seismic moments and moment magnitude (M_w) [Shelly *et al.*, 2016], in which case $c = 2/3$ [Hanks and Kanamori,

1979]. In our study, $c=2/3$ is not just a theoretical value; it can be observed from template calibration. If we follow the similar procedure to calibration template events:

$$\log M_2 - \log M_1 = \log \alpha_{1,2} \quad (5-8)$$

where M_1, M_2 are seismic moment for template pair 1 and 2. $\alpha_{1,2}$ is the principal component slope between template waveform vector 1, 2; then I perform the same calculation for all template pairs. All the measurements are then combined to solve the linear equation below and get the seismic moment for each template.

$$\begin{bmatrix} \log \alpha_{1,2} \\ \log \alpha_{1,3} \\ \log \alpha_{1,4} \\ \vdots \\ \log \alpha_{N-1,N} \\ \sum \log M_0 \end{bmatrix} = \begin{bmatrix} -1 & 1 & 0 & 0 & 0 & 0 & \dots & 0 & 0 \\ -1 & 0 & 1 & 0 & 0 & 0 & \dots & 0 & 0 \\ -1 & 0 & 0 & 1 & 0 & 0 & \dots & 0 & 0 \\ \vdots & \vdots & \vdots & \vdots & \vdots & \vdots & \vdots & \vdots & \vdots \\ 0 & 0 & 0 & 0 & 0 & 0 & \dots & -1 & 1 \\ 1 & 1 & 1 & 1 & 1 & 1 & \dots & 1 & 1 \end{bmatrix} * \begin{bmatrix} \log M_1 \\ \log M_2 \\ \vdots \\ \log M_N \end{bmatrix} \quad (5-9)$$

where $\sum \log M_0$ denotes the summation of approximate logarithmic seismic moment of all templates, which are obtained from original catalog magnitudes. It is used to constrain the total seismic moment for all events. Then we cross plot the magnitude difference and α for all template pairs; and the slope after calibration shown in Figure 5-6 is exactly $2/3$ as suggested by *Hanks and Kanamori* [1979].

After magnitude calibration, the magnitude completeness of 181 detected events around Nepal earthquake in three days is -0.3 (Figure 5-7), greatly improved from the magnitude completeness 2.8 of the cluster. The b value for this 3-day detected catalog is low ($b=0.54$); this could be due to the artifact of insufficient station coverage, or it could be due to fault reactivation during this stage; the b value before calibration was

also relatively low ($b=0.96$). It will be ideal to calculate the average principal component slope among stations with a full azimuth coverage. Since we only have one station to the south of the cluster, the epicentral distance of events might affect the magnitude calibration. I tested this method on another cluster with 254 events and much better station coverage in Guthrie, Oklahoma; the results showed that b value only changed from 1.05 to 1.21 after calibration. The method can be used to estimate magnitude, but we should be careful with some artifacts caused by lack of station coverage.

5.6 Discussion

Our study shows that May 12th, 2015 M7.3 Nepal earthquake (refer to as ‘Nepal earthquake’ below) triggered events in Woodward area; while the March 29th, 2015 M7.5 earthquake (refer to as ‘Papua earthquake’ below) did not. Both earthquakes occurred when the seismicity rate in Woodward cluster was high (Figure 5-8, same as stage2 in Figure 4-4). I detected 217 and 120 small events within one day before and one day after Papua earthquake and Nepal earthquake, respectively, suggesting that area was very active in early 2015. Both earthquakes showed a seismicity increase using detected catalog, but the increase of Papua earthquake started before the surface wave arrival while the increase of Nepal earthquake followed the surface wave arrival (Figure 5-9); the seismicity after Papua earthquake showed a random magnitude distribution while the seismicity after Nepal earthquake showed a decrease in magnitude (Figure 5-10), which could be a triggered aftershock sequence. From those comparisons, I think it is likely that the M7.3 Nepal earthquake triggered local events in surface wave; while

the seismicity rate increase following Papua mainshock was just coincident in time with the cluster events.

5.7 Conclusion

In this study, I perform a systematic search for dynamic triggering evidence in Oklahoma. In the stacked beta map for the whole continental U.S., the triggering potential ($\beta > 2.0$) of Oklahoma is strikingly high. A detailed local catalog search shows triggering potential in central, northern and northwestern Oklahoma. I focus my search on Woodward, a transtensional area in northwest Oklahoma. By visually examining the waveform and matched-filter detection for ten large, remote earthquakes showing positive beta in Woodward, I find that May 12th, 2015 Mw7.3 Nepal earthquake showed dynamic triggering in that area. During the passage of surface wave of Nepal earthquake, four local events were triggered; the seismicity rate was significant higher after the surface wave arrival. I calculate the triggering stress from waveform as 0.76kPa; such a low triggering threshold suggests the fault was critically loaded at the time of mainshock.

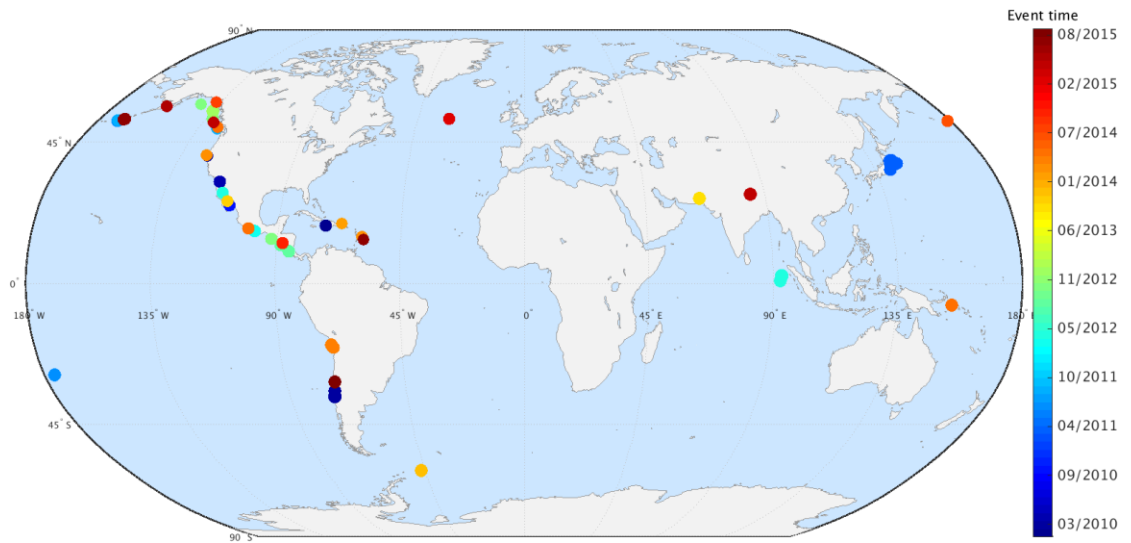


Figure 5-1. Mainshock distribution from 2010 to 2015 with $M_s > 6.5$, $depth < 100km$, and $PGV > 0.01cm/s$. There are 49 mainshocks used in continental U.S beta search.

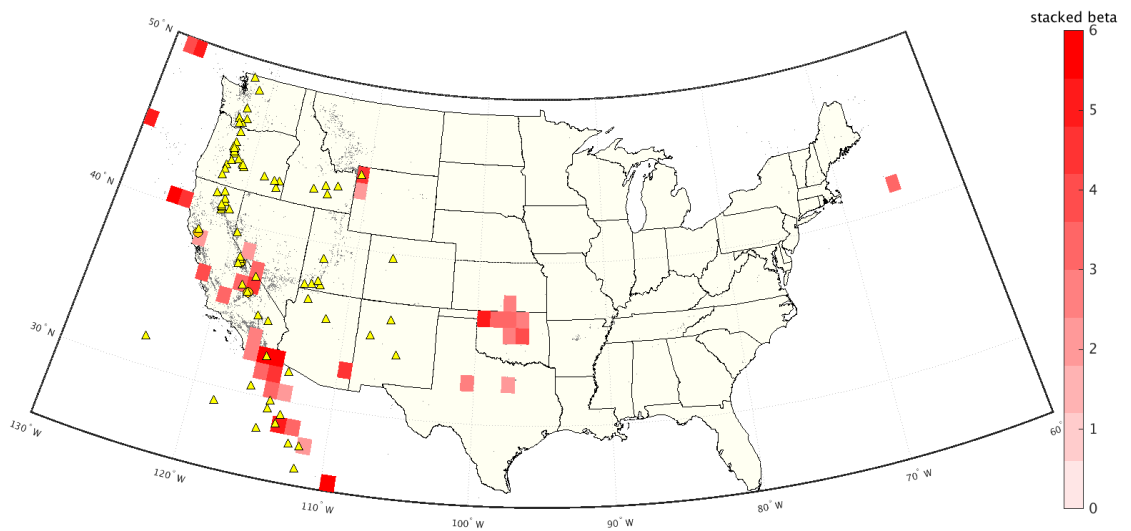


Figure 5-2. Stacked beta (>2.0) map from 49 mainshocks shown in Figure 5-1. Gray dots are seismicity from ANSS catalog with $M > 3.0$; yellow triangles are volcanoes; orange circles are geothermal fields in California.

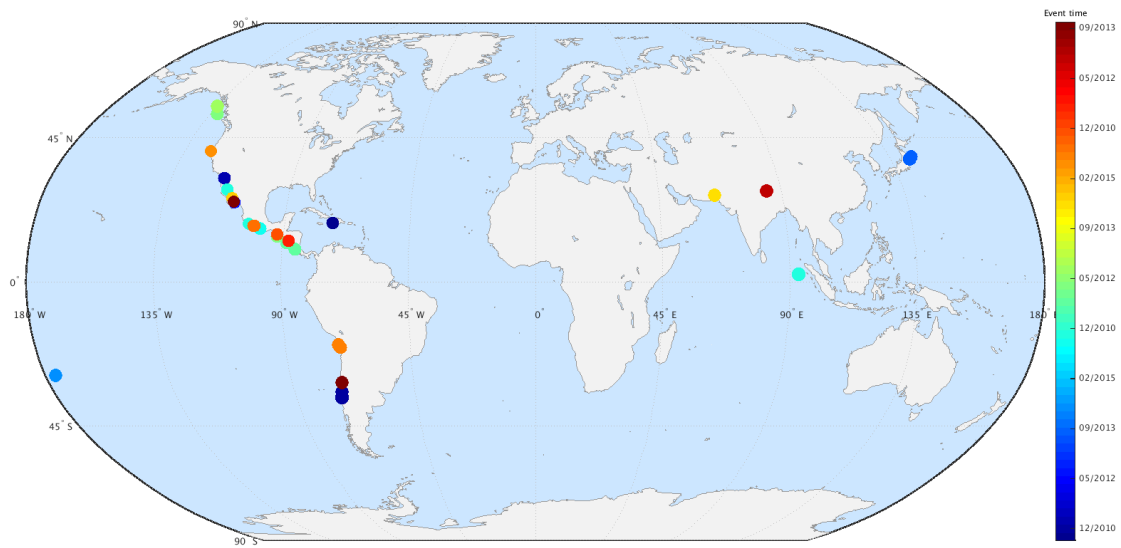


Figure 5-3. Mainshock distribution from 2010 to 2015 with $M_s > 6.5$, $depth < 100km$, and $PGV > 0.002cm/s$. There are 29 mainshocks used in Oklahoma beta search.

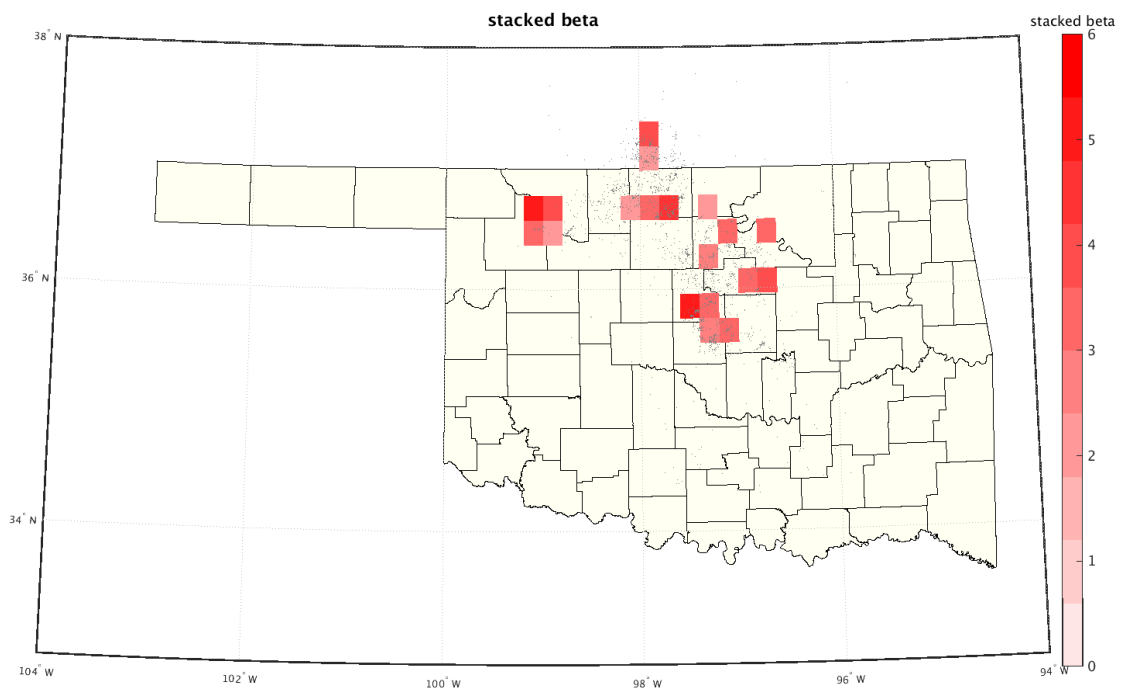


Figure 5-4. Stacked beta (>2.0) map from 29 mainshocks in Figure 5-3. Gray dots are earthquake locations from OGS catalog.

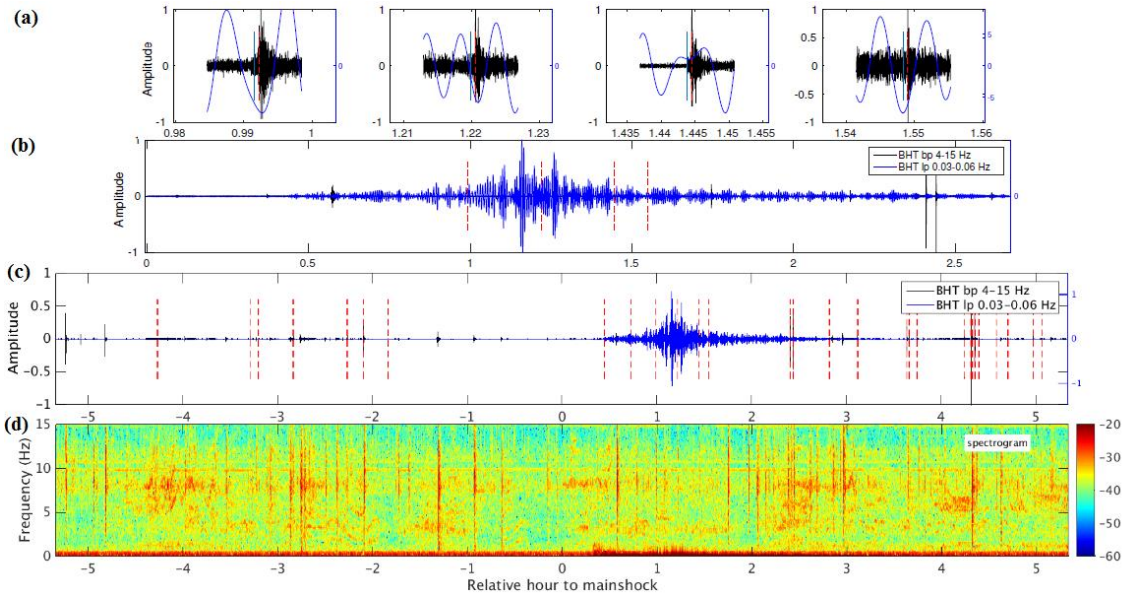
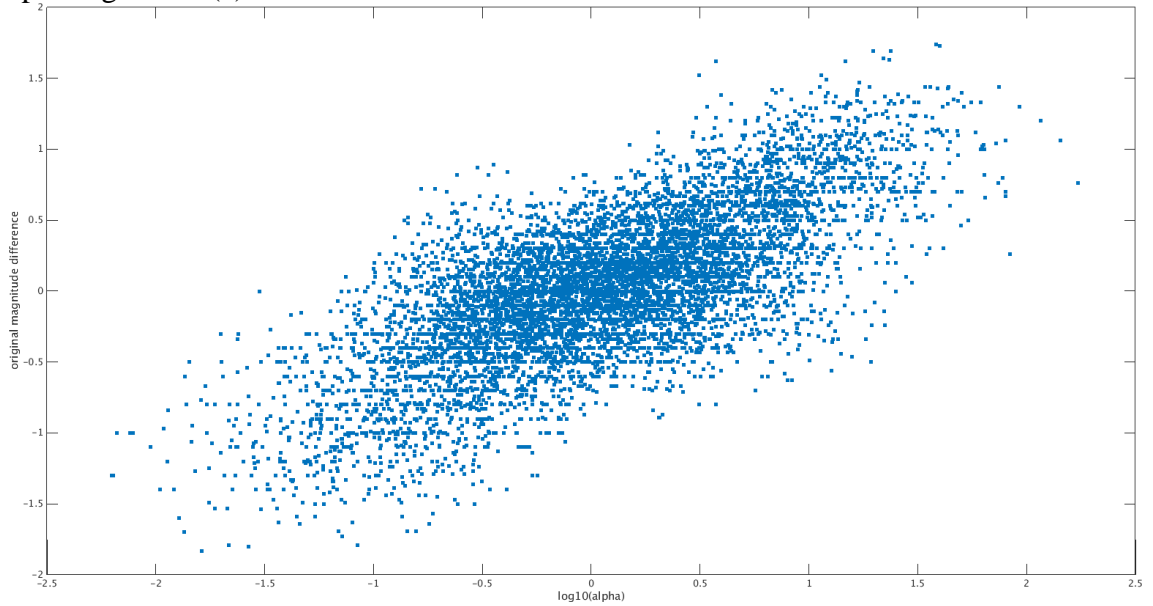


Figure 5-5. Matched filter detection results of May 12th, 2015 M7.3 earthquake shown on waveforms of station U32A, BHT component. Red dashed lines are detected events; (c) shows the waveform 5h before till 5h after the mainshock; (b) zooms into 2.5h after mainshock; (a) zooms into four detected events in surface wave in (b); (d) shows the spectrogram of (c).



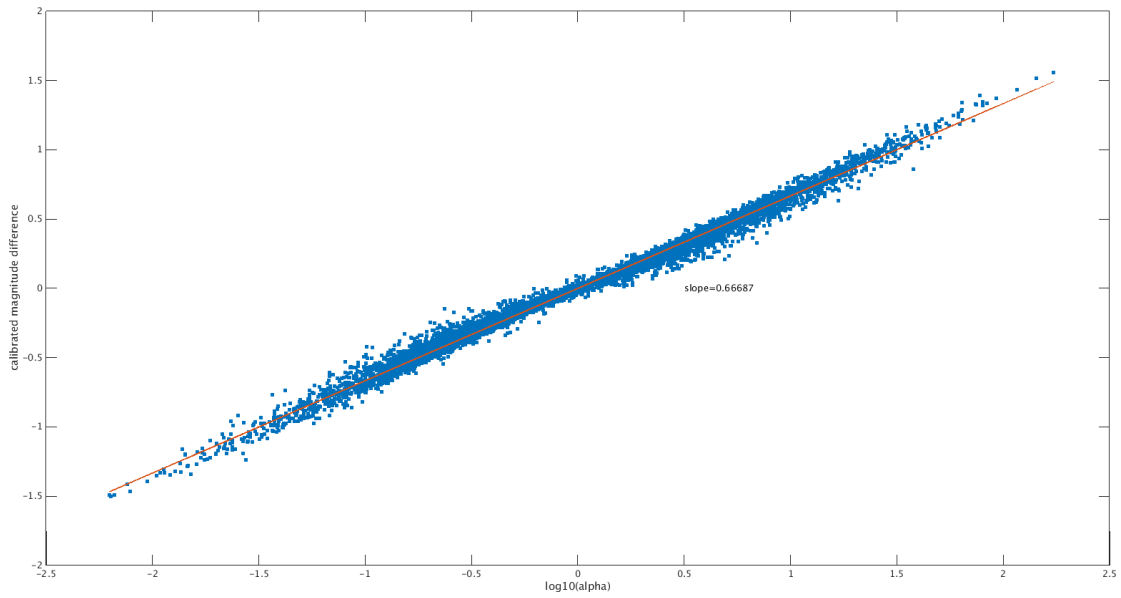
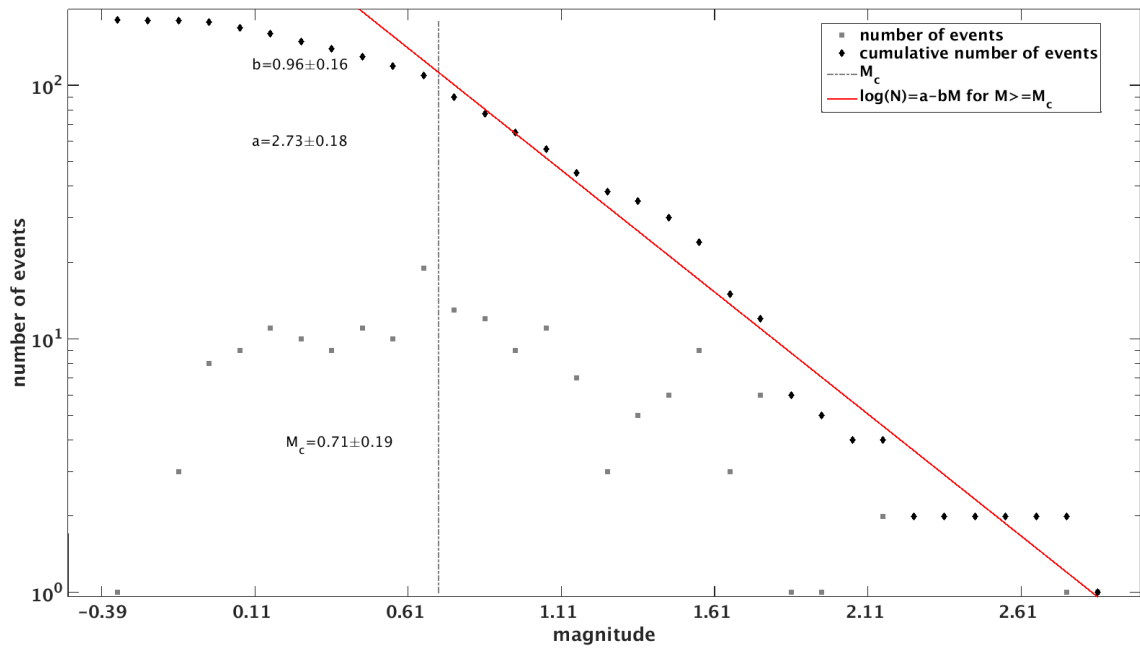


Figure 5-6. Magnitude difference versus $\log_{10}(\alpha)$ for templates used in matched-filter detection. Top: before magnitude calibration; bottom: after magnitude calibration. The slope is the constant c in equation 5-6.



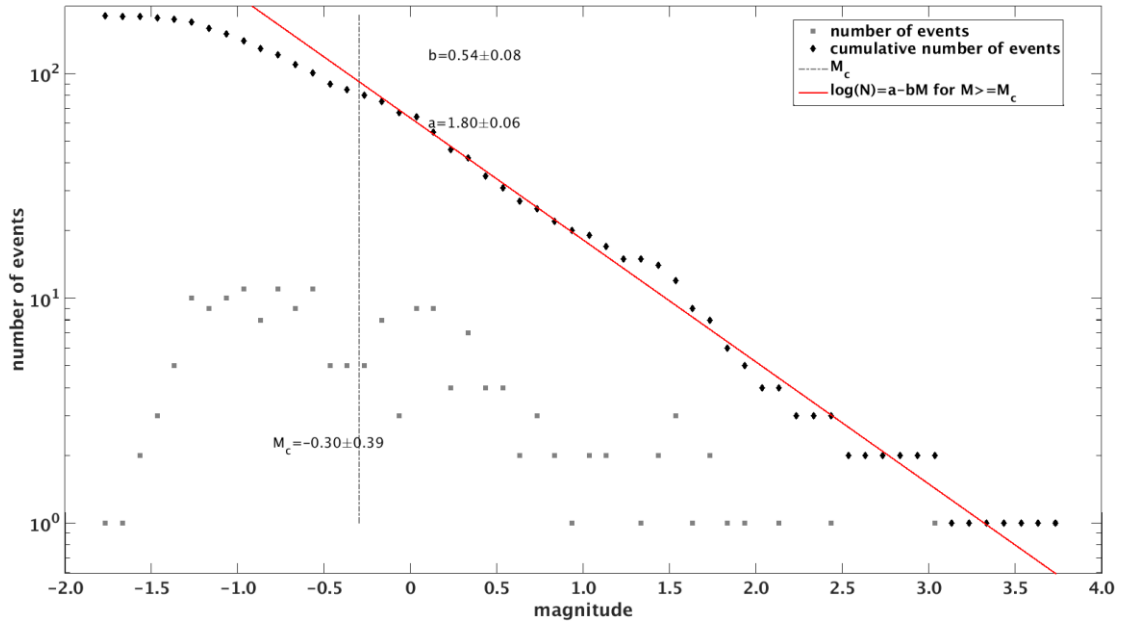


Figure 5-7. Magnitude distribution for detected events around May 12th, 2015 M7.3 mainshock. Top: before calibration; bottom: after calibration.

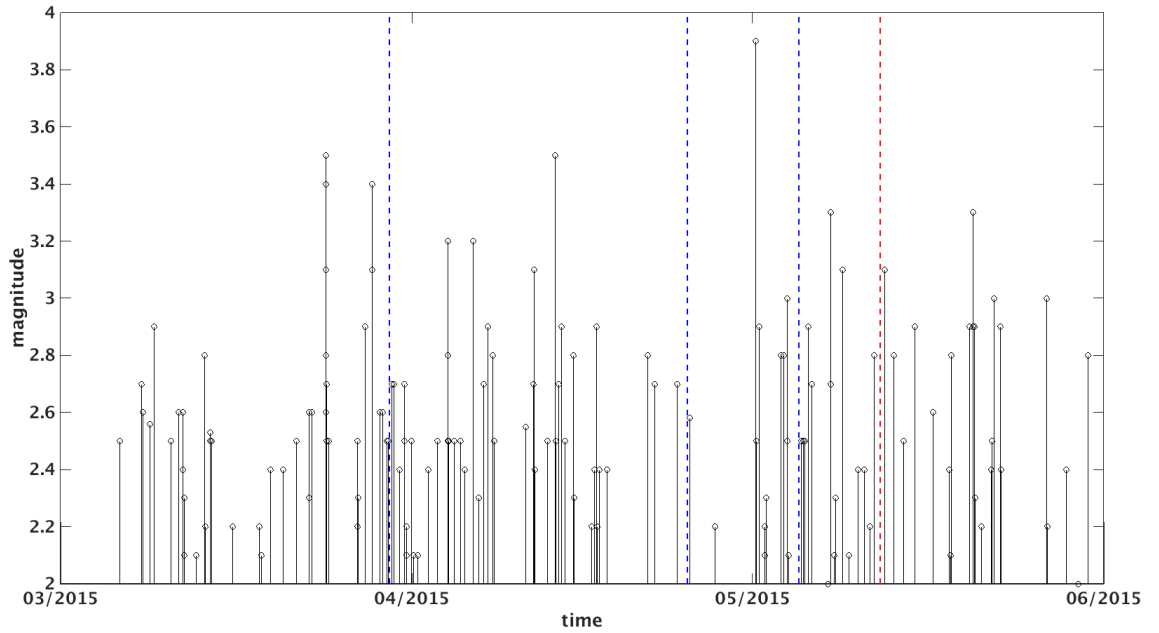


Figure 5-8. Magnitude-time distribution of cataloged events in stage2 in figure 4-4. Dashed lines are large earthquakes that shows positive beta anomaly in stage2; blue means no triggering; red denotes the triggering event of May 12th, 2015 M7.3 Nepal earthquake.

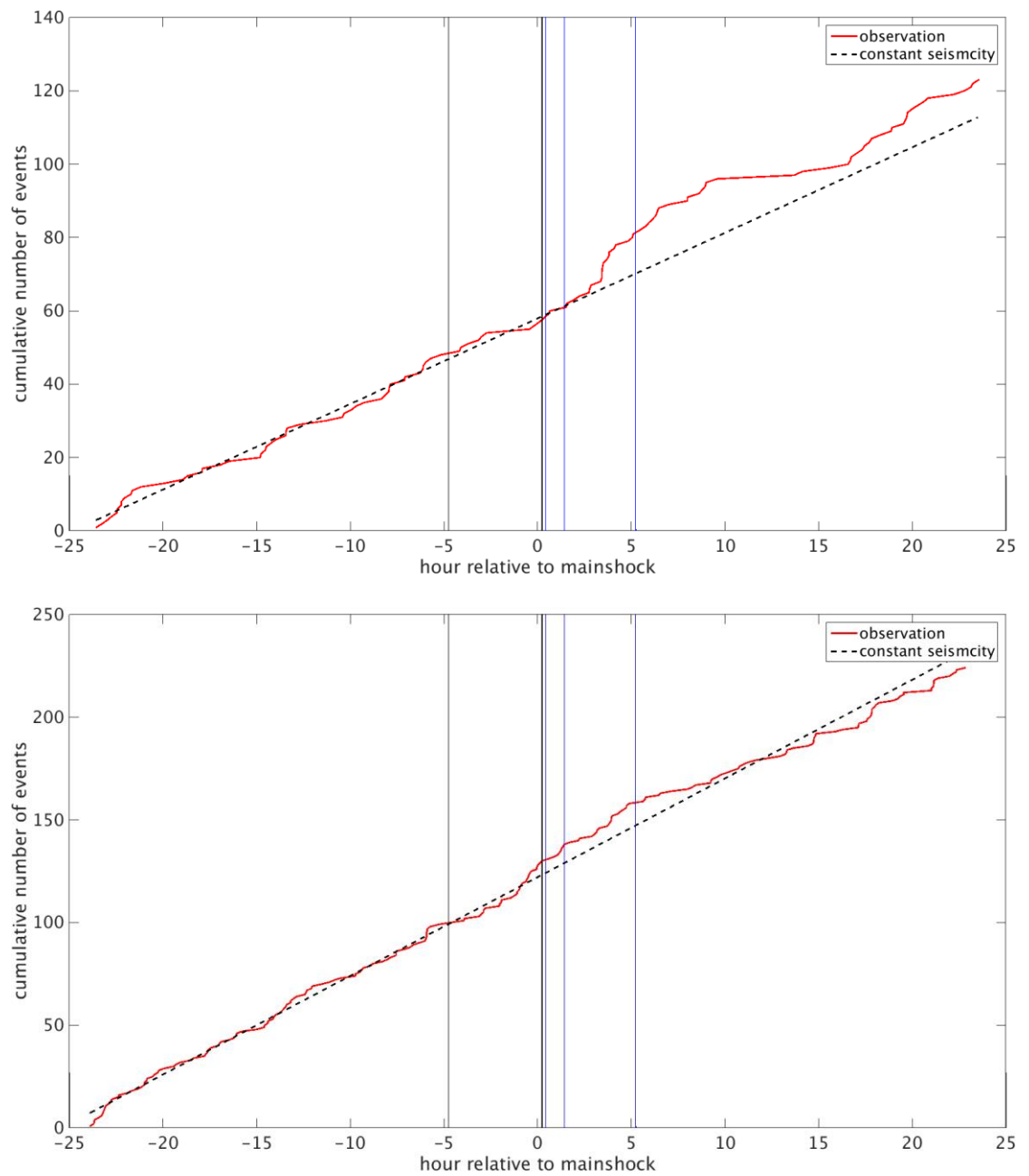


Figure 5-9. Seismicity rate within 24 hours of May 12th, 2015 M7.3 mainshock (top) and March 29th, 2015 M7.5 mainshock (bottom). Red line is the observation; black line is constant rate based on the seismicity rate before mainshock.

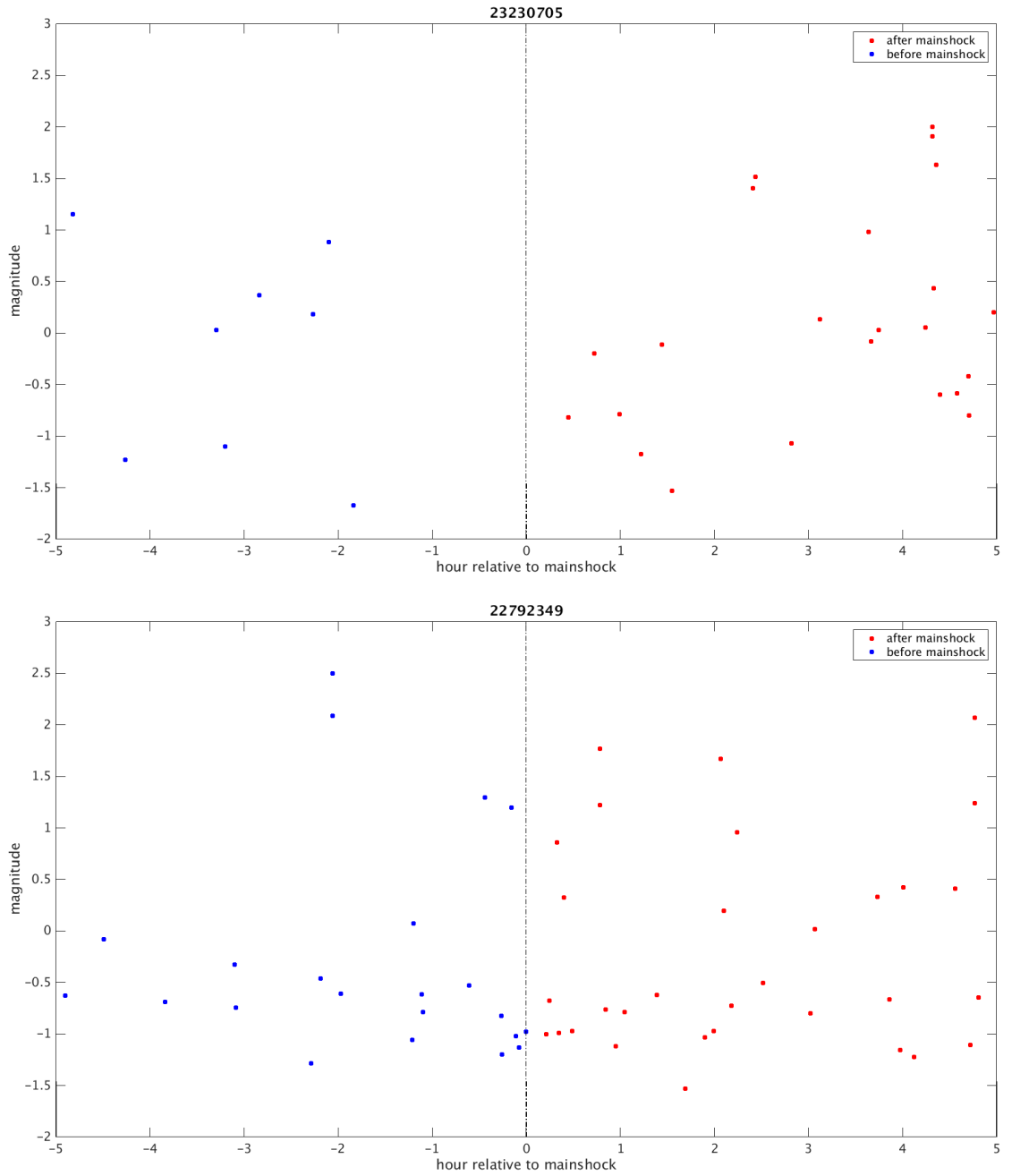


Figure 5-10. Magnitude distribution of detected catalog for May 12th, 2015 M7.3 mainshock (top) and March 29th, 2015 M7.5 mainshock (bottom).

Table 5-1 Mainshock information showing positive β statistic in Woodward area and calculated β using detected catalog.

event id	origin time		Magnitude	N1	N2	instantaneous	N1	N2	Delayed
21080215	10/9/2014	2:14:31	7	2	0	nan	2	1	nan
21130352	10/14/2014	3:51:34	7.3	9	1	0.82	9	6	-0.65
21980507	1/7/2015	5:07:08	6.5	6	0	-0.61	6	6	0.15
22792349	3/29/2015	23:48:31	7.5	22	6	0.68	22	23	1.28
23060611	4/25/2015	6:11:26	8.1	13	4	0.64	13	13	0.94
23160144	5/5/2015	1:44:06	7.5	17	0	-1.85	17	14	0.4
23230705	5/12/2015	7:05:20	7.3	7	5	2.18	7	18	3.16
23990450	7/27/2015	4:49:46	6.9	2	1	nan	2	2	0.14
24502255	9/16/2015	22:54:33	8.3	1	0	nan	1	4	1.58
24502319	9/16/2015	23:18:42	7	1	0	nan	1	4	1.58

Table 5-2 Dynamic stress of each mainshock showing positive β statistic in Woodward area.

event id	origin time		Magnitude	σ_T (kpa)	σ_R (kpa)	σ_z (kpa)
21080215	10/9/2014	2:14:31	7	0.135	0.629	0.792
21130352	10/14/2014	3:51:34	7.3	0.789	1.176	0.635
21980507	1/7/2015	5:07:08	6.5	0.033	0.036	0.038
22792349	3/29/2015	23:48:31	7.5	0.33	0.44	0.57
23060611	4/25/2015	6:11:26	8.1	0.87	0.82	0.82
23160144	5/5/2015	1:44:06	7.5	0.88	1.04	1.35
23230705	5/12/2015	7:05:20	7.3	0.367	0.606	0.763
23990450	7/27/2015	4:49:46	6.9	0.081	0.074	0.092
24502255	9/16/2015	22:54:33	8.3	0.485	1.07	1.235
24502319	9/16/2015	23:18:42	7	0.485	1.07	1.235

Conclusion

In this project, I use seismicity to map currently active faults; I generate a detailed stress field map for Oklahoma using focal mechanism solutions. By comparing the fault strike and σ_{Hmax} orientation, I find that many of the currently reactivated faults are optimally oriented to local stress field.

The detailed stress field map (0.2° by 0.2°) reveals more spatial variations compared to a uniform stress field in previous studies. The stress orientation shows a clear rotation along Nemaha fault in Central Oklahoma, in northern Oklahoma and southern Kansas and in northwestern Oklahoma. To the north and northwest, the map shows a faulting type transition from strike-slip faulting to normal faulting, suggesting the stress magnitude is less compressive in those areas.

Woodward cluster is an isolated, large cluster in one of those transition areas in northwest Oklahoma. The area is in transtensional regime which is characterized by both strike-slip and normal faulting. Two optimally oriented fault segments are reactivated in this cluster; the seismicity migration is used to depict the rupture process and the rupture pattern is explained by Coulomb Stress interaction.

In a relatively independent study, I search for dynamic triggering evidence in Oklahoma and find that May 12th, 2015 M7.3 Nepal earthquake triggered local events. The triggering stress is lower than $1kPa$, suggesting the fault was critically loaded at the mainshock time.

References

- Aiken, Chastity, and Zhigang Peng. "Dynamic triggering of microearthquakes in three geothermal/volcanic regions of California." *Journal of Geophysical Research: Solid Earth* 119, no. 9 (2014): 6992-7009.
- Alt, Richard C., and Mark D. Zoback. "A Detailed Oklahoma Stress Map for Induced Seismicity Mitigation." In *AAPG Annual Convention and Exhibition*. 2015.
- Aron, Allegra, and Jeanne L. Hardebeck. "Seismicity rate changes along the central California coast due to stress changes from the 2003 M 6.5 San Simeon and 2004 M 6.0 Parkfield earthquakes." *Bulletin of the Seismological Society of America* 99, no. 4 (2009): 2280-2292.
- Ben-Zion, Yehuda. "Collective behavior of earthquakes and faults: Continuum-discrete transitions, progressive evolutionary changes, and different dynamic regimes." *Reviews of Geophysics* 46, no. 4 (2008).
- Bott, Martin Harold Phillips. "The mechanics of oblique slip faulting." *Geological Magazine* 96, no. 02 (1959): 109-117.
- Brodsky, Emily E., and Nicholas J. van der Elst. "The uses of dynamic earthquake triggering." *Annual Review of Earth and Planetary Sciences* 42 (2014): 317-339.
- Brodsky, Emily E., and Stephanie G. Prejean. "New constraints on mechanisms of remotely triggered seismicity at Long Valley Caldera." *Journal of Geophysical Research: Solid Earth* 110, no. B4 (2005).
- Byerlee, James. "Friction of rocks." *Pure and applied geophysics* 116, no. 4 (1978): 615-626.
- Chen, Chen. "Comprehensive analysis of Oklahoma earthquakes: from earthquake monitoring to 3D tomography and relocation." PhD diss., University of Oklahoma, 2016.
- Cheng, Yifang. "Seismicity and source spectra analysis in Salton Sea Geothermal Field", MSc diss., University of Oklahoma, 2016.
- Chen, X., and P. M. Shearer. "Comprehensive analysis of earthquake source spectra and swarms in the Salton Trough, California." *Journal of Geophysical Research: Solid Earth* 116, no. B9 (2011).
- Cleveland, K. Michael, and Charles J. Ammon. "Precise relative earthquake magnitudes from cross correlation." *Bulletin of the Seismological Society of America* (2015).

Darold, A. P., and A. A. Holland. "Preliminary Oklahoma Optimal Fault Orientations Determined by Focal Mechanism Solutions." In *AGU Fall Meeting Abstracts*. 2015.

Felzer, Karen R., and Emily E. Brodsky. "Decay of aftershock density with distance indicates triggering by dynamic stress." *Nature* 441, no. 7094 (2006): 735-738.

Goertz-Allmann, Bettina P., and Stefan Wiemer. "Geomechanical modeling of induced seismicity source parameters and implications for seismic hazard assessment." *Geophysics* 78, no. 1 (2012): KS25-KS39.

Gomberg, J., P. A. Reasenberg, P. Bodin, and R. A. Harris. "Earthquake triggering by seismic waves following the Landers and Hector Mine earthquakes." *Nature* 411, no. 6836 (2001): 462-466.

Gomberg, J., P. Bodin, K. Larson, and H. Dragert. "Earthquake nucleation by transient deformations caused by the M= 7.9 Denali, Alaska, earthquake." *Nature* 427, no. 6975 (2004): 621-624.

Hanks, Thomas C., and Hiroo Kanamori. "A moment magnitude scale". *Journal of Geophysical Research*: Vol. 84, 2348-2350 (1979).

Hardebeck, Jeanne L., and Andrew J. Michael. "Damped regional - scale stress inversions: Methodology and examples for southern California and the Coalinga aftershock sequence." *Journal of Geophysical Research: Solid Earth* 111, no. B11 (2006).

Hardebeck, Jeanne L., and Egill Hauksson. "Crustal stress field in southern California and its implications for fault mechanics." *Journal of Geophysical Research B* 106, no. B10 (2001): 21859-21882.

Hardebeck, Jeanne L., Julie J. Nazareth, and Egill Hauksson. "The static stress change triggering model: Constraints from two southern California aftershock sequences." *Journal of Geophysical Research B* 103, no. B10 (1998): 24427-24437.

Harding, Thomas P. "Identification of wrench faults using subsurface structural data: criteria and pitfalls (1)." *AAPG Bulletin* 74, no. 10 (1990): 1590-1609.

Harding, Thomas P. "Seismic characteristics and identification of negative flower structures, positive flower structures, and positive structural inversion." *AAPG Bulletin* 69, no. 4 (1985): 582-600.

Häring, Markus O., Ulrich Schanz, Florentin Ladner, and Ben C. Dyer. "Characterisation of the Basel 1 enhanced geothermal system." *Geothermics* 37, no. 5 (2008): 469-495.

Harrington, Rebecca M., and Emily E. Brodsky. "The absence of remotely triggered seismicity in Japan." *Bulletin of the Seismological Society of America* 96, no. 3 (2006): 871-878.

Hill, David P., and Stephanie Prejean. "Dynamic triggering." (2015): 273-304.

Hill, David P., P. A. Reasenberg, A. Michael, W. J. Arabaz, G. Beroza, D. Brumbaugh, J. N. Brune et al. "Seismicity remotely triggered by the magnitude 7.3 Landers, California, earthquake." *Science* 260, no. 5114 (1993): 1617-1624.

Holland, Austin A. "Optimal fault orientations within Oklahoma." *Seismological Research Letters* 84, no. 5 (2013): 876-890.

Holland, Austin A. "Preliminary fault map of Oklahoma." *Oklahoma Geol. Surv. Open File Rep., OF3* (2015).

Jaeger, John C., and Neville GW Cook. "Fundamentals of rock mechanics, Methuen & Co." *Ltd., London* 513 (1969).

Jones, Lucile M., and Peter Molnar. "Some characteristics of foreshocks and their possible relationship to earthquake prediction and premonitory slip on faults." *Journal of Geophysical Research: Solid Earth* 84, no. B7 (1979): 3596-3608.

Keranen, Katie M., Heather M. Savage, Geoffrey A. Abers, and Elizabeth S. Cochran. "Potentially induced earthquakes in Oklahoma, USA: Links between wastewater injection and the 2011 Mw 5.7 earthquake sequence." *Geology* 41, no. 6 (2013): 699-702.

Keranen, Katie M., Matthew Weingarten, Geoffrey A. Abers, Barbara A. Bekins, and Shemin Ge. "Sharp increase in central Oklahoma seismicity since 2008 induced by massive wastewater injection." *Science* 345, no. 6195 (2014): 448-451.

King, Geoffrey CP, Ross S. Stein, and Jian Lin. "Static stress changes and the triggering of earthquakes." *Bulletin of the Seismological Society of America* 84, no. 3 (1994): 935-953.

Kisslinger, Carl. "Aftershocks and fault-zone properties." *Advances in geophysics* 38 (1996): 1-36.

Le Guerroué, Erwan, and Peter Robert Cobbold. "Influence of erosion and sedimentation on strike-slip fault systems: insights from analogue models." *Journal of Structural Geology* 28, no. 3 (2006): 421-430.

Lin, Jian, and Ross S. Stein. "Stress triggering in thrust and subduction earthquakes and stress interaction between the southern San Andreas and nearby thrust and strike-slip faults." *Journal of Geophysical Research: Solid Earth* 109, no. B2 (2004).

Lund, Björn, and John Townend. "Calculating horizontal stress orientations with full or partial knowledge of the tectonic stress tensor." *Geophysical Journal International* 170, no. 3 (2007): 1328-1335.

Martínez - Garzón, Patricia, Grzegorz Kwiatek, Michèle Ickrath, and Marco Bohnhoff. "MSATSI: A MATLAB package for stress inversion combining solid classic methodology, a new simplified user - handling, and a visualization tool." *Seismological Research Letters* 85, no. 4 (2014): 896-904.

Matthews, Mark V., and Paul A. Reasenberg. "Statistical methods for investigating quiescence and other temporal seismicity patterns." *Pure and Applied Geophysics* 126, no. 2 (1988): 357-372.

McNamara, Daniel E., Harley M. Benz, Robert B. Herrmann, Eric A. Bergman, Paul Earle, Austin Holland, Randy Baldwin, and A. Gassner. "Earthquake hypocenters and focal mechanisms in central Oklahoma reveal a complex system of reactivated subsurface strike - slip faulting." *Geophysical Research Letters* 42, no. 8 (2015): 2742-2749.

Menke, William. *Geophysical data analysis: Discrete inverse theory*. Vol. 45. Academic press, 2012.

Michael, Andrew J. "Determination of stress from slip data: faults and folds." *Journal of Geophysical Research: Solid Earth* 89, no. B13 (1984): 11517-11526.

Michael, Andrew Jay. "Use of focal mechanisms to determine stress: a control study." *Journal of Geophysical Research: Solid Earth* 92, no. B1 (1987): 357-368.

Moran, Seth C., John A. Power, Scott D. Stihler, John J. Sánchez, and Jacqueline Caplan-Auerbach. "Earthquake triggering at Alaskan volcanoes following the 3 November 2002 Denali fault earthquake." *Bulletin of the Seismological Society of America* 94, no. 6B (2004): S300-S309.

Naylor, M. A., G. T. Mandl, and C. H. K. Supsteijn. "Fault geometries in basement-induced wrench faulting under different initial stress states." *Journal of Structural Geology* 8, no. 7 (1986): 737-752.

Omori, Fusakichi. *On the after-shocks of earthquakes*. Vol. 7. The University, 1894.

Peng, Zhigang, David P. Hill, David R. Shelly, and Chastity Aiken. "Remotely triggered microearthquakes and tremor in central California following the 2010 Mw 8.8 Chile earthquake." *Geophysical Research Letters* 37, no. 24 (2010).

Peng, Zhigang, John E. Vidale, Aaron G. Wech, Robert M. Nadeau, and Kenneth C. Creager. "Remote triggering of tremor along the San Andreas Fault in central California." *Journal of Geophysical Research: Solid Earth* 114, no. B7 (2009).

Prejean, S. G., D. P. Hill, E. E. Brodsky, S. E. Hough, M. J. S. Johnston, S. D. Malone, D. H. Oppenheimer, A. M. Pitt, and K. B. Richards-Dinger. "Remotely triggered seismicity on the United States west coast following the Mw 7.9 Denali fault earthquake." *Bulletin of the Seismological Society of America* 94, no. 6B (2004): S348-S359.

Qi, Wen. "Stress analysis of recent earthquakes in Oklahoma." MSc diss., University of Oklahoma, 2016.

Reasenbergs, Paul A., and Robert W. Simpson. "Response of regional seismicity to the static stress change produced by the Loma Prieta earthquake." *Science* 255, no. 5052 (1992): 1687.

Reches, Ze'ev, Gidon Baer, and Yossef Hatzor. "Constraints on the strength of the upper crust from stress inversion of fault slip data." *Journal of Geophysical Research: Solid Earth* 97, no. B9 (1992): 12481-12493.

Richter, Charles Francis. "Elementary seismology." (1958).

Roland, Emily, and Jeffrey J. McGuire. "Earthquake swarms on transform faults." *Geophysical Journal International* 178, no. 3 (2009): 1677-1690.

Romanowicz, Barbara. "Spatiotemporal patterns in the energy release of great earthquakes." *Science* 260, no. 5116 (1993): 1923-1927.

Schaff, David P., and Paul G. Richards. "Improvements in magnitude precision, using the statistics of relative amplitudes measured by cross correlation." *Geophysical Journal International* 197, no. 1 (2014): 335-350.

Scholz, Christopher H. *The mechanics of earthquakes and faulting*. Cambridge university press, 2002.

Shapiro, Sergei A., Ernst Huenges, and Günter Borm. "Estimating the crust permeability from fluid-injection-induced seismic emission at the KTB site." *Geophysical Journal International* 131, no. 2 (1997): F15-F18.

Shearer, Peter M. "Self-similar earthquake triggering, Båth's law, and foreshock/aftershock magnitudes: Simulations, theory, and results for southern California." *Journal of Geophysical Research: Solid Earth* 117, no. B6 (2012).

Shelly, David R., Gregory C. Beroza, and Satoshi Ide. "Non-volcanic tremor and low-frequency earthquake swarms." *Nature* 446, no. 7133 (2007): 305-307.

Shelly, David R., William L. Ellsworth, and David P. Hill. "Fluid - faulting evolution in high definition: connecting fault structure and frequency - magnitude variations during the 2014 Long Valley Caldera, California earthquake swarm." *Journal of Geophysical Research: Solid Earth* (2016).

Sumy, Danielle F., Elizabeth S. Cochran, Katie M. Keranen, Maya Wei, and Geoffrey A. Abers. "Observations of static Coulomb stress triggering of the November 2011 M5.7 Oklahoma earthquake sequence." *Journal of Geophysical Research: Solid Earth* 119, no. 3 (2014): 1904-1923.

Sylvester, Arthur G. "Strike-slip faults." *Geological Society of America Bulletin* 100, no. 11 (1988): 1666-1703.

Tchalenko, J. S. "Similarities between shear zones of different magnitudes." *Geological Society of America Bulletin* 81, no. 6 (1970): 1625-1640.

Toda, Shinji, Ross S. Stein, Keith Richards-Dinger, and Serkan B. Bozkurt. "Forecasting the evolution of seismicity in southern California: Animations built on earthquake stress transfer." *Journal of Geophysical Research: Solid Earth* 110, no. B5 (2005).

Toda, Shingi, Ross S. Stein, Volkan Sevilgen, and Jian Lin. *Coulomb 3.3 graphic-rich deformation and stress-change software for earthquake, tectonic, and volcano research and teaching-user guide*. No. 2011-1060. US Geological Survey, 2011.

Utsu, Tokuji. "43 Statistical features of seismicity." *International Geophysics* 81 (2002): 719-732.

Utsu, Tokuji. "A statistical study on the occurrence of aftershocks." *Geophysical Magazine* 30, no. 4 (1961).

Utsu, Tokuji, Yoshihiko Ogata, and S. Ritsuko. "The centenary of the Omori formula for a decay law of aftershock activity." *Journal of Physics of the Earth* 43, no. 1 (1995): 1-33.

van der Elst, Nicholas J., and Emily E. Brodsky. "Connecting near - field and far - field earthquake triggering to dynamic strain." *Journal of Geophysical Research: Solid Earth* 115, no. B7 (2010).

van der Elst, Nicholas J., Heather M. Savage, Katie M. Keranen, and Geoffrey A. Abers. "Enhanced remote earthquake triggering at fluid-injection sites in the midwestern United States." *Science* 341, no. 6142 (2013): 164-167.

Vidale, John E., Katie L. Boyle, and Peter M. Shearer. "Crustal earthquake bursts in California and Japan: Their patterns and relation to volcanoes." *Geophysical research letters* 33, no. 20 (2006).

Vidale, John E., and Peter M. Shearer. "A survey of 71 earthquake bursts across southern California: Exploring the role of pore fluid pressure fluctuations and aseismic slip as drivers." *Journal of Geophysical Research: Solid Earth* 111, no. B5 (2006).

Wallace, Robert E. "Geometry of shearing stress and relation to faulting." *The journal of Geology* 59, no. 2 (1951): 118-130.

Walsh, F. Rall, and Mark D. Zoback. "Probabilistic assessment of potential fault slip related to injection-induced earthquakes: Application to north-central Oklahoma, USA." *Geology* 44, no. 12 (2016): 991-994.

Wang, Bei, Rebecca M. Harrington, Yajing Liu, Hongyu Yu, Alex Carey, and Nicholas J. Elst. "Isolated cases of remote dynamic triggering in Canada detected using cataloged earthquakes combined with a matched - filter approach." *Geophysical Research Letters* 42, no. 13 (2015): 5187-5196.

Yeck, W. L., G. P. Hayes, D. E. McNamara, J. L. Rubinstein, W. D. Barnhart, P. S. Earle, and H. M. Benz. "Oklahoma experiences largest earthquake during ongoing regional wastewater injection hazard mitigation efforts." *Geophysical Research Letters* (2016).

Yeck, W. L., M. Weingarten, H. M. Benz, D. E. McNamara, E. A. Bergman, R. B. Herrmann, J. L. Rubinstein, and P. S. Earle. "Far - field pressurization likely caused one of the largest injection induced earthquakes by reactivating a large preexisting basement fault structure." *Geophysical Research Letters* 43, no. 19 (2016).

Yoshida, Keisuke, Akira Hasegawa, Tomomi Okada, Takeshi Inuma, Yoshihiro Ito, and Youichi Asano. "Stress before and after the 2011 great Tohoku-Oki earthquake and induced earthquakes in inland areas of eastern Japan." *Geophysical Research Letters* 39, no. 3 (2012).

Zaliapin, Ilya, Andrei Gabrielov, Vladimir Keilis-Borok, and Henry Wong. "Clustering analysis of seismicity and aftershock identification." *Physical Review Letters* 101, no. 1 (2008): 018501.

Zaliapin, Ilya, and Yehuda Ben - Zion. "Earthquake clusters in southern California I: Identification and stability." *Journal of Geophysical Research: Solid Earth* 118, no. 6 (2013): 2847-2864.

Zhang, Qiong, and Peter M. Shearer. "A new method to identify earthquake swarms applied to seismicity near the San Jacinto Fault, California." *Geophysical Journal International* 205, no. 2 (2016): 995-1005.

Zoback, Mary Lou. "First - and second - order patterns of stress in the lithosphere: The World Stress Map Project." *Journal of Geophysical Research: Solid Earth* 97, no. B8 (1992): 11703-11728.

Appendix A: Seismogenic fault mapping results

Fault #	Strike	Dip	Planarity	Start point		End point		top depth	bottom depth
1	45.4	86	0.8	36.43725	-98.7816	36.53787	-98.679	0.278	12.918
2	281	89.6	0.8	35.8207	-97.45	35.8125	-97.4093	3.644	10.195
3	291.5	67.9	0.5	35.60033	-97.4082	35.58776	-97.3767	2.585	7.747
4	61.3	86.5	0.7	35.86121	-97.3335	35.89951	-97.2635	0.015	8.035
5	131	85.5	1	36.29496	-97.536	36.27447	-97.5121	1.309	11.958
6	105.8	88.2	0.9	36.43469	-96.9638	36.40663	-96.8648	0.132	15.881
7	63	88.7	0.9	36.4361	-96.9146	36.4578	-96.872	3.139	11.273
8	104.6	84.8	0.5	35.7809	-97.4932	35.7703	-97.4527	3.401	8.237
9	225	84.1	0.9	35.64476	-97.1346	35.68275	-97.0967	0.016	17.514
10	283.1	54	0.7	36.75658	-98.0788	36.74174	-98.0159	2.449	8.366
11	78.5	79.1	0.9	36.50334	-99.0612	36.52524	-98.9555	0.001	12.415
12	117.5	87.7	0.9	35.67807	-97.422	35.66132	-97.3894	5.042	8.226
13	284.5	87.5	0.9	35.61614	-97.2617	35.60809	-97.2304	0.221	7.652
14	256.4	86.7	1	36.60985	-97.7127	36.62653	-97.6443	2.747	13.524
15	251.9	13.2	0.6	36.82945	-98.2819	36.85052	-98.2179	1.204	11.438
16	248.3	89.1	0.9	36.93297	-97.6393	36.9426	-97.6152	0.504	8.6
17	112.1	72.8	0.9	35.75005	-97.403	35.74152	-97.3821	4.63	7.284
18	54.1	83	1	35.74457	-97.3795	35.75737	-97.3617	3.939	7.694
19	273.9	53.3	1	36.94284	-97.8519	36.93973	-97.8062	1.019	7.526
20	102.3	86.9	1	36.7513	-97.5907	36.7414	-97.5455	2.267	11.587
21	105.5	88.6	1	36.271	-97.3136	36.25574	-97.2587	2.259	7.924
22	242.4	76.6	0.9	35.98163	-96.8242	36.00451	-96.7809	2.616	4.805
23	263.4	87	0.9	36.84918	-97.8743	36.85099	-97.8555	1.754	10.72
24	86.4	88.4	0.8	36.83762	-97.8872	36.8387	-97.8709	2.724	9.661
25	71	86.1	0.9	36.82695	-97.8866	36.83364	-97.8671	3.915	6.182
26	246	77.5	0.4	35.48963	-97.2707	35.50555	-97.2345	3.088	8.434
27	249.4	89.4	1	36.31875	-97.5448	36.32882	-97.5181	8.22	13.081
28	241.3	21.7	0.7	35.52734	-97.3093	35.53961	-97.2869	1.386	6.571
29	45	89.4	1	36.11653	-97.6447	36.14884	-97.6123	2.472	6.189
30	116.5	82.1	0.9	36.83515	-97.825	36.81846	-97.7912	0.61	8.358
31	120.4	85.3	1	36.22309	-97.5639	36.20743	-97.5366	1.875	7.65
32	107.6	85.9	0.8	35.92634	-97.3512	35.91499	-97.3145	0	6.071
33	257.3	85.3	0.9	36.81167	-97.7249	36.816	-97.7048	3.491	11.095
34	78.8	87.4	0.9	36.5904	-97.6401	36.5954	-97.6139	9.019	13.47
35	122.3	87.1	0.3	36.13715	-97.2989	36.12051	-97.272	0.811	7.116
36	73.3	89.3	0.9	36.65311	-98.471	36.65923	-98.4514	0.835	10.269
37	90.6	88.1	0.8	36.70831	-97.9212	36.70775	-97.8775	3.064	7.665
38	52.6	63	0.7	35.70745	-97.4434	35.72846	-97.416	0.761	6.912
39	112.3	67	0.8	35.57568	-97.3118	35.56875	-97.295	3.5	7.283
40	52.6	86.2	0.7	36.31354	-96.7736	36.32901	-96.7531	0.686	5.534
41	288.8	77.2	0.6	35.95273	-96.7943	35.94242	-96.7644	2.519	7.111
42	67.6	67.9	0.8	35.54771	-97.2579	35.55622	-97.2373	4.591	6.88
43	105.1	80.1	0.8	36.86979	-98.14	36.86385	-98.1183	4.002	6.432
44	53	85.1	0.9	35.7216	-97.1787	35.72879	-97.1695	4.616	5.564

(Continued)

Fault #	Strike	Dip	Planarity	Start point		End point		top depth	bottom depth
45	107	85.5	1	35.99109	-97.5802	35.98357	-97.5558	4.276	8.016
46	344.3	78.5	0.7	36.9332	-97.6813	36.91985	-97.6775	4.134	6.772
47	68.7	62.3	0.4	35.66286	-97.1906	35.67103	-97.169	4.037	5.141
48	251.4	85	1	36.29794	-96.694	36.30685	-96.6669	0.223	7.166
49	240.1	40.7	0.4	36.55649	-97.8456	36.57097	-97.8205	1.642	9.27
50	47.4	45.2	0.4	35.55475	-97.3093	35.56438	-97.299	2.086	6.824
51	68	82.9	0.9	36.59151	-97.8391	36.60283	-97.8111	3.217	10.126
52	122.1	87.8	1	36.18396	-97.2739	36.17214	-97.2549	1.157	8.214
53	213	51.8	0.2	36.26179	-97.3897	36.27136	-97.3838	2.843	7.869
54	54.4	81.5	0.9	35.84992	-97.2472	35.86172	-97.2308	5.015	6.179
55	34.1	58.2	0.3	35.58083	-97.2479	35.58705	-97.2438	4.836	6.18
56	240.1	87.5	0.7	36.83859	-97.7028	36.84409	-97.6933	4.579	8.062
57	161.5	80.1	0.8	36.66739	-97.7392	36.65943	-97.7372	4.569	9.421
58	51	24.1	0.7	35.71321	-97.1746	35.72441	-97.1607	4.408	5.437
59	287.9	89.7	0.7	35.79473	-97.006	35.79084	-96.9942	0.96	5.803
60	90.3	82.1	0.9	35.58478	-97.2924	35.58478	-97.2821	4.354	12.908
61	280.5	83.2	0.6	35.75028	-97.1387	35.74759	-97.1241	3.206	4.315
62	100	88.1	0.9	37.05636	-97.9237	37.05432	-97.9116	3.353	6.543
63	146.4	85.8	0.9	36.16905	-96.9984	36.15888	-96.9915	1.435	10.653
64	212.8	86	0.5	36.43651	-97.0786	36.44815	-97.0712	0.199	7.418
65	75.1	87.3	0.9	36.07258	-97.5692	36.07903	-97.5451	0.937	7.787
66	212.5	86.5	0.9	36.3868	-97.1606	36.3971	-97.1542	0.97	8.793
67	196.3	88.6	0.6	36.1055	-97.4462	36.11298	-97.4441	0.597	7.125
68	276	84.7	0.8	36.02743	-97.1116	36.02478	-97.0851	1.754	5.065
69	290	88.5	1	36.3579	-97.1174	36.3474	-97.0889	2.529	10.333
70	235.2	89.7	0.8	36.04336	-97.267	36.05752	-97.2466	1.56	5.066
71	96.1	86.1	0.9	36.70186	-98.0426	36.69979	-98.0226	4.654	6.749
72	115.7	86.5	1	36.7346	-98.3436	36.71625	-98.3054	3.67	8.123
73	330.3	88.1	0.6	36.47261	-97.3295	36.46335	-97.3243	4.631	8.727
74	108.9	89.2	0.8	36.61559	-98.4217	36.60728	-98.3975	2.815	9.314
75	273.3	88.5	0.4	35.81473	-97.2478	35.81433	-97.2377	0.459	6.246
76	258.9	70.7	0.6	36.11752	-97.5848	36.12368	-97.5541	3.729	6.355
77	207.9	87.5	1	36.56076	-97.3986	36.57367	-97.3914	4.185	10.086
78	134.8	89.4	0.8	36.07548	-97.2172	36.06598	-97.2076	3.2	12.815
79	125.4	88.8	0.8	36.69116	-98.2651	36.68277	-98.2539	4.929	7.441
80	106.5	88.9	1	36.3722	-97.7266	36.37053	-97.7197	6.795	8.313
81	101.9	45.6	0.2	35.98053	-97.2091	35.97739	-97.1933	4.798	6.02
82	55.3	86.9	1	36.26549	-97.5784	36.27179	-97.5698	6.268	8.473
83	267.8	56.8	1	36.93431	-97.9049	36.93498	-97.8841	4.047	5.982
84	235.5	74.1	0.4	36.76527	-98.0341	36.77862	-98.0149	5.086	7.324
85	93.7	84.5	1	36.21355	-97.5792	36.2125	-97.5601	4.3	7.755
86	128.1	89.8	0.9	36.28111	-97.2733	36.26443	-97.2521	0.775	10.098
87	231.9	89.6	0.9	36.11466	-97.3272	36.12392	-97.3157	1.182	8.745
88	55	89.2	0.9	35.4593	-96.8896	35.5421	-96.7445	3.038	5.6181

Appendix B: Regional stress inversion results

Grid #	Longitude	Latitude	Hmax azimuth	Standard deviation of Hmax azimuth	R	Number of focal mechanisms
1	-99.15	36.45	99	10	0.68	58
2	-99.15	36.55	100	11	0.6	46
3	-99.05	36.45	97	4	0.2	98
4	-99.05	36.55	101	5	0.22	92
5	-98.95	36.45	99	4	0.26	55
6	-98.95	36.55	98	4	0.31	49
7	-98.85	36.35	89	2	0.28	288
8	-98.85	36.45	89	2	0.29	309
9	-98.85	36.55	76	4	0.05	31
10	-98.85	36.65	91	5	0.13	26
11	-98.75	36.35	89	2	0.29	286
12	-98.75	36.45	89	2	0.29	324
13	-98.75	36.55	81	4	0.14	49
14	-98.75	36.65	88	4	0.41	33
15	-98.75	36.75	92	6	0.46	26
16	-98.65	36.45	92	4	0.15	31
17	-98.65	36.55	90	4	0.22	26
18	-98.55	36.15	65	4	0.42	22
19	-98.55	36.25	70	5	0.41	23
20	-98.55	36.45	83	8	0.35	20
21	-98.55	36.55	83	5	0.32	38
22	-98.55	36.65	82	5	0.17	33
23	-98.45	36.25	75	5	0.44	21
24	-98.45	36.45	84	7	0.31	22
25	-98.45	36.55	81	4	0.3	46
26	-98.45	36.65	76	5	0.3	50
27	-98.45	36.75	80	4	0.15	36
28	-98.35	36.55	85	4	0.28	37
29	-98.35	36.65	77	4	0.36	47
30	-98.35	36.75	79	2	0.18	94
31	-98.35	36.85	81	3	0.18	75
32	-98.25	36.35	86	3	0.23	20
33	-98.25	36.45	83	6	0.21	23
34	-98.25	36.55	83	4	0.23	36
35	-98.25	36.65	82	4	0.21	41

(Continued)

Grid #	Longitude	Latitude	Hmax azimuth	Standard deviation of Hmax azimuth	R	Number of focal mechanisms
36	-98.25	36.75	83	2	0.23	105
37	-98.25	36.85	83	2	0.23	92
38	-98.15	36.55	76	3	0.22	20
39	-98.15	36.65	84	2	0.1	83
40	-98.15	36.75	87	2	0.06	108
41	-98.15	36.85	88	4	0.08	44
42	-98.15	36.95	90	3	0.35	50
43	-98.15	37.05	93	3	0.14	89
44	-98.15	37.15	86	4	0.31	107
45	-98.15	37.25	87	5	0.38	62
46	-98.05	36.65	85	2	0.1	88
47	-98.05	36.75	85	2	0.05	92
48	-98.05	36.85	84	2	0.04	60
49	-98.05	36.95	83	2	0.12	216
50	-98.05	37.05	85	2	0.07	229
51	-98.05	37.15	74	3	0.35	227
52	-98.05	37.25	70	2	0.36	174
53	-97.95	36.55	89	4	0.37	41
54	-97.95	36.65	84	3	0.28	52
55	-97.95	36.75	82	2	0.14	75
56	-97.95	36.85	81	2	0.09	142
57	-97.95	36.95	78	2	0.12	318
58	-97.95	37.05	76	2	0.16	317
59	-97.95	37.15	69	2	0.11	268
60	-97.95	37.25	63	2	0.22	175
61	-97.85	36.25	73	4	0.23	30
62	-97.85	36.35	86	3	0.36	37
63	-97.85	36.45	95	3	0.63	33
64	-97.85	36.55	92	2	0.3	69
65	-97.85	36.65	86	2	0.26	73
66	-97.85	36.75	85	2	0.09	90
67	-97.85	36.85	83	2	0.09	140
68	-97.85	36.95	69	2	0.1	215
69	-97.85	37.05	67	1	0.21	252
70	-97.85	37.15	69	2	0.28	177

(Continued)

Grid #	Longitude	Latitude	Hmax azimuth	Standard deviation of Hmax azimuth	R	Number of focal mechanisms
71	-97.85	37.25	64	3	0.11	68
72	-97.75	36.05	88	4	0.26	22
73	-97.75	36.15	85	3	0.18	33
74	-97.75	36.25	80	3	0.04	45
75	-97.75	36.35	87	3	0.2	42
76	-97.75	36.45	112	4	0.41	45
77	-97.75	36.55	104	2	0.24	125
78	-97.75	36.65	100	2	0.24	113
79	-97.75	36.75	89	2	0.11	91
80	-97.75	36.85	89	2	0.09	135
81	-97.75	36.95	76	2	0.06	125
82	-97.75	37.05	51	2	0.09	118
83	-97.75	37.15	65	5	0.2	82
84	-97.75	37.25	99	7	0.22	26
85	-97.65	35.95	87	3	0.15	34
86	-97.65	36.05	90	3	0.06	52
87	-97.65	36.15	89	2	0.26	152
88	-97.65	36.25	92	2	0.27	155
89	-97.65	36.35	104	3	0.23	35
90	-97.65	36.45	113	4	0.32	33
91	-97.65	36.55	110	2	0.25	90
92	-97.65	36.65	104	2	0.25	93
93	-97.65	36.75	90	3	0.25	84
94	-97.65	36.85	90	2	0.27	105
95	-97.65	36.95	94	3	0.55	115
96	-97.65	37.05	74	3	0.67	94
97	-97.65	37.15	68	7	0.23	56
98	-97.65	37.25	103	8	0.18	23
99	-97.55	35.55	75	3	0.37	57
100	-97.55	35.65	81	2	0.37	115
101	-97.55	35.75	83	2	0.29	108
102	-97.55	35.85	81	2	0.21	58
103	-97.55	35.95	86	2	0.22	46
104	-97.55	36.05	91	3	0.18	53
105	-97.55	36.15	91	2	0.28	143

(Continued)

Grid #	Longitude	Latitude	Hmax azimuth	Standard deviation of Hmax azimuth	R	Number of focal mechanisms
106	-97.55	36.25	93	4	0.34	151
107	-97.55	36.35	104	4	0.23	31
108	-97.55	36.65	88	8	0.23	20
109	-97.55	36.75	94	6	0.23	31
110	-97.55	36.85	94	7	0.36	22
111	-97.55	36.95	92	5	0.74	67
112	-97.55	37.05	92	4	0.91	57
113	-97.45	35.45	80	3	0.36	53
114	-97.45	35.55	80	2	0.43	135
115	-97.45	35.65	79	2	0.4	174
116	-97.45	35.75	81	1	0.28	158
117	-97.45	35.85	80	2	0.25	111
118	-97.45	35.95	84	2	0.24	59
119	-97.45	36.05	91	5	0.14	41
120	-97.45	36.15	88	4	0.21	49
121	-97.45	36.25	91	4	0.27	42
122	-97.45	36.35	80	7	0.36	27
123	-97.45	36.45	83	8	0.07	24
124	-97.45	36.85	83	6	0.32	24
125	-97.35	35.35	96	7	0.59	22
126	-97.35	35.45	83	2	0.34	102
127	-97.35	35.55	80	2	0.38	151
128	-97.35	35.65	75	2	0.43	99
129	-97.35	35.75	83	2	0.28	132
130	-97.35	35.85	81	2	0.34	158
131	-97.35	35.95	86	3	0.37	79
132	-97.35	36.05	93	3	0.1	67
133	-97.35	36.15	83	2	0.09	100
134	-97.35	36.25	83	3	0.18	72
135	-97.35	36.35	77	5	0.29	39
136	-97.35	36.45	77	4	0.2	36
137	-97.25	35.45	84	3	0.4	66
138	-97.25	35.55	84	3	0.43	119
139	-97.25	35.65	87	3	0.36	120
140	-97.25	35.75	91	2	0.31	123

(Continued)

Grid #	Longitude	Latitude	Hmax azimuth	Standard deviation of Hmax azimuth	R	Number of focal mechanisms
141	-97.25	35.85	76	2	0.27	129
142	-97.25	35.95	74	3	0.21	73
143	-97.25	36.05	92	3	0.1	51
144	-97.25	36.15	83	2	0.09	78
145	-97.25	36.25	82	3	0.19	66
146	-97.25	36.35	84	3	0.18	40
147	-97.25	36.45	68	3	0.28	28
148	-97.15	35.45	77	5	0.54	22
149	-97.15	35.55	91	4	0.45	68
150	-97.15	35.65	97	2	0.34	103
151	-97.15	35.75	103	2	0.31	52
152	-97.15	35.85	71	3	0.2	44
153	-97.15	35.95	73	3	0.15	53
154	-97.15	36.05	84	4	0.45	34
155	-97.15	36.15	79	4	0.34	31
156	-97.15	36.25	88	4	0.25	39
157	-97.15	36.35	88	3	0.26	46
158	-97.15	36.45	79	4	0.1	28
159	-97.05	35.55	86	5	0.42	25
160	-97.05	35.65	88	5	0.42	25
161	-97.05	35.95	92	7	0.34	21
162	-97.05	36.05	86	4	0.33	46
163	-97.05	36.15	81	2	0.21	49
164	-97.05	36.25	91	3	0.16	56
165	-97.05	36.35	79	2	0.33	156
166	-97.05	36.45	74	2	0.4	120
167	-96.95	35.45	83	7	0.55	21
168	-96.95	35.85	94	4	0.25	29
169	-96.95	35.95	103	6	0.15	25
170	-96.95	36.05	97	4	0.15	33
171	-96.95	36.15	86	3	0.18	46
172	-96.95	36.25	91	4	0.17	67
173	-96.95	36.35	80	1	0.22	288
174	-96.95	36.45	77	1	0.22	240
175	-96.85	35.45	79	5	0.52	62

(Continued)

Grid #	Longitude	Latitude	Hmax azimuth	Standard deviation of Hmax azimuth	R	Number of focal mechanisms
176	-96.85	35.55	76	5	0.48	46
177	-96.85	35.85	92	4	0.31	52
178	-96.85	35.95	98	4	0.26	70
179	-96.85	36.05	104	4	0.41	46
180	-96.85	36.15	91	6	0.32	32
181	-96.85	36.25	88	4	0.19	43
182	-96.85	36.35	81	2	0.12	165
183	-96.85	36.45	79	2	0.12	135
184	-96.75	35.45	77	6	0.53	44
185	-96.75	35.55	76	4	0.51	43
186	-96.75	35.85	91	3	0.34	45
187	-96.75	35.95	96	3	0.3	54
188	-96.75	36.05	104	3	0.39	29
189	-96.75	36.15	104	4	0.11	24
190	-96.75	36.25	94	4	0.19	41
191	-96.75	36.35	80	5	0.27	26
192	-96.65	36.25	105	7	0.13	27